Doklady Physics, Vol. 48, No. 11, 2003, pp. 599–601. Translated from Doklady Akademii Nauk, Vol. 393, No. 1, 2003, pp. 33–35.

PHYSICS

Barrier Capacitance in the Case of the Polyacenequinone Contact with Aluminum

R. V. Afanas'eva, T. G. Ermakova, A. A. Maksimov, and Academician M. G. Voronkov

Received April 16, 2003

Nowadays, the basic direction in the development of semiconductor materials science is the study of electron processes at interfaces. For the vast class of low-resistivity amorphous polymeric materials with a system of conjugate bonds of the net structure, the contact phenomena are weakly investigated. For certain polycrystalline inorganic semiconductors, surface layers of crystallites form natural double heterostructures in their contact zones [1, 2]. A possibility of similar behavior of a system of intergranular barriers in pressed samples of polymeric semiconductors is indicated by an unusual capacity–voltage characteristic of polyacenequinone (PAQ) [3]. Methods of synthesis and properties of PAQ obtained on the basis of pyrene and pyromellitic dianhydride are described in [4].

Based on analysis of current–voltage characteristics and capacity–voltage characteristics, in the present paper we consider features of screening weak external electric fields at the point of metal–PAQ contact.

A typical capacity–voltage characteristic of the Al–PAQ–Ag structure at different frequencies is shown in Fig. 1 in C–V coordinates. Key to this characteristic is the symmetry of C–V curves with respect to the direction of a constant external electric field. This fact determines the principal difference of this characteristic from the capacity–voltage characteristics intrinsic to rectifying metal–semiconductor contacts with the Schottky barrier. This is explained by the fact that for these contacts, the barrier capacitance corresponds only to reverse-biased diodes [5]. Silver is used as a rear contact because the current–voltage characteristics of PAQ with silver and platinum electrodes obey the Ohm law up to the region *1* of the prebreakdown nonlinearity (Fig. 2, curve *1*). This allows us to associate the symmetry of the capacity–voltage characteristic (Fig. 1) with only the Al–PAQ contact. The comparison of curves *2* and *3* in Fig. 3 testifies to the fact that the current–voltage characteristics of the Sn–PAQ–Ag- and Al–PAQ–Ag-structures differ in only the magnitude of the contact resistance at low-voltage ohmic segments II. In contrast to the Al–PAQ contact [3], the capacity–voltage characteristic of the Sn–PAQ contact has no clearly pronounced linear segment in C^{-2}–V coordinates and therefore is not discussed in this paper. All current–voltage characteristics demonstrated in Fig. 3 are symmetric as capacity–voltage characteristics. In the case of changing the polarity, only slight differences in the slope of power segments of the current–voltage characteristics are observed. The general view of the current–voltage characteristics (Fig. 2, curve *2*) corresponds to the injection-contact phenomena concept [6]. This is implied by the existence of the initial resistivity segment II at low voltages and quadratic dependence in the segment III, which is characteristic of regimes of currents limited by the space charge (SC) [6, 7]. However, for $V \geq 2$ V, the current–voltage characteristic is independent of the electrode material (including Ag forming the electric contact with PAQ (Fig. 3, curves *1–3*)).

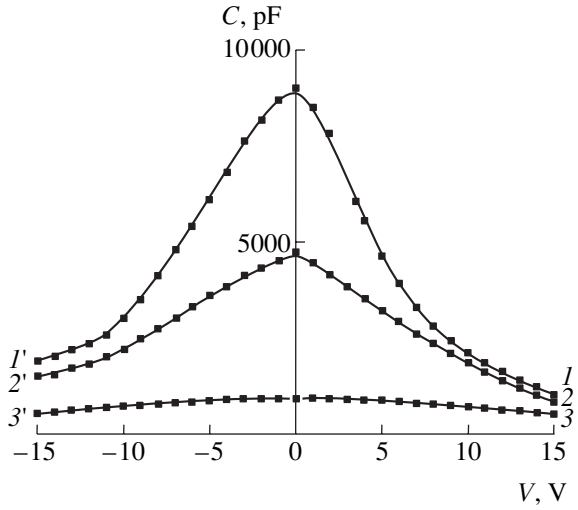

Fig. 1. Capacity–voltage characteristics of the Al–PAQ–Ag system at 20°C for the frequencies: (*1* and *1'*) 0.4, (*2* and *2'*) 1, and (*3* and *3'*) 4 kHz. The PAQ synthesis duration is 24 h; the sample thickness is 540 μm; and the diameter of electrodes is 1 cm.

Favorsky Institute of Chemistry,
Siberian Division, Russian Academy of Sciences,
Irkutsk, 664000 Russia
e-mail: samty@irioch.irk.ru

1028-3358/03/4811-0599$24.00

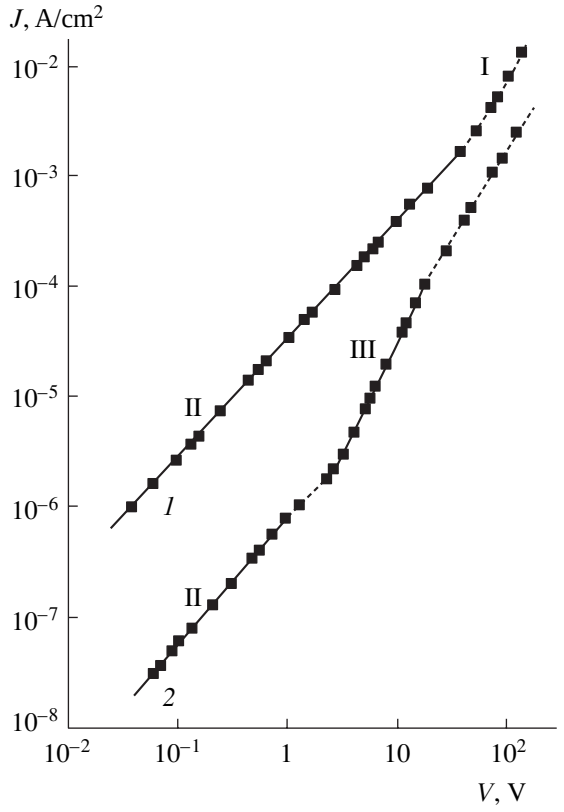

Fig. 2. Current–voltage characteristics for two PAQ samples with different electrodes at 20°C: (*1*) Pt–PAQ–Pt, the sample thickness is 298 μm and the diameter of electrodes is 4.5 mm; (*2*) Al–PAQ–Pt, the sample thickness is 180 μm, and the diameter of electrodes is 9 mm.

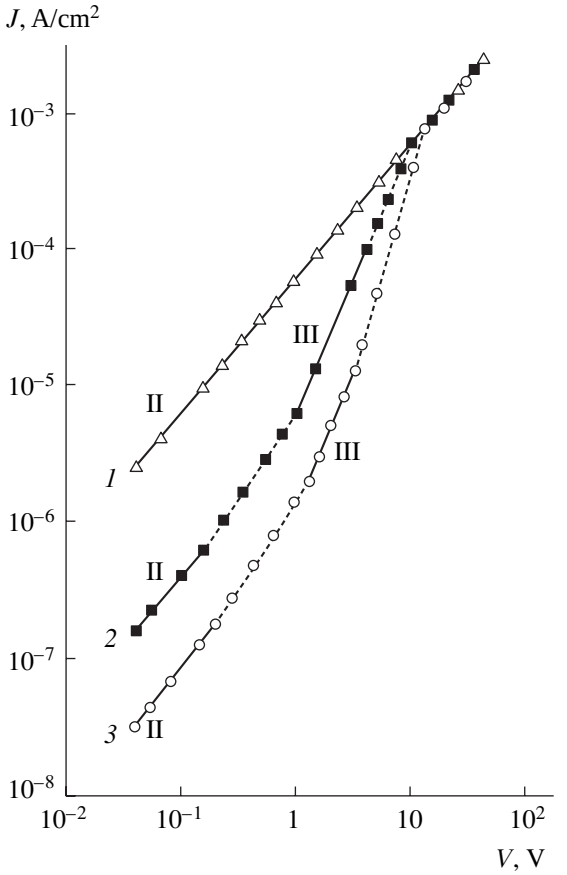

Fig. 3. Effect of the electrode material on the PAQ current–voltage characteristics at 20°C. The sample is the same as in Fig. 1: (*1*) Ag–PAQ–Ag; (*2*) Sn–PAQ–Ag; and (*3*) Al–PAQ–Ag.

This implies that the current–voltage characteristic for the Al–PAQ contact in the segment IV (Fig. 3, curve *3*) depends upon processes in the bulk of a pressed sample, whereas the regime of currents limited by the space charge is realized not in the polymeric material but in the intermediate high-resistivity layer separating Al and PAQ. The allowance for such intermediate (transition) layers represents an obligatory element in modern models of injection-contact phenomena [6]. However, the nature of these layers is different. They can be associated, in particular, with oxide films on the surface of a metal or a semiconductor [6]. In the experimental situation under discussion (Fig. 3, curves *2*, *3*), the presence of aluminum oxide or tin oxide is probably revealed. This is confirmed by the results of special test experiments. The current–voltage characteristics shown in Fig. 3 demonstrate the practical realization of the so-called "dirty contacts" method. This method was recommended in [7] for checking formation conditions for the case of ohmic contact with organic semiconductors.

However, the reaction of this "dirty contact" to the alternating electric field in conditions of bias voltage is similar to the behavior of certain specially produced chemically and technologically complicated inorganic heterostructures [5, 8, 9]. At present, properties of these objects are insufficiently understood. Nevertheless, their investigation opens new possibilities in both fundamental science and the application of fundamentally new instrumentation [9, 10].

Indeed, in an equivalent scheme, the symmetric capacity–voltage characteristic (Fig. 1) corresponds not to the usual Schottky barrier characteristic of metal–semiconductor contacts [5] but to two Schottky diodes switched in towards one another [5, 8, 9]. This indicates a specific structure of the potential relief at the PAQ–aluminum-oxide heteroboundary intrinsic to isotypical heterostructures with the double depletion [5, 8, 9]. However, in these structures, depleted layers are localized at both sides of the heteroboundary [5, 8, 10]. In this case, the slope of the linear (in the C^{-2}–V coordinates) dependence, as a rule, is different. In the framework of the well-known model of barrier capacitance [11], this fact is unambiguously determined by the level of the doping of contacting semiconductors [8]. At the same time, as is seen in Fig. 4 for the case of PAQ, the slope of the capacity–voltage characteristic in the C^{-2}–V coordinates is the same for both polarities of the bias

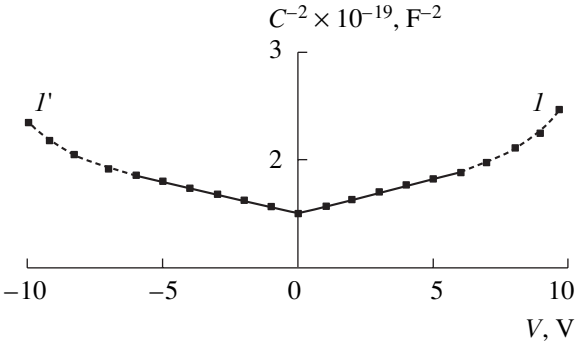

Fig. 4. Current–voltage characteristic for the Al–PAQ–Ag system in C^{-2}–V coordinates at 20°C of PAQ temperature. The synthesis duration is 5 h; the frequency is 0.4 kHz; the sample thickness is 570 μm, the diameter of electrodes is 9 mm; and $N_{ion} = 1.1 \times 10^{-14}$ cm^{-3}.

voltage. In other words, this slope is independent of the fact of which bias (direct or reverse) is applied to each of the two Schottky diodes in the double-depletion model.

According to our data for PAQ [3], the concentration N_{ion} of ionized centers in the space charge region at a synthesis duration of 24 h turned out close to the value $\bar{n} = 2 \times 10^{16}$ cm^{-3} of the Hall concentration of charge carriers. (The PAQ samples under study purposefully were not doped.) As far as we know from [12], there exist no commonly used methods for analysis of capacitive measurements in disordered semiconductors. The results of measurements of the Hall constant in conditions of the hopping conduction [13] and in granular media [14] also deserve a particular analysis. Nevertheless, the observed equality $N_{ion} \approx \bar{n}$ is apparently nonrandom and reveals the general nature of processes determining the Hall emf and screening the electric field in PAQ. Moreover, a decrease in the value of N_{ion} by two orders of magnitude, while reducing the synthesis duration from 24 [3] to 5 h (Fig. 4), indicates the probable sensitivity of the capacity–voltage characteristic method to conditions of the PAQ synthesis.

We can explain the totality of these experimental facts only under the assumption that the system of deep energy levels, which functionally is equivalent to the double Schottky diode, is associated with states localized only at one side of the Al_2O_3–PAQ heteroboundary, i.e., in the space charge region of the polymer. In this case, for PAQ pressed samples, the contribution of the variation in the occupancy of these deep layers to the barrier capacitance of the Al–PAQ contact must represent the collective response of the system of elementary double Schottky diodes to the action of the alternating electric field. These diodes are kinetically stable isotypical heterostructures with local double depletion spontaneously arising in the PAQ granule contact zones. Evidently, this is possible only under the condition of the existence of a correlation in surface layers of the polymer. This is expected from the results of the theoretical study [15] if we take into account the layered structure of graphite-like fragments of the overmolecular PAQ structure [4]. It seems that for PAQ the near-electrode space charge zone represents a strongly correlated system of double self-consistent potential wells connected to intergranular barriers.

REFERENCES

1. V. Mattis, D. Emin, and L. Kazmerski, in *Polycrystalline and Amorphous Thin Films and Devices*, Ed. by L. Kazmerski (Academic, New York, 1980; Mir, Moscow, 1983).
2. V. I. Uglyanets and A. K. Fedotov, Fiz. Tekh. Poluprovodn. (St. Petersburg) **28**, 594 (1994) [Semiconductors **28**, 357 (1994)].
3. R. V. Afanas'eva, T. G. Ermakova, and M. G. Voronkov, Dokl. Ross. Akad. Nauk **374**, 473 (2000) [Dokl. Phys. **45**, 507 (2000)].
4. T. G. Ermakova, A. A. Maksimov, L. Ya. Tsarik, *et al.*, Vysokomol. Soedin., Ser. A **44**, 551 (2002).
5. A. G. Milnes and D. L. Feucht, *Heterojunctions and Metal–Semiconductor Junctions* (Academic, New York, 1972; Mir, Moscow, 1975).
6. A. L. Zyuganov and S. V. Svechnikov, *Injection-Contact Phenomena in Semiconductors* (Naukova Dumka, Kiev, 1981).
7. F. Gutmann and L. E. Lyons, *Organic Semiconductors* (Wiley, New York, 1967; Mir, Moscow, 1970).
8. B. L. Sharma and R. K. Purohit, *Semiconductor Heterojunctions* (Pergamon, Oxford, 1974; Sov. Radio, Moscow, 1979).
9. V. I. Strikha, *Contact Phenomena in Semiconductors* (Vysshaya Shkola, Kiev, 1982).
10. Zh. I. Alferov, Usp. Fiz. Nauk **172**, 1068 (2002).
11. L. S. Berman and A. A. Lebedev, *Deep-Level Transient Spectroscopy of Semiconductor* (Nauka, Leningrad, 1981).
12. A. A. Simashkevich and S. D. Shutov, Fiz. Tekh. Poluprovodn. (St. Petersburg) **28**, 133 (1994) [Semiconductors **28**, 80 (1994)].
13. Yu. M. Gal'perin, E. P. German, and V. G. Karpov, Zh. Éksp. Teor. Fiz. **99**, 343 (1991) [Sov. Phys. JETP **72**, 193 (1991)].
14. S. A. Azimov and Sh. B. Atakulov, *Kinetic Phenomena in Polycrystalline Films of Lead Chalcogenides* (Tashkentsk. Fiz. Inst., Tashkent, 1985).
15. F. G. Pikus and A. L. Efros, Zh. Éksp. Teor. Fiz. **96**, 985 (1989) [Sov. Phys. JETP **69**, 558 (1989)].

Translated by G. Merzon

Doklady Physics, Vol. 48, No. 11, 2003, pp. 602–607. Translated from Doklady Akademii Nauk, Vol. 393, No. 1, 2003, pp. 36–41.

PHYSICS

Energy of Interatomic Bonds, Phonon Spectra, and Polymorphism of Ca and Sr Chemical Elements

N. N. Sirota

Presented by Academician O.A. Bannykh June 4, 2003

Received June 4, 2003

The problem of polymorphism [1] is one of the central problems in physics of condensed matter. In most cases, the polymorphism of a chemical element, in particular of thermal and baric origin, is predominantly determined by its crystal-lattice dynamics (see [1–4]).

In the present paper, which is based on the atomic statistical theory, we quantitatively analyze conditions related to the polymorphism of the chemical elements Ca and Sr for the first time. A method is proposed for determining the atomic screening coefficient for an atom that forms bonds with another atom of a given coordination sphere using atoms of preceding coordination spheres. The calculated values for both equilibrium temperatures of polymorphic transitions and thermodynamic characteristics of polymorphic modifications turn out to be consistent with available experimental data.

While considering polymorphism of Ca and Sr, we use harmonic approximation and restrict our analysis by clarifying an effect of the temperature polymorphism on the coupling energy $U(\delta)$ and phonon spectra of Ca and Sr using Helmholtz free energy F and its derivatives.

Table 1 shows the electron structures of atoms and basic thermodynamic properties of corresponding chemical elements.

The energy U_0 of interatomic bonds at temperature $T \approx 0$ for quiescent atoms is mainly determined by the distribution function of electron density ρ of external bonding electrons in the crystal lattice. We now use the approximation of the simplified variant of the Thomas–Fermi–Dirac–Gambös atomic statistical theory for a spherical atom [5–8]. In this approximation, the energy $u(\delta)$ of a single bond between quiescent atoms situated at the distance δ one from the other is determined by the difference between the exchange energy u_a and a half of the kinetic energy $\frac{1}{2}u_k$ of bonding electrons as well as by the correlation energies u_ω and Coulomb interaction energy u_C. For condensed phases formed by atoms of the same kind, the estimate of the coupling energy can be restricted to sufficient accuracy if we allow for only u_k, u_a, and, partly, for u_ω. All these components are dependent on the distribution of the electron density ρ [5]. In the accepted approximation, we omit the electrostatic component of the interaction energy, which is inherent in systems composed of the same atoms. We also omit the variation of the electron density in the process of crystal formation compared to an isolated atom. The kinetic energy of bonding electrons is proportional to $\rho^{5/3}$, whereas according to Dirac, the exchange energy is proportional to $\rho^{4/3}$.

At the distance equal to half of the bond length $\delta/2$ between atoms A and B of the same kind, the contributions of their electron densities $\rho_{A_{1/2}}$ and $\rho_{B_{1/2}}$ are equal, i.e., $\rho_{A_{1/2}} = \rho_{B_{1/2}} = \rho$. Correspondingly, the difference in volume densities of a half of the kinetic energy $\frac{1}{2}\left(\frac{\partial u_k}{\partial V}\right)$ and of the exchange energy $\left(\frac{\partial u_a}{\partial V}\right)$ at a given point of the plane normal to the line connecting the atoms is (at the midpoint of this length)

$$\frac{1}{2}\left(\frac{\partial u_k}{\partial V}\right)_{1/2} - \left(\frac{\partial u_a}{\partial V}\right)_{1/2}$$
$$= \frac{1}{2}\kappa_k[(\rho_A + \rho_B)^{5/3} - \rho_A^{5/3} - \rho_B^{5/3}]$$
$$- \kappa_a[(\rho_A + \rho_B)^{4/3} - \rho_A^{4/3} - \rho_B^{4/3}]$$

or

$$\frac{1}{2}\left(\frac{\partial u_k}{\partial V}\right)_{1/2} - \left(\frac{\partial u_a}{\partial V}\right)_{1/2} = 0.578\kappa_k\rho^{5/3} - 0.52\kappa_a\rho^{4/3}. \quad (1)$$

Here, $\kappa_k = 2.871e^2a_0$ and $\kappa_a = 0.7386e^2$ are constants of the atomic statistical theory.

The density distribution of electron gas for external bonding electrons in a spherical atom can be approximated as usual by the first term of expansion in the

Moscow State University of Environmental Engineering, ul. Pryanishnikova 9, Moscow, 127550 Russia

1028-3358/03/4811-0602$24.00

Table 1. Atomic mass, electron structure of an atom, atomization energy, type of the crystal structure, characteristic temperature θ, entropy *S*, and temperatures of polymorphic transitions T_k for chemical elements Ca and Sr

Chemical element	Ordering number	Atomic mass [14]	Electron structure [14]	Radius of the external orbital, Å [13]	Type of structure	Lattice parameters *a*, *c*, Å [14]	Closest interatomic distance	Atomization energy [14]		Transition temperature T_k, K [14]	θ, K [13]	S_{298}, J/(mol K) [13]	θ according to S_{298}, K
								kJ/mol	Ry				
Ca	20	40.078	[Ar] $4S^2$	1.690	A_1	5.5884	7.4688	178.2	0.1355	573	220	41.63	216.6
					A_2	4.48	7.3540			723			
					A_3	3.97, 6.49	7.5047						
Sr	38	55.847	[Kr] $5S^2$	1.836	A_1	6.0849	8.132	164.4	0.125	506	129	52.3	142.5
					A_2	4.32, 7.06	8.185			813			
					A_3	4.85	7.94						

Gauss function $\rho = Ae^{\gamma r^2}$, where *r* is the distance counted off from the center of the atom and γ is the semiempiric multiplier connected to the reciprocal value of the averaged radius squared of external-electron orbitals.

The normalization condition for the number *N* of electrons forming the bonds, the magnitude of the preexponential multiplier *A* is

$$A = \frac{N}{4\pi\int_0^\infty r^2 e^{-\gamma r^2} dr} = 0.1796\gamma^{1.5}N. \quad (2)$$

We now write out the volume energy density for the difference of the kinetic and exchange energies of the electron gas at a certain point of the plane normal to the line connecting the atoms A and B. At the midpoint of the line, this energy density is written out as

$$\left(\frac{\partial u}{\partial V}\right)_{1/2} = \frac{1}{2}\left(\frac{\partial u_k}{\partial V}\right)_{1/2} - \left(\frac{\partial u_a}{\partial V}\right)_{1/2}$$

$$= 0.587\kappa_k A^{5/3}\exp\left(-\frac{5}{3}\gamma r^2\right) - 0.52\kappa_a A^{4/3}\exp\left(-\frac{4}{3}\gamma r^2\right). \quad (3)$$

In the case of an axisymmetric shape of the bonding electron cloud, the distance squared r^2 from the center of the atom to the given point of the plane normal to the bond line at the midpoint of its length is

$$r^2 = \left(\frac{\delta}{2}\right)^2 + y^2,$$

where *y* is the distance from the bonding line to the given point. The passage from the volume energy density to the linear energy density *u* along the bond at its midpoint can be written out in the form

$$\left(\frac{\partial u}{\partial \delta}\right)_{1/2} = 0.587\kappa_k A^{5/3}\exp\left(-\frac{5}{3}\gamma\left(\frac{\delta}{2}\right)^2\right)$$

$$\times 2\pi\int_0^\infty y\exp\left(-\frac{5}{3}\gamma y^2\right)dy - 0.52\kappa_a A^{4/3}\exp\left(-\frac{4}{3}\gamma\left(\frac{\delta}{2}\right)^2\right)$$

$$\times 2\pi\int_0^\infty y\exp\left(-\frac{4}{3}\gamma y^2\right)dy. \quad (4)$$

Assuming the bonding electron cloud to be spindle-shaped and approximating the linear bonding-energy density by a function of the form proposed in [9], after integrating along the bond line, we find the energy $u(\delta)$ of the pair bond. In this case, the role of the correlation component u_ω is taken into account by the coefficient $\kappa_a' = 0.8349e^2$, $\frac{\kappa_a'}{\kappa_a} = 1.065$. Thus, we obtain

$$u(\delta) = -0.152\gamma N^{4/3}\exp\left(-\frac{4}{3}\gamma\left(\frac{\delta}{2}\right)^2\right)$$

$$\times\left[1 - 1.982N^{1/3}\gamma^{1/2}\exp\left(-\frac{1}{3}\gamma\left(\frac{\delta}{2}\right)^2\right)\right]. \quad (5)$$

The quantities γ and *N* may be considered as variational parameters.

Summing the pair coupling energy for an atom placed into the origin of coordinates with all interacting atoms of all coordination spheres *i* taken into account, we arrive at the total coupling energy corresponding to one atom:

$$U(\delta) = l\sum_i z_{\text{eff}_i} u(\delta_i), \quad (6)$$

where *l* is a correcting coefficient.

Table 2. Values of coefficients $K_i^2 = \left(\frac{r_i}{r_1}\right)^2$ taken in the calculations for various types of structure and for the coordination spheres i = I–VII

Type of structure	K_i^2						
	I	II	III	IV	V	VI	VII
A_1	1	2	3	4	5	6	7
A_2	1	1.33	2.66	3.66	4	5.33	6.33
A_3	1	2	2.66	3	3.66	4	5

Table 3. De Launay force constants α_i/β_i taken in the calculations, coefficients γ, and numbers N of bonding electrons for chemical elements Ca and Sr

Chemical element	Type of structure	$\frac{\alpha_i}{\beta_i}$				γ	N
		I	II	III	IV		
Ca	A_1	$\frac{1.064}{0}$	$\frac{0.154}{0.139}$	$\frac{-0.219}{0.105}$	$\frac{-0.271}{0.056}$	0.222	2.4818
	A_2	$\frac{1.311}{0}$	$\frac{0.429}{0.113}$	$\frac{-0.12}{0.127}$	$\frac{-0.283}{0.076}$	0.220	2.5153
	A_3	$\frac{1.147}{0}$	$\frac{0.057}{0.136}$	$\frac{-0.215}{0.106}$	$\frac{0.269}{0.086}$	0.212	2.6672
Sr	A_1	$\frac{0.913}{0}$	$\frac{0.055}{0.133}$	$\frac{-0.278}{0.081}$	$\frac{-0.225}{0.035}$	0.225	2.5582
	A_2	$\frac{1.078}{0}$	$\frac{0.018}{0.132}$	$\frac{-0.245}{0.097}$	$\frac{-0.28}{0.076}$	0.226	2.4949
	A_3	$\frac{0.961}{0}$	$\frac{0.522}{0.098}$	$\frac{-0.258}{0.095}$	$\frac{-0.245}{0.041}$	0.216	0.8286

The effective coordination number z_{eff_i} of the ith coordination sphere is smaller than the true coordination number z_i since a portion of the atoms of this sphere are screened by atoms of preceding spheres:

$$z_{\mathrm{eff}_i} = z_i\xi_i. \tag{7}$$

Here, ξ_i is the coefficient for screening of atoms of the ith coordination sphere by atoms of all preceding $(i-1)$th, $(i-2)$th, …, $(i-k)$th spheres.

The value of the screening coefficient ξ_i is taken to be equal to the ratio of the portion of the surface area of the ith sphere unoccupied by the summary surface of projections of atoms from preceding spheres to the total surface area F_i of the ith sphere. The area of projections of atoms of preceding $(i-1)$th, $(i-2)$th, …, $(i-k)$th spheres onto the ith surface is determined by the sum of products of the coordination number z_{i-k} by the surface area S_{i-k} of the atom projection:

$$\xi_i = \frac{F_i - \sum z_{i-k}S_{i-k}}{F_i} = 1 - \frac{\sigma}{F_1}\sum\frac{z_{i-k}F_1}{F_{i-k}}. \tag{8}$$

The summation is performed over all preceding $i-k$ spheres. We assume in this case that the area of the projection of an atom of the $(i-k)$th sphere onto the ith sphere is

$$S_{i-k} = \sigma\frac{F_i}{F_{i-k}},$$

where σ is the area of the principal cross section of an atom and $\frac{S_i}{S_{i-k}} = \frac{F_i}{F_{i-k}}$. The ratio of the surface area F_{i-k} of the $(i-k)$th sphere to the surface area F_1 of the first sphere corresponds to the ratio of the radii squared of these spheres:

$$\frac{F_{i-k}}{F_1} = \frac{r_{i-k}^2}{r_1^2} = K_{i-k}^2.$$

Then,

$$\xi_i = 1 - \eta S_0\sum\frac{z_{i-k}}{K_{i-k}^2}, \tag{9}$$

where η determines both the rate of a decrease in the contribution of coordination spheres with increasing their number and the probability of covering the projections of atoms of preceding spheres. The ratio $\frac{\sigma}{F_1}$ is a constant lying between 0.025 and 0.0625 for various structures. In what follows, we conventionally set $\eta S_0 = 0.025$ taking into account seven spheres.

The interatomic interaction energy $U(\delta)$ as a function of the interatomic distance δ between atoms at rest is calculated by formula (6) for structures A_1, A_2, and A_3. These calculations are based on the low-temperature modification for which γ and N corresponding to known atomization energy $U_0(\delta)$ and interatomic distance δ_0 are calculated. For high-temperature modifications, γ and N are determined with inclusion of the polymorphic transition temperatures T_k. Tables 1–3 present the input data for calculations.

Figure 1 shows $U(\delta)$ curves for various modifications of Ca and Sr. The atomization energies of atoms at rest are determined from minima of $U_0(\delta)$. Using functions $U(\delta)$, the de Launay force constants [10, 11]

$$\alpha_{ikj} = \left(\frac{\partial^2 U}{\partial\delta^2}\right)_{ikj}, \quad \beta_{ikj} = \frac{1}{\delta_{ij}}\left(\frac{\partial U}{\partial\delta}\right)_{ikj} \tag{10}$$

for modifications k = 1, 2, and 3 are calculated at points corresponding to the radii of four coordination spheres

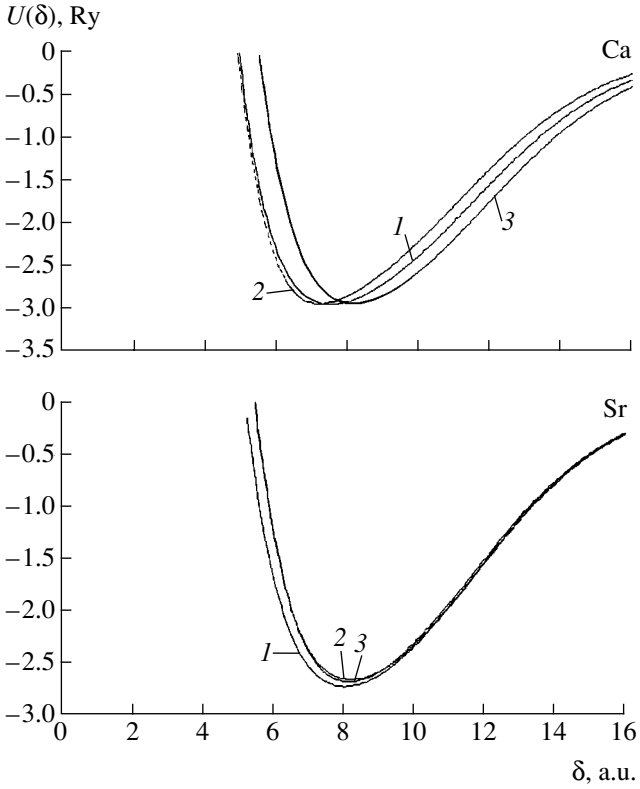

Fig. 1. Energy $U(\delta)$ of interatomic bonds as a function of the distance δ between closest atoms in modifications of chemical elements with the indicated types of structure. Ca: (*1*) A_1; (*2*) A_2; (*3*) A_3. Sr: (*1*) A_1; (*2*) A_3; (3) A_2.

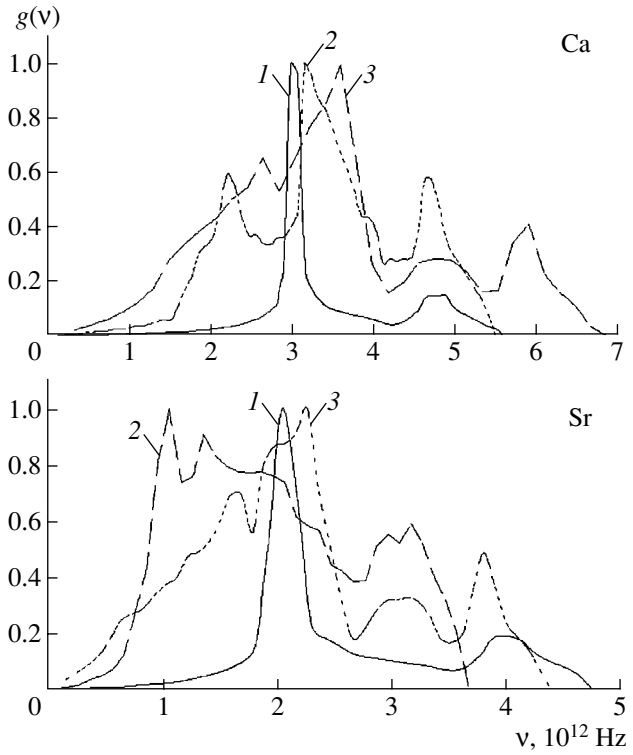

Fig. 2. Phonon spectra for modifications of chemical elements: Ca: (*1*) A_1; (*2*) A_2; (*3*) A_3. Sr: (*1*) A_1; (*2*) A_3; (*3*) A_2.

i of the *j*th element. These constants used for calculations of phonon spectra are presented in Table 3.

Phonon spectra are calculated by the Born–Karman–Blackman method based on solving the secular equation with the Born–Karman dynamical matrix

$$\left|D(q) - \omega^2 m\right| = 0. \qquad (11)$$

Sampling of calculated points from 1/48 of the Brillouin zone is carried out by the Monte Carlo method [12]. Figure 2 shows the phonon spectra calculated for modifications of Ca and Sr by the computer program developed by T.D. Sokolovskiĭ with introduced correcting coefficients.

Using the calculated phonon spectra with the frequency density distribution $g(\nu)$, we have derived the temperature dependences for the internal energy

$$U_T = U - U_0 = \int_0^{\nu_m} g(\nu)\bar{\varepsilon}d\nu,$$

heat capacity

$$C_V = \int g(\nu)\frac{\partial\bar{\varepsilon}}{\partial T}d\nu, \quad \bar{\varepsilon} = \frac{h\nu}{e^{h\nu/kT}-1} + \frac{h\nu}{2},$$

and free energy

$$F_T = -F - U_0 = -T\int_0^T \frac{U_T}{T^2}dT.$$

The characteristic temperatures were determined according to the values of C_V for the ratios $\frac{\theta}{T}$ corresponding to the Debye values, as well as according to the value of the entropy at $T = 300$ K.

Figure 3 shows curves of temperature dependences $C_V(T)$ for polymorphic modifications of the A_1, A_2, and A_3 structures for Ca and Sr.

The temperatures $T_{I,II}$ and $T_{II,III}$ of polymorphic transitions for the modifications I and II and II and III, respectively, were found as intersection points $F_I - F_{II} = 0$ and $F_{II} - F_{III} = 0$ of free-energy curves for these modifications (Fig. 4). The differences in the temperature-dependent parts of the free energies F_T for the low-temperature and high-temperature modifications at $T = T_k$ correspond to the difference in the atomization energies for these modifications at $T = 0$. In this case, the difference in zero energies of atomic oscillations is negligibly low.

The chemical elements Ca and Sr have similar electron structures of their atoms with filled-in $4S^2$ and $5S^2$

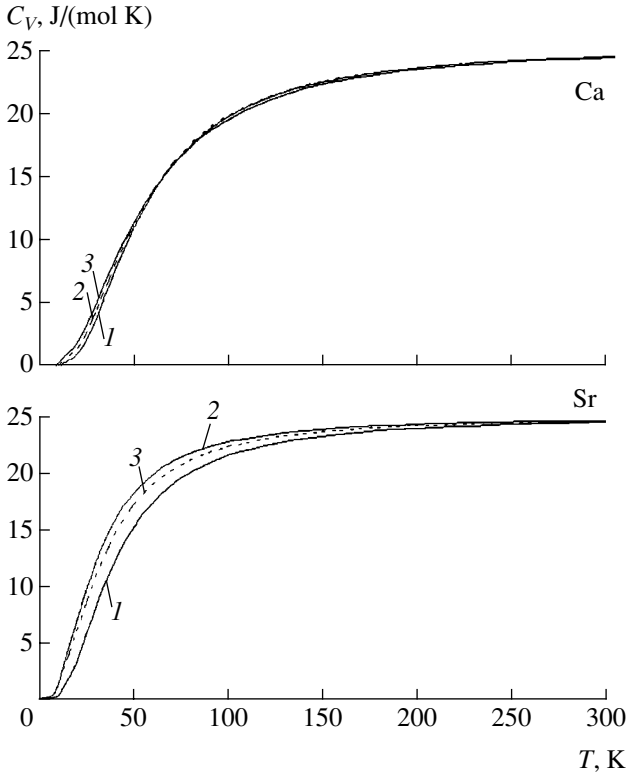

Fig. 3. Temperature dependence of the heat capacity for modifications of chemical elements: Ca: (*1*) A_1; (*2*) A_2; (*3*) A_3. Sr: (*1*) A_1; (*2*) A_3; (*3*) A_2.

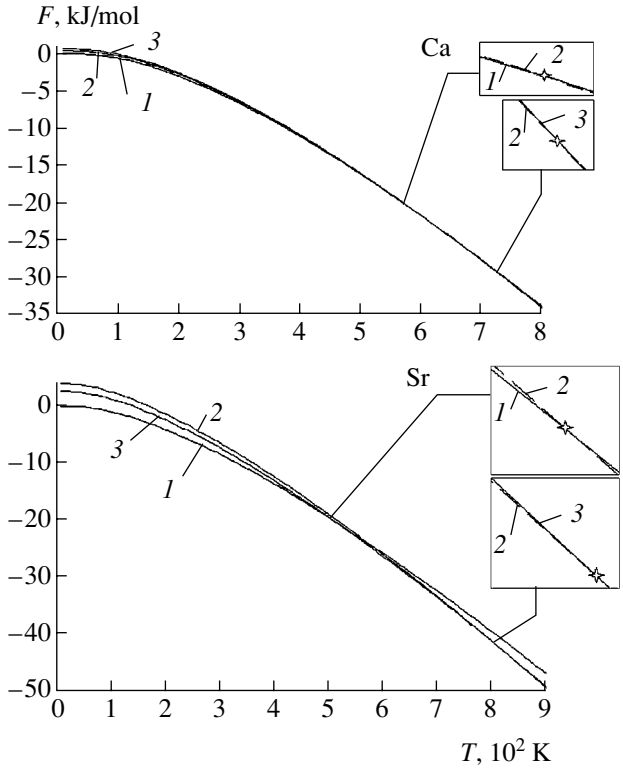

Fig. 4. Temperature dependence of the free energies $F(T)$ for modifications of chemical elements: Ca: (*1*) A_1; (*2*) A_2; (*3*) A_3. Sr: (*1*) A_1; (*2*) A_3; (*3*) A_2.

orbitals, respectively. The cores of these orbitals have structures of Ar and Kr, respectively. In spite of the similarity of external orbitals of Ca and Sr, they differ in the sequence of the modification structures as functions of temperatures: $A_1 \leftrightarrow A_2 \leftrightarrow A_3$ for Ca and $A_1 \leftrightarrow A_3 \leftrightarrow A_2$ for Sr. In this case, there exists a slight difference in

Table 4. Calculated atomization energies U_0 corresponding to the closest interatomic distances δ_0; internal energy U_T and entropy S_T at $T = T_k$; temperatures of polymorphic transitions; Debye characteristic temperatures θ calculated according to C_V at 100, 200, and 300 K and according to the value S_T = 300 K for modifications of chemical elements Ca and Sr

Chemical element	Type of structure	U_0, Ry	δ_0, a.u.	U_T at $T = T_k$, kJ/mol	S_T, J/(mol K)		T_k, K	θ, K			
					$T = T_k$	T = 300 K		at 100 K	at 200 K	at 300 K	according to S_{300}
Ca	A_1	−0.1355	7.47	12.1896	0.0565	0.0408	568	222	225	225	225
	A_2	−0.1352	7.19	12.2230 / 16.1651	0.0572 / 0.0633	0.0415	727	220	223.5	224	219
	A_3	−0.1350	8.1	16.1257	0.0650	0.0419		227.5	232.5	235	216
Sr	A_1	−0.1250	8.03	10.9915	0.0608	0.0481	501	171.5	174	175	168
	A_2	−0.1230	8.1	11.2315 / 18.8922	0.0665 / 0.0784	0.0538	809	147	149	150.5	135
	A_3	−0.1220	8.17	19.0030	0.0802	0.0555		133.5	135.5	141	125

Note: For modifications A_2 (Ca) and A_3 (Sr) two values of U_T and S_T are given. For Ca, the values above and under the lines correspond to the temperatures of the $A_1 \leftrightarrow A_2$ and $A_2 \leftrightarrow A_3$ transitions, respectively. For Sr, the values above and under the lines correspond to the temperatures of the $A_1 \leftrightarrow A_3$ and $A_3 \leftrightarrow A_2$ transitions, respectively.

the ratio $\frac{c}{a}$ for the A_3 modification. This fact can be associated with a difference in the polarizability of the atoms and sizes of their cores.

In Table 4, the values of a number of parameters calculated in the present paper are listed. They are atomization energies U_0 for polymorphic modifications of Ca and Sr, the closest interatomic distances δ_0 in crystal lattices, temperatures T_k, and energies ΔU_T of transitions, as well as characteristic temperatures $\theta(T)$.

The temperatures of polymorphic transitions and thermodynamic characteristics of modifications of these elements, which were obtained in the calculations, are consistent with available experimental data. Questions associated with estimating the quantity γ and its comparison with the radii of orbitals corresponding to external atomic electrons deserve detailed separate studies.

The methods of estimating screening coefficients for atomic electrons, while forming interatomic bonds in crystals turned out rather efficient, nevertheless, they need refinement. Analysis of the polymorphism of chemical elements (with Ca and Sr as examples), with application of the methods based on the statistical atomic theory, testifies to their high efficiency and, at the same time, to the expediency of their further development.

REFERENCES

1. A. R. Verma and P. Krishna, *Polymorphism and Polytypism in Crystals* (Wiley, New York, 1966; Mir, Moscow, 1969).
2. M. Born and K. Huang, *Dynamical Theory of Crystal Lattices* (Clarendon, Oxford, 1954; Inostrannaya Literatura, Moscow, 1958).
3. G. Leibfirid, *Microscopy Theory of Mechanical and Thermal Properties of Crystals* (Gos. Izd. Fiz. Mat. Lit., Moscow, 1963).
4. N. N. Sirota, Dokl. Akad. Nauk **382**, 45 (2002) [Dokl. Phys. **47**, 16 (2002)].
5. P. Gambosh, *Statistical Theory of Atom and Its Application* (Inostrannaya Literatura, Moscow, 1951).
6. M. G. Veselov and L. N. Labzovskiĭ, *Atomic Theory: Electron Shell Structure* (Nauka, Moscow, 1986).
7. S. Lundqvist and N. H. March, *Theory of Inhomogeneous Electron Gas* (Plenum, New York, 1983; Mir, Moscow, 1987).
8. N. N. Sirota, I. M. Sirota, T. M. Soshnina, and T. D. Sokolovskiĭ, Fiz. Tverd. Tela (St. Petersburg) **43**, 1674 (2001) [Phys. Solid State **43**, 1743 (2001)].
9. N. N. Sirota and T. M. Soshnina, Dokl. Akad. Nauk Belarusi **47** (1), 45 (1997).
10. J. De Launay, Solid State Phys. **2**, 219 (1956).
11. S. C. Upadhyaya, Phys. Rev. B **44**, 122 (1991).
12. *Chemical Bonds in Semiconductors and Solids*, Ed. by N. N. Sirota (Consultants Bureau, New York, 1967), pp. 139–141.
13. *Metals*, Ed. by G. V. Samsonov (Metallurgiya, Moscow, 1976).
14. J. Emsley, *The Elements* (Clarendon, Oxford, 1989; Mir, Moscow, 1993).

Translated by G. Merzon

Doklady Physics, Vol. 48, No. 11, 2003, pp. 608–611. Translated from Doklady Akademii Nauk, Vol. 393, No. 2, 2003, pp. 176–179.

PHYSICS

On Calculating Spectral Intensities for Anomalous Average Values in the Theory of Superconductors with Strong Electron Correlations

V. V. Val'kov*, D. M. Dzebisashvili, and A. S. Kravtsov*****

Presented by Academician K.S. Aleksandrov April 28, 2003

Received May 7, 2003

In this paper, we show that allowance for properties of the Hubbard operator algebra leads to the appearance of a singular (at $\omega = 0$) component in the total spectral intensity of the anomalous correlation function of superconductors that possess the electron pairing mechanism. In this case, the spectral theorem acquires the form of a singular integral equation. Taking these features into account, we can eliminate previously claimed forbidding of realization of the superconducting phase with the *S*-type symmetry of the order parameter.

1. While constructing a theory of high-temperature superconductors which is based on the electron pairing mechanism, the two following methods are most widely employed. The first approach uses the diagram technique for Hubbard operators [1, 2]. The second one is based on the formalism of irreversible retarded two-time Green's functions [3]. Previously, the scattering amplitude calculated for the Hubbard model [4] in the regime of strong electron correlations [1] was analyzed in the paramagnetic phase. It was shown that in the Cooper channel, this amplitude has a singularity corresponding to the transition into the superconducting phase (Zaĭtsev mechanism) [2]. While analyzing this phase on the basis of retarded Green's functions, the spectral theorem [5] was used, which made it possible to obtain self-consistency equations for calculating normal and anomalous average values. It turned out that at $f = g$, the anomalous average values $\langle X_{\mathbf{g}}^{0\sigma} X_{\mathbf{f}}^{0\bar{\sigma}} \rangle$, ($X_{\mathbf{g}}^{0\sigma}$ and $X_{\mathbf{f}}^{0\bar{\sigma}}$ are Hubbard operators [6]) calculated according to this rule for the superconducting phase with the *S*-type symmetry of the order parameter do not satisfy the evident requirement $\langle X_{\mathbf{f}}^{0\sigma} X_{\mathbf{f}}^{0\bar{\sigma}} \rangle = 0$ [3]. This violation of the sum rule has constituted the statement on forbidding the superconducting state of the *S*-type.

We now show that the origin of this forbidding is exclusively associated with ignoring the singular (at $\omega = 0$) component of the spectral intensity of the anomalous correlation function $\langle X_{\mathbf{g}}^{0\sigma}(t') X_{\mathbf{f}}^{0\bar{\sigma}}(t) \rangle$. With this statement taken into account, we can satisfy necessary requirements for anomalous correlators in limiting cases without any variation of the form of the previously obtained self-consistency equations for the superconducting phase. The approach developed allows us to overcome problems that arise when describing the superconducting phase with the *S*-type symmetry of the order parameter.

2. Before analyzing features of spectral representations for the correlation functions $\langle X_{\mathbf{g}}^{0\sigma}(t') X_{\mathbf{f}}^{0\bar{\sigma}}(t) \rangle$, we pay attention to the fundamental distinction between the anomalous Green's function in the BCS theory and the anomalous Green's function in the theory of high-temperature superconductivity based on the electron pairing mechanism. The anomalous Green's function constructed on usual Fermi operators of secondary quantization

$$F_{\sigma\bar{\sigma}}(\mathbf{f}t; \mathbf{g}t') = -i\theta(t-t')\langle\{a_{\mathbf{f}\sigma}^{+}(t), a_{\mathbf{g}\bar{\sigma}}^{+}(t')\}\rangle$$

is zero when $t = t' + \delta$, $\delta \to +0$. This is associated with the anti-commutativity of Fermi production operators at coinciding times. At the same time, the time-average values $\langle a_{\mathbf{f}\sigma}^{+}(t) a_{\mathbf{g}\bar{\sigma}}^{+}(t) \rangle$ and $\langle a_{\mathbf{g}\bar{\sigma}}^{+}(t) a_{\mathbf{f}\sigma}^{+}(t) \rangle$ in the superconducting phase can be nonzero in their own right (and opposite in their signs) even at $\mathbf{f} = \mathbf{g}$:

$$\langle a_{\mathbf{f}\sigma}^{+} a_{\mathbf{f}\bar{\sigma}}^{+} \rangle = \eta(\sigma)\langle X_{\mathbf{f}}^{20} \rangle, \quad \langle a_{\mathbf{f}\bar{\sigma}}^{+} a_{\mathbf{f}\sigma}^{+} \rangle = -\eta(\sigma)\langle X_{\mathbf{f}}^{20} \rangle,$$
$$\eta(\sigma) = 2\sigma.$$

* *Kirensky Institute of Physics, Siberian Division, Russian Academy of Sciences, Krasnoyarsk, 660036 Russia*
e-mail: vvv@iph.krasn.ru

** *Krasnoyarsk State Technological University, Krasnoyarsk, 660074 Russia*
e-mail: ddm@iph.krasn.ru

*** *Krasnoyarsk State University, Krasnoyarsk, 660075 Russia*
e-mail: ask@iph.krasn.ru

1028-3358/03/4811-0608$24.00

Another situation takes place for the anomalous Green's function constructed on Hubbard operators,

$$\langle\langle X_{\mathbf{f}}^{\bar{\sigma}0}(t)\big|X_{\mathbf{g}}^{\sigma 0}(t')\rangle\rangle = -i\theta(t-t')\langle\{X_{\mathbf{f}}^{\bar{\sigma}0}(t), X_{\mathbf{g}}^{\sigma 0}(t')\}\rangle. \quad (1)$$

In this case, for $t \to t' + 0$, the average values $\langle X_{\mathbf{f}}^{\bar{\sigma}0} X_{\mathbf{g}}^{\sigma 0}\rangle$ and $\langle X_{\mathbf{g}}^{\sigma 0} X_{\mathbf{f}}^{\bar{\sigma}0}\rangle$ entering into the definition of the Green's function identically vanish as long as the site indices turn out to be equal. It is important that such a situation occurs not by virtue of features of a physical system but as a result of the algebra of the Hubbard operator multiplication. The independence of this fact of particular physical conditions makes it possible to explicitly take it into account at the spectral-representation level.

Keeping in mind this feature, we can write out the spectral intensity $\tilde{J}_{\mathbf{gf}}^{\sigma\bar{\sigma}}(\omega)$ in the spectral representation

$$\langle X_{\mathbf{g}}^{\sigma 0}(t') X_{\mathbf{f}}^{\bar{\sigma}0}(t)\rangle = \int d\omega \exp\{-i\omega(t-t')\}\tilde{J}_{\mathbf{gf}}^{\sigma\bar{\sigma}}(\omega), \quad (2)$$

as

$$\tilde{J}_{\mathbf{gf}}^{\sigma\bar{\sigma}}(\omega) = J_{\mathbf{gf}}^{\sigma\bar{\sigma}} - \delta(\omega)\delta_{\mathbf{fg}}\int d\omega_1 J_{\mathbf{gf}}^{\sigma\bar{\sigma}}(\omega_1)\exp(-i\omega_1\delta), \quad \delta \to +0. \quad (3)$$

This form ensures the elimination of the right-hand side in expression (2) at $t = t' + \delta$, $\delta \to +0$ as far as $\mathbf{f} = \mathbf{g}$ and provides the basic distinction of the introduced spectral representation form that usually is applied in the theory of two-time temperature Green's functions [5].

We now on the basis of representation (2) are able construct the spectral representation of the anomalous correlation function $\langle X_{\mathbf{f}}^{\bar{\sigma}0}(t), X_{\mathbf{g}}^{\sigma 0}(t')\rangle$. In this case, using the property of cyclic transpositivity of operators under the trace sign, we obtain from representation (2)

$$\langle X_{\mathbf{f}}^{\bar{\sigma}0}(t) X_{\mathbf{g}}^{\sigma 0}(t')\rangle = \int d\omega \exp\{-i\omega(t-t')\} \times \{J_{\mathbf{gf}}^{\sigma\bar{\sigma}}(\omega)\exp(\beta\omega) - \delta(\omega)\delta_{\mathbf{fg}} S_{\mathbf{fg}}^{\bar{\sigma}\sigma}\}, \quad (4)$$

$$S_{\mathbf{fg}}^{\bar{\sigma}\sigma} = \int d\omega_1 J_{\mathbf{gf}}^{\sigma\bar{\sigma}}(\omega_1)\exp(\beta\omega_1)\exp(-i\omega_1\delta), \quad \beta = \frac{1}{T}, \quad \delta \to +0. \quad (5)$$

It is seen that also in this case, for $\mathbf{f} = \mathbf{g}$ and $t \to t' + 0$, as it must, the right-hand side vanishes, and $\langle X_{\mathbf{f}}^{\bar{\sigma}0} X_{\mathbf{f}}^{\sigma 0}\rangle = 0$.

Applying spectral representations (2) and (4), we find the expression for the average value of the anticommutator entering into the definition of the anomalous Green's function:

$$\langle\{X_{\mathbf{f}}^{\bar{\sigma}0}(t), X_{\mathbf{g}}^{\sigma 0}(t')\}_+\rangle = \int d\omega \exp\{-i\omega(t-t')\} \times \{J_{\mathbf{gf}}^{\sigma\bar{\sigma}}(\omega)[\exp(\beta\omega)+1] - \delta(\omega)\delta_{\mathbf{fg}}\Sigma_{\mathbf{gf}}^{\sigma\bar{\sigma}}\}, \quad (6)$$

where

$$\Sigma_{\mathbf{gf}}^{\sigma\bar{\sigma}} = \int d\omega_1 J_{\mathbf{gf}}^{\sigma\bar{\sigma}}(\omega_1)[\exp(\beta\omega_1)+1] \times \exp(-i\omega_1\delta), \quad \delta \to +0. \quad (7)$$

From definition (1) with allowance for (6), we find the Fourier transform of the anomalous Green's function

$$\langle\langle X_{\mathbf{f}}^{\bar{\sigma}0}\big|X_{\mathbf{g}}^{\sigma 0}\rangle\rangle_\omega = \int \frac{d\omega_1}{\omega - \omega_1 + i\delta} \times \{J_{\mathbf{gf}}^{\sigma\bar{\sigma}}(\omega)(\exp(\beta\omega)+1) - \delta(\omega)\delta_{\mathbf{fg}}\Sigma_{\mathbf{gf}}^{\sigma\bar{\sigma}}\}. \quad (8)$$

Hence in this case, the spectral theorem [5] acquires the form of the integral equation with respect to $J_{\mathbf{gf}}^{\sigma\bar{\sigma}}(\omega)$

$$-\frac{1}{\pi}\frac{\mathrm{Im}\langle\langle X_{\mathbf{f}}^{\bar{\sigma}0}\big|X_{\mathbf{g}}^{\sigma 0}\rangle\rangle_{\omega+i\delta}}{\exp(\beta\omega)+1} = J_{\mathbf{gf}}^{\sigma\bar{\sigma}}(\omega) - \frac{\partial(\omega)\delta_{\mathbf{fg}}}{\exp(\beta\omega)+1} \times \int d\omega_1 J_{\mathbf{gf}}^{\sigma\bar{\sigma}}(\omega_1)[\exp(\beta\omega_1)+1]\exp(-i\omega_1\delta). \quad (9)$$

It is easy to see that the solution to this equation can be written out in the form

$$J_{\mathbf{gf}}^{\sigma\bar{\sigma}}(\omega) = R_{\mathbf{gf}}^{\sigma\bar{\sigma}}(\omega) + \delta(\omega)\delta_{\mathbf{fg}}\frac{A_{\mathbf{ff}}^{\sigma\bar{\sigma}}}{\exp(\beta\omega)+1}, \quad (10)$$

where

$$R_{\mathbf{gf}}^{\sigma\bar{\sigma}}(\omega) = -\frac{1}{\pi}\frac{\mathrm{Im}\langle\langle X_{\mathbf{f}}^{\bar{\sigma}0}\big|X_{\mathbf{g}}^{\sigma 0}\rangle\rangle_{\omega+i\delta}}{\exp(\beta\omega)+1}, \quad (11)$$

and $A_{\mathbf{ff}}^{\sigma\bar{\sigma}}$ is an arbitrary constant. When deriving (10), we took into account that the equality

$$\int d\omega \exp(-i\omega\delta)\mathrm{Im}\langle\langle X_{\mathbf{f}}^{\bar{\sigma}0}\big|X_{\mathbf{g}}^{\sigma 0}\rangle\rangle_{\omega+i\delta} = 0, \quad (12)$$

which is a part of more generally evident relation

$$\langle\langle X_{\mathbf{f}}^{\bar{\sigma}0}(t)\big|X_{\mathbf{g}}^{\sigma 0}(t')\rangle\rangle_{(t\to t'+\delta)} = \int d\omega \exp(-i\omega\delta)\langle\langle X_{\mathbf{f}}^{\bar{\sigma}0}\big|X_{\mathbf{g}}^{\sigma 0}\rangle\rangle_{\omega+i\delta} = 0, \quad \delta \to +0 \quad (13)$$

takes place.

The ambiguity of the quantity $A_{\mathbf{ff}}^{\sigma\bar{\sigma}}$ is inessential because the total spectral intensity $\tilde{J}_{\mathbf{gf}}^{\sigma\bar{\sigma}}(\omega)$ turns out to be independent of $A_{\mathbf{ff}}^{\sigma\bar{\sigma}}$. Indeed, substituting solution (10) into definition (3), we arrive at

$$\tilde{J}_{\mathbf{gf}}^{\sigma\bar{\sigma}}(\omega) = R_{\mathbf{gf}}^{\sigma\bar{\sigma}}(\omega) - \delta(\omega)\delta_{\mathbf{fg}}\int d\omega_1 R_{\mathbf{gf}}^{\sigma\bar{\sigma}}(\omega_1)\exp(-i\omega_1\delta). \quad (14)$$

In view of this property and also of the fact that according to its form written in (3), $J_{\mathbf{gf}}^{\sigma\bar{\sigma}}(\omega)$ must not contain a singular component at $\omega = 0$, we obtain that the constant $A_{\mathbf{ff}}^{\sigma\bar{\sigma}}$ can be taken to be zero. Thus, it is seen that the analytically continued Fourier transform of the anomalous Green's function determines only the regular part $R_{\mathbf{gf}}^{\sigma\bar{\sigma}}(\omega)$ of the total spectral intensity $\tilde{J}_{\mathbf{gf}}^{\sigma\bar{\sigma}}(\omega)$. In turn, the singular (at $\omega = 0$) component of the total spectral intensity $\tilde{J}_{\mathbf{gf}}^{\sigma\bar{\sigma}}(\omega)$ is unambiguously expressed in terms of $R_{\mathbf{gf}}^{\sigma\bar{\sigma}}(\omega)$, thereby ensuring true values of correlators in limiting cases.

The following fact is of fundamental importance. The singular (at $\omega = 0$) component of the total spectral intensity cannot be determined only from the knowledge of the Fourier transform of the anomalous Green's function, which is analytically continued to the upper complex half-plane. This fact, in essence, is one further example that illustrates the well-known problem of ambiguously reconstructing the spectral intensity of the correlation function according to the spectral theorem. A discussion of particularly relevant examples can be found, e.g., in the review by Rudoĭ, which has entered into the collection of papers [7], as well as in original papers [8, 9]. Practically, the allowance for singular (at $\omega = 0$) components turns out to be necessary in order to obtain true limiting correlator values.

The analysis performed shows that the origin of above-mentioned forbidding for the existence of the superconducting phase with *S*-type symmetry of the order parameter is exclusively caused by the loss of the singular (at $\omega = 0$) component of the correlation function but not by a principle having a certain actual physical content. Consequently, introducing a singular addition overcomes the indicated forbidding without changing the forms of all previously derived equations in the theory of the superconducting state for strongly correlated systems.

Aimed at confirming the statement on the invariability of the self-consistent equations, we note that representation (2) leads to the following expression for simultaneous correlators:

$$\langle X_{\mathbf{f}}^{0\sigma} X_{\mathbf{g}}^{0\bar{\sigma}}\rangle = S_{\mathbf{gf}}^{\sigma\bar{\sigma}} - \delta_{\mathbf{fg}} S_{\mathbf{gf}}^{\sigma\bar{\sigma}} = \frac{1}{N}\sum_{\mathbf{q}} \exp\{i\mathbf{q}(\mathbf{f}-\mathbf{g})\}\left\{S_{\mathbf{q}}^{\bar{\sigma}\sigma} - \frac{1}{N}\sum_{\mathbf{k}} S_{\mathbf{k}}^{\bar{\sigma}\sigma}\right\}. \quad (15)$$

This implies that in the quasi-momentum representation, we have

$$\langle X_{\mathbf{q}\sigma} X_{-\mathbf{q}\bar{\sigma}}\rangle = \sum_{(\mathbf{f}-\mathbf{g})} \exp\{-i\mathbf{q}(\mathbf{f}-\mathbf{g})\}\langle X_{\mathbf{f}}^{0\sigma} X_{\mathbf{g}}^{0\bar{\sigma}}\rangle = S_{\mathbf{q}}^{\bar{\sigma}\sigma} - \frac{1}{N}\sum_{\mathbf{k}} S_{\mathbf{k}}^{\bar{\sigma}\sigma}.$$

Hence, it follows that the equation

$$\Delta_{\mathbf{k}} = \frac{1}{N}\sum_{\mathbf{q}}\left\{2t_{\mathbf{q}} + \frac{n}{2}(J_{\mathbf{k}+\mathbf{q}} + J_{\mathbf{k}-\mathbf{q}}) + 4\left(1-\frac{n}{2}\right)\frac{t_{\mathbf{k}}t_{\mathbf{q}}}{U} - n\left(\frac{t_{\mathbf{q}}^2}{U} - \frac{J_0}{2}\right)\right\}\langle X_{\mathbf{q}\sigma} X_{-\mathbf{q}\bar{\sigma}}\rangle \quad (16)$$

for the superconducting order parameter $t - J^*$ of the model (with due regard to three-center interactions) [10, 11] does not vary with allowance for the singular component of the spectral intensity of the correlation function because

$$\frac{1}{N}\sum_{\mathbf{q}}\left\{\left[2t_{\mathbf{q}} + \frac{n}{2}(J_{\mathbf{k}+\mathbf{q}} + J_{\mathbf{k}-\mathbf{q}}) + 4\left(1-\frac{n}{2}\right)\frac{t_{\mathbf{k}}t_{\mathbf{q}}}{U} - n\left(\frac{t_{\mathbf{q}}^2}{U} - \frac{J_0}{2}\right)\right]\left[\frac{1}{N}\sum_{\mathbf{p}} S_{\mathbf{p}}^{\bar{\sigma}\sigma}\right]\right\} \equiv 0.$$

ACKNOWLEDGMENTS

We are grateful to Prof. V.A. Ignatchenko for fruitful discussion of this study and valuable comments.

This work was supported by the Quantum Macrophysics Program of the Presidium of Russian Academy of Sciences; by the Russian Foundation for Basic Research, project no. 03-02-16124; by the Russian Foundation for Basic Research together with the "Eniseĭ" Krasnoyarsk Competition Science Foundation, project no. 02-02-97705; and by the Lavrent'ev Competition of projects of young scientists in Siberian Division, Russian Academy of Sciences.

One of us (D. M. D) is indebted for the financial support to the Charitable Foundation of Assistance for Native Science.

REFERENCES

1. R. O. Zaĭtsev, Zh. Éksp. Teor. Fiz. **70**, 1100 (1976) [Sov. Phys. JETP **43**, 574 (1976)].
2. R. O. Zaĭtsev and V. A. Ivanov, Pis'ma Zh. Éksp. Teor. Fiz. **46**, 140 (1987) [JETP Lett. **46**, S116 (1987)].
3. N. N. Plakida, V. Yu. Yushankhay, and I. V. Stasyuk, Physica C (Amsterdam) **162**, 787 (1989).
4. J. C. Hubbard, Proc. R. Soc. London, Ser. A **276**, 238 (1963).
5. D. N. Zubarev, *Nonequilibrium Statistical Thermodynamics* (Nauka, Moscow, 1971).
6. J. C. Hubbard, Proc. R. Soc. London, Ser. A **285**, 542 (1965).
7. *Statistical Physics and Quantum Field Theory*, Ed. by N. N. Bogolyubov (Nauka, Moscow, 1973).
8. H. Callen, R. H. Swendsen, and R. Tahir-Kheli, Phys. Lett. A **25**, 505 (1967).
9. P. E. Bloomfield and N. Nafari, Phys. Rev. A: Gen. Phys. **5**, 806 (1972).
10. V. Yu. Yushankhay, G. M. Vujicic, and R. B. Zakula, Phys. Lett. A **151**, 254 (1990).
11. V. V. Val'kov, T. A. Val'kova, D. M. Dzebisashvili, and S. G. Ovchinnikov, Pis'ma Zh. Éksp. Teor. Fiz. **75**, 450 (2002) [JETP Lett. **75**, 378 (2002)].

Translated by G. Merzon

Doklady Physics, Vol. 48, No. 11, 2003, pp. 612–614. Translated from Doklady Akademii Nauk, Vol. 393, No. 2, 2003, pp. 180–183.

PHYSICS

Stepwise Transition from Elastic to Elastoplastic Deformation at the Initial Stage of Nanoindentation

Yu. I. Golovin* and S. N. Dub**

Presented by Academician Yu.A. Osipov April 28, 2003

Received April 29, 2003

Strong deviation from the Hooke's law (conditional yield limit σ_y) in macrotests for tension/compression, torsion, bending, etc., is usually attributed to the mass nucleation and further motion of dislocations. In certain rare cases (e.g., in single crystals of silicon and other semiconductors in the absence of stress concentrators), this process is hindered. In these cases, the overstress region, or yield tooth, appears on the σ–ε loading diagram (Fig. 1) detected by an Instron hard testing machine at the initial loading stages. In contrast to the deformation of macrospecimens, the transition from elastic local deformation to elastoplastic deformation during nanoindentation tests is usually stepwise [1–7]. Since all available nanoindentometers are soft testing machines (i.e., they specify force *P*, while hard testing machines specify strain Δl), the strain jump in them is equivalent to the dip of the stress in a hard machine near the yield tooth. The volume of the locally deformed region at the initial indentation stages is very small (1–100 nm^3). This substantial circumstance can strongly change the physicochemical properties of the material and deformation mechanisms [8–11].

In this work, the features of the elastoplastic transition are studied under the local deformation of nanoregions of the material by ultralow loadings (*P* varies from 0.1 μN to 1 mN). It is shown that even very plastic crystals (KCl, NaCl, etc.) are elastically deformed up to contact stress magnitudes on the order of the theoretical ultimate stress. The nucleation of dislocation loops is hindered at the initial indentation stage because the local deformed region is too small to contain dislocation-loop nuclei of supercritical sizes.

The experimental data were obtained by an MTS Nanoindenter II. Figure 2 shows the typical *P*–*h* diagrams, where *P* is the indentation force and *h* is the depth. As a rule, jumps were observed on the surfaces of spall or growth, which were not mechanically processed or were chemically etched after polishing.

It is generally clear that certain elastic deformation precedes any plastic deformation. A triangular diamond Berkovich pyramid is ordinarily used for nanoindentation. However, an actual indenter always has a certain vertex dulling, which can be taken into account by introducing the equivalent curvature radius *R*. We used an indenter with $R = 220$ nm, which was determined by several independent methods. For $h \ll R$, indentation of the indenter in the material can be considered in the model of the elastic interaction of a ball with a half-

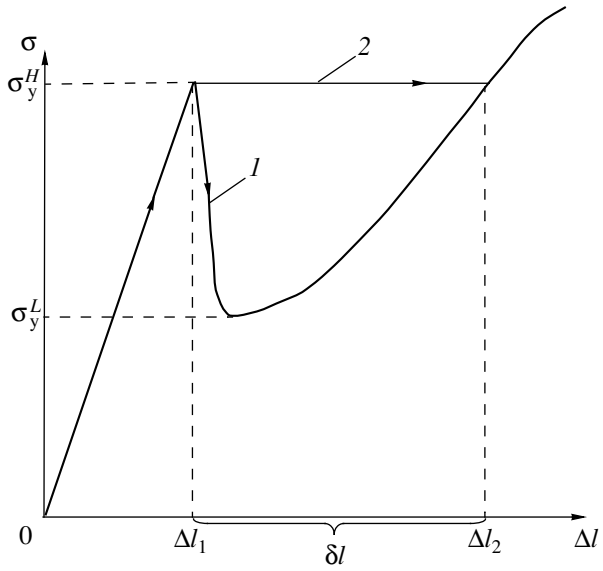

Fig. 1. Plots of the formation of jumps in (*1*) stress σ in a hard testing machine and (*2*) strain Δl in a soft testing machine in the transition from elastic to elastoplastic deformation near the yield point; σ_y^H and σ_y^L are the upper and lower yield points, respectively, and $\delta l = \Delta l_2 - \Delta l_1$ is the strain jump in the soft machine.

* *Tambov State University, ul. Internatsional'naya 33, Tambov, 392622 Russia e-mail: golovin@tsu.tmb.ru*

** *Bakul Institute for Superhard Materials, National Academy of Sciences of Ukraine, ul. Avtozavodskaya 2, Kiev, 04074 Ukraine e-mail: sergey_dub@ukrpost.net*

1028-3358/03/4811-0612$24.00 © 2003 MAIK "Nauka/Interperiodica"

space. According to the Hertz contact theory, for this model,

$$P = \frac{4}{3}E^*\sqrt{Rh^3},$$

where

$$E^* = \left(\frac{1-\nu_m}{E_m} - \frac{1-\nu_i}{E_i}\right)^{-1}$$

is the reduced elastic modulus. Here, E_m and ν_m are, respectively, the elastic modulus and Poisson's ratio of the material and E_i and ν_i are respective quantities for the indenter.

According to Fig. 2, *P*–*h* dependences at the initial deformation stage (until the first jump in *h*) coincide with the Hertz law $P \sim h^{3/2}$. Unloading at this stage leads to the complete elastic recovery of the impression without any traces of plastic deformation, which is corroborated by atomic force microscopy and by the absence of hysteresis in the *P*(*h*) curve (Fig. 2b). When the critical force P_{cr} corresponding to h_{cr} from 5 to 65 nm in various materials is reached, the strain undergoes a jump. Then, the slope of the *P*(*h*) curve returns to the Hertz behavior in certain materials and decreases strongly in other materials. A substantial difference from macrotests is that strain jumps at the yield limit are observed not only in hard materials (cBN, W, Mo) but also in many others including soft ionic crystals and fcc metals (Cu, Al, Au, etc.) [1–4]. This fact implies that a cause of this behavior is common.

The nucleation and motion of dislocations are the most probable causes for the formation of jumps. We consider in detail the conditions of the nucleation of dislocation loops under the indenter at the initial indentation stage. In various planes where dislocation loops can nucleate under the indenter, shear stresses act. Their maximum is equal to

$$\tau_{max} = 0.31 p_{max},$$

where

$$p_{max} = \left(\frac{6E^{*2}P}{\pi^3 R^2}\right)^{1/3}$$

is the maximum contact pressure in the impression. We note that the Meier hardness is equal to $H = \frac{2}{3}p_{max}$. We emphasize that maximum shear stresses are reached at the point spaced by 0.48 of the contact region radius

$$a = \frac{\pi R}{2E^*}\left(\frac{6E^{*2}P}{\pi^3 R^2}\right)^{1/3}$$

rather than at the center of the impression or at any other point on its surface.

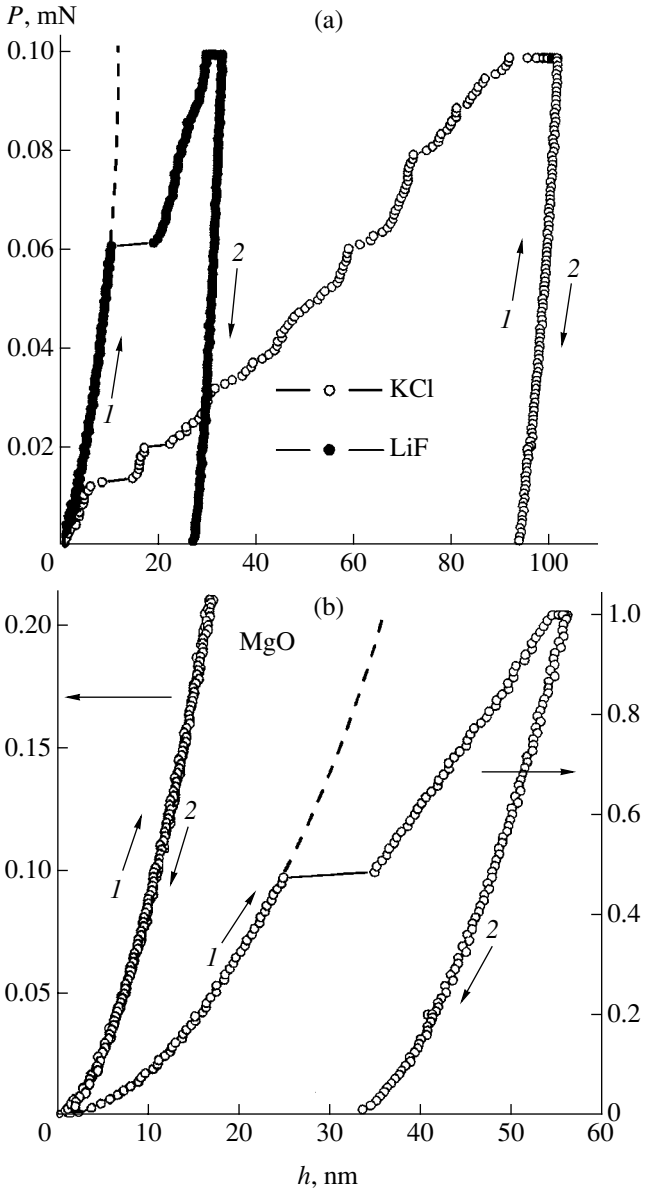

Fig. 2. Typical stress–strain curves at the initial stages of nanoindentation: (*1*) loading stage and (*2*) unloading stage; the dashed line is the Hertz law $P \sim h^{3/2}$.

As is known [12], for a dislocation loop with radius *r* to nucleate in the uniform stress field τ, it is necessary to have the excess free energy

$$\Delta U_d = \frac{2-\nu}{1-\nu}\frac{Gb^2}{4}r\left[\ln\left(\frac{4r}{r_0}\right) - 2\right],$$

where *G* is the shear modulus, *b* is the Burgers vector, and $r_0 \simeq b$. In this case, the elastic energy $\Delta U_e = \pi r^2 b\tau$ is released. For $r \sim 10b$, $\Delta U_d \approx Gb^2 r$. Homogeneous nucleation of a dislocation loop nucleus is possible for $U_g \geq U_c$; i.e., the condition $\tau \geq \frac{Gb}{r_{cr}}$ is one (force) of the

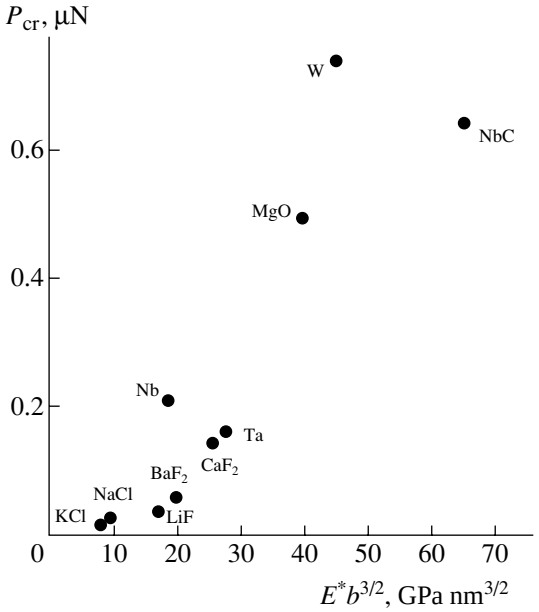

Fig. 3. Critical force P_{cr} before the strain jump vs. the fundamental parameter $E^*b^{3/2}$.

necessary conditions of the flow onset. Therefore,

$$r_{cr} \geq \frac{Gb}{0.31}\left(\frac{\pi^3 R^2}{6E^{*2}P}\right)^{1/3}. \quad (1)$$

At the same time, the "geometric" condition must be satisfied in the field of strongly nonuniform stresses: the size r' of the region, where stresses are strong enough for a stress loop to nucleate, must be no less than the critical loop radius r_{cr}. Taking $r' = Ka$ (where $K \approx 1$), we obtain

$$r_{cr} = \frac{K\pi R}{2E^*}\left(\frac{6E^{*2}}{\pi^3 R^2}P\right)^{1/3}. \quad (2)$$

Equating expressions (1) and (2), we determine the critical value

$$P_{cr} = \left(\frac{2E^{*2}b}{K\pi R}\right)^{3/2}\frac{\pi^3 R^2}{6E^{*2}} = 2.56E^*\left(\frac{b}{K}\right)^{3/2}R^{1/2}. \quad (3)$$

Figure 3 shows the P_{cr} values measured as a function of the parameter $E^*b^{3/2}$ for a number of materials being investigated. It is seen that the results qualitatively agree with expression (3), i.e., with the model of the homogeneous nucleation of dislocations in nanovolumes.

The Δh jump value provides the reasonable estimate $N \approx \frac{\Delta h}{b} \approx$10–50 for the number of formed loops. It is obvious that stress concentrators that can reduce P_{cr} always exist in an actual crystal whose imperfectly planar surface is indented by an imperfect sphere. However, for a nanometer loading region, the probability of the existence of such concentrator is low, which is corroborated, first, by the qualitative agreement of the results with the model of homogeneous nucleation and, second, by the fact that extremely fine mechanical polishing eliminates jumps and smoothens the deformation curve. Small irreversible deformations observed in certain materials before the appearance of the first jump can be attributed to the manifestation of nondislocation modes of plasticity (e.g., due to the formation of interstitial atoms and crowdions [10, 11, 13, 14]).

Thus, the initial stage of nanoindentation is purely elastic even in plastic materials. As a result, contact stresses before the stepwise transition to plastic flow reach $\tau_{max} \approx 0.05$–$0.1G$, which is comparable with the theoretical ultimate stress. Since many current elements of nanotechnological devices operate under the conditions of dynamic nanocontact interaction (i.e., probes of scanning atomic force microscopes), it is necessary to take into account the possibility of a considerable increase in the load carrying capability of the material under these conditions.

ACKNOWLEDGMENTS

This work was supported by the Russian Foundation for Basic Research (project no. 01-02-16573) and the Ministry of Education of the Russian Federation (project no. E02-34-263).

REFERENCES

1. D. F. Bahr, D. E. Kramer, and W. W. Gerberich, Acta Mater. **46**, 3605 (1998).
2. D. F. Bahr, D. E. Wilson, and D. A. Growson, J. Mater. Res. **14**, 2269 (1999).
3. W. W. Gerberich, D. E. Kramer, N. I. Tymiak, *et al.*, Acta Mater. **47**, 4115 (1999).
4. A. Gouldstone, H.-J. Koh, K.-Y. Zeng, *et al.*, Acta Mater. **48**, 2277 (2000).
5. D. F. Bahr, C. M. Watkins, D. E. Kramer, and W. W. Gerberich, Mater. Res. Soc. Symp. Proc. **552** (10), 83 (1998).
6. H. S. Leipner, D. Lorenz, A. Zecker, *et al.*, Physica B (Amsterdam) **308**–**310**, 446 (2001).
7. S. Suresh, T.-G. Nieh, and B. W. Choi, Scr. Mater. **41**, 951 (1999).
8. B. Bhushan, J. N. Israelachvili, and U. Landman, Nature (London) **374**, 607 (1995).
9. H. Gleiter, Acta Mater. **48**, 1 (2000).
10. Yu. I. Golovin, A. I. Tyurin, and B. Ya. Farber, J. Mater. Sci. **37**, 895 (2002).
11. Yu. I. Golovin, A. I. Tyurin, and B. Ya. Farber, Philos. Mag. A **82**, 1857 (2002).
12. J. P. Hirth and J. Lothe, *Theory of Dislocations* (McGraw-Hill, New York, 1968; Atomizdat, Moscow, 1972).
13. B. Ya. Farber, V. I. Orlov, and A. H. Heuer, Phys. Status Solidi A **166**, 115 (1998).
14. M. A. Velednitskaya, V. N. Rozhauskiĭ, L. F. Comolova, *et al.*, Phys. Status Solidi A **32**, 123 (1975).

Translated by R. Tyapaev

Doklady Physics, Vol. 48, No. 11, 2003, pp. 615–618. Translated from Doklady Akademii Nauk, Vol. 393, No. 2, 2003, pp. 184–187.

PHYSICS

Distribution Functions in Scale Transformations of 1/*f* Fluctuations

Corresponding Member of the RAS V. P. Koverda and V. N. Skokov

Received June 18, 2003

Fluctuation power spectra (flicker noise spectra) $S \sim 1/f$, varying in inverse proportion to the frequency f, are specific for various physical, chemical, mechanical, and biological systems [1, 2]. The $1/f$ dependence remains valid over a wide range (several orders of magnitude of the fluctuation power). In astrophysical observations, $1/f$ pulsations of the radiation intensity of quasars and sunspots are well known. In geophysics, $1/f$ spectra are used for describing earthquakes and floods. Spectra of $1/f$ are also observed in variations of the insulin content in the blood of diabetics and in cardiac and muscular rhythms specific for certain illnesses. Financial variations and rates of exchange also obey the $1/f$ spectral dependence. Moreover, flicker fluctuations are manifested in the number of cars on the roads and even in music and speech [3].

In the literature, stochastic processes with spectra of the $1/f^{\alpha}$ form, where the exponent α can vary within a certain range, are sometimes considered as $1/f$ noise. A spectrum varying exactly in inverse proportion to the frequency ($\alpha = 1$) is observed for voltage fluctuations formed by an electric current flowing in resistors [2, 4] and in the case of nonequilibrium phase transitions, e.g., in boiling crisis regimes, under explosive boiling of superheated-liquid jets, in vibratory regimes of combustion, and in arc discharge [5–10].

The dynamical scaling, which is observed at critical points of equilibrium, is a well-known feature of $1/f$ fluctuations. There have been numerous attempts to elucidate the mechanism of generation of scale-invariant fluctuations. The concept of self-organized criticality is a striking example [11]. It is evident that not all systems exhibiting $1/f$ fluctuations are acceptable for analysis in terms of this scheme. Moreover, in the models of the self-organized criticality, the fluctuation spectrum has the form $1/f^{\alpha}$ (with $\alpha > 1$), and the fluctuation distributions are not Gaussian [12, 13].

Institute of Thermal Physics, Ural Division, Russian Academy of Sciences, ul. Amundsena 106, Yekaterinburg, 620016 Russia
e-mail: vnskokov@itp.uran.ru

In this paper, we present numerical results for the distribution functions under scale transformations of $1/f$ fluctuations in nonequilibrium phase transitions. According to theory of $1/f$- fluctuations under nonequilibrium phase transitions, which was proposed in [5], the spectral density of the fluctuation power is strictly proportional to $1/f$, and the corresponding distribution function is Gaussian.

The simplest stochastic equations describing fluctuations in a concentrated system have the form

$$\begin{aligned} \frac{d\phi}{dt} &= -\phi\psi^2 + \psi + \Gamma_1(t), \\ \frac{d\psi}{dt} &= -\phi^2\psi + 2\phi + \Gamma_2(t). \end{aligned} \tag{1}$$

Here, ϕ and ψ are dynamical variables, and $\Gamma_1(t)$ and $\Gamma_2(t)$ are Gaussian δ-correlated noises with the same variances. Because of the multiplier 2 in the second equation, the equations of system (1) are nonequivalent. System (1) experiences a noise-induced transition with respect to the probability density $P(\sqrt{\phi^2\psi^2})$. If the white-noise intensity corresponds to the criticality condition for the noise-induced transition, then the solutions $\phi(t)$ and $\psi(t)$ of system (1) represent stationary stochastic processes with the power spectra of the forms $1/f$ and $1/f^2$, respectively.

When integrating system (1) numerically, it is rewritten in the form [5, 14]

$$\begin{aligned} \phi_{i+1} &= (\phi_i + \psi_i\Delta t)(1 + \psi_i^2\Delta t)^{-1} + \xi_i\Delta t^{0.5}, \\ \psi_{i+1} &= (\psi_i + 2\phi_i\Delta t)(1 + \phi_i^2\Delta t)^{-1} + \eta_i\Delta t^{0.5}, \end{aligned} \tag{2}$$

where ξ_i and η_i are sequences of Gaussian random numbers with zero means and standard deviations σ. If the integration step is chosen within the interval $0.05 < \Delta t < 0.3$, the criticality condition for the noise-induced transition has the form $\sigma_c = 0.8$. Therefore, under the condition $0.7 < \sigma < 0.9$, the fluctuation power spectra for ϕ_i and ψ_i correspond to the dependences $1/f$ and $1/f^2$, respectively. In our calculations, we took integra-

1028-3358/03/4811-0615$24.00

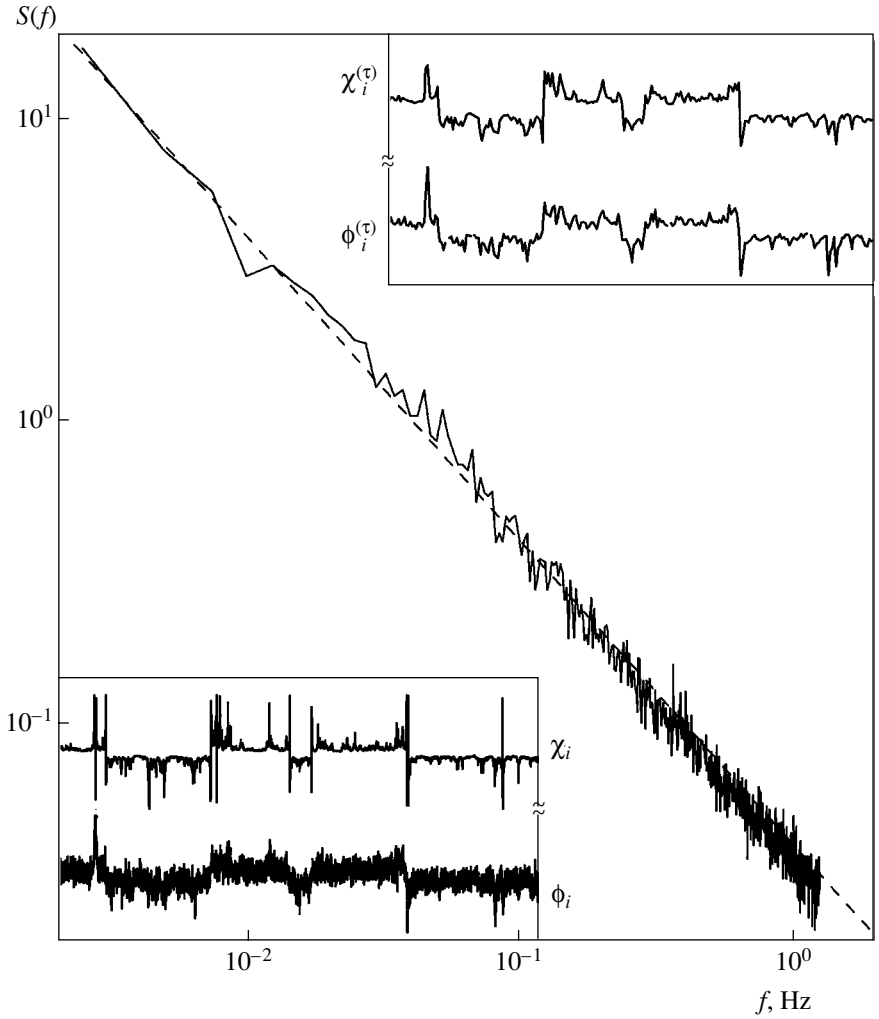

Fig. 1. Fluctuation power spectra for the processes ϕ_i and χ_i. Dashed line represents the ~1/*f* dependence. Initial (ϕ_i and χ_i) and roughened ($\phi_i^{(\tau)}$ and $\chi_i^{(\tau)}$ for $\tau = 32$) realizations are shown in the upper and lower inserts, respectively.

tion steps of 10^4 to 10^5 and performed averaging over several tens of realizations.

Each calculated realization of a random process was characterized by both the mean value and variance. For zero initial conditions ($\phi_0 = 0$ and $\psi_0 = 0$), the random processes attained the steady-state regime in a certain time. This transient period can be estimated by comparing the above case with the realization of a stochastic process for the same sample of random numbers but under initial conditions corresponding to the mean values $\phi_0 = \sqrt{\overline{\phi^2}}$ and $\psi_0 = \sqrt{\overline{\psi^2}}$. For the parameters taken within the above-indicated range, the transient period did not exceed 5% of the sample volume. The initial conditions corresponding to the standard deviation, which result in a decrease in the transient period, allow us to reduce the integration step and, thereby, to retain the 1/*f* dependence of the fluctuation power spectrum.

The system of equations (2) remains applicable not only in the vicinity of the critical point of the noise-induced transition but within a fairly wide range of the distribution parameters. This property follows from the self-consistency of the variables ϕ_i and ψ_i of system (1). As was pointed out in [5], the approximate equality $\overline{\phi_i\psi_i} \approx 1$ for the mean product remains valid for a concentrated system regardless of the sampling volume and other relevant parameters. Because of this, we consider a new function $\chi_i = \dfrac{\psi_i}{\varepsilon + \psi_i^2}$, which for small ε is close to the function $1/\psi_i$. Introducing the parameter ε eliminates the divergence of the function χ_i at zeros of the function ψ_i. This divergence of the function $1/\psi_i$ can be removed by various methods but the basic result is unaffected: the spectral density of χ_i is inversely proportional to the frequency $S_\chi \sim 1/f$, and coincides numerically with that of the function ϕ_i. The identical

spectral densities of the variables ϕ_i and χ_i are shown in Fig. 1. The parameter ε was chosen within the range 0.01 to 0.02. Even though the power spectrum of ψ_i is inversely proportional to the frequency squared, i.e., $S_\psi \sim 1/f^2$, the power spectrum of the variable χ_i is proportional to $1/f$. Thus, the second equation of system (1) or (2) after the change of the variable $\psi(t)$ by $\chi(t)$, as well as the first equation, results in the $1/f$ spectrum.

The distribution functions for the variables ϕ_i and χ_i are different. The distribution function for the variable ϕ_i is shown in Fig. 2. This function is close to the Gaussian distribution but has a long tail of large fluctuations especially well pronounced in semilogarithmic coordinates. As follows from numerical calculations, the distribution function can be approximated by the expression

$$P(\phi) = A\exp\left(-\frac{\phi^2}{2\sigma_\phi}\right) + B\exp\left(-\frac{|\phi|}{\sigma_\phi}\right), \qquad (3)$$

where A and B are constant and $\sigma_\phi = 2\sigma t^{0.5}$ is the standard deviation of the random process $\phi(t)$. In contrast to $P(\chi)$, the distribution function $P(\phi)$ has a minimum at the zero value of the argument (Fig. 2).

We now analyze changes of the distribution functions under a scale transformation of the realizations. For this purpose, we introduce a sequence of roughened realizations $\{y^{(\tau)}\}$ formed by averaging the initial realization $\{x_1, x_2, \ldots, x_N\}$ over a certain time scale τ referred to as a scale-transformation coefficient (scaling factor) according to the equation

$$y_j^{(\tau)} = \frac{1}{\tau}\sum_{i=\tau j}^{\tau(jN)-1} x_i, \quad 0 \le j \le \frac{N}{\tau}. \qquad (4)$$

Here, x_i is a stochastic variable (ϕ_i, χ_i, etc.). The first realization $\{y^{(1)}\}$ coincides with the initial one. The volume of each subsequent roughened realization decreases by a factor of τ, i.e., consists of $\frac{N}{\tau}$ numbers. It is worth noting that the given scale transformation does not affect the spectrum. The spectra of $\phi_i^{(\tau)}$ and $\chi_i^{(\tau)}$ vary in inverse proportion to the frequency: $S \sim 1/f$. In order to numerically characterize distribution changes caused by the scale transformation, we define the quantity

$$H(x) = -\sum_{x_i} p(x_i)\log p(x_i), \qquad (5)$$

which has a sense of informational entropy. In [14], this method was referred to as a multiscaling entropic analysis of realizations. We now consider the entropy $H(x)$ as a function of the scaling factor τ. The calculated entropy of roughened realizations and that of white noise are shown in Fig. 3 as functions of the scaling factor τ. As is seen from Fig. 3, in contrast to the Gaussian δ-correlated process (white noise) whose entropy

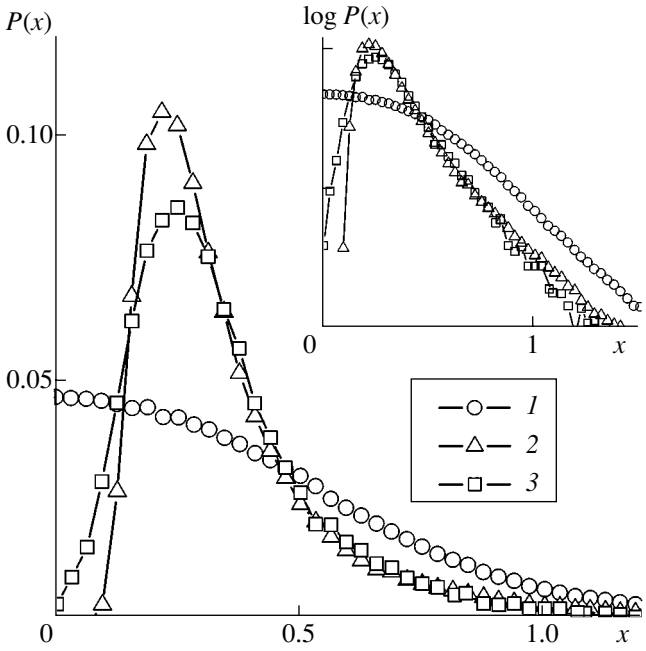

Fig. 2. Distribution functions for the stochastic variables: (*1*) $P(\phi_i)$; (2) $P(\chi_i)$; and (*3*) $P(\phi_i^{(\tau)}) = P(\chi_i^{(\tau)})$ with $\tau = 32$. The same functions are shown in the insert in semilogarithmic coordinates.

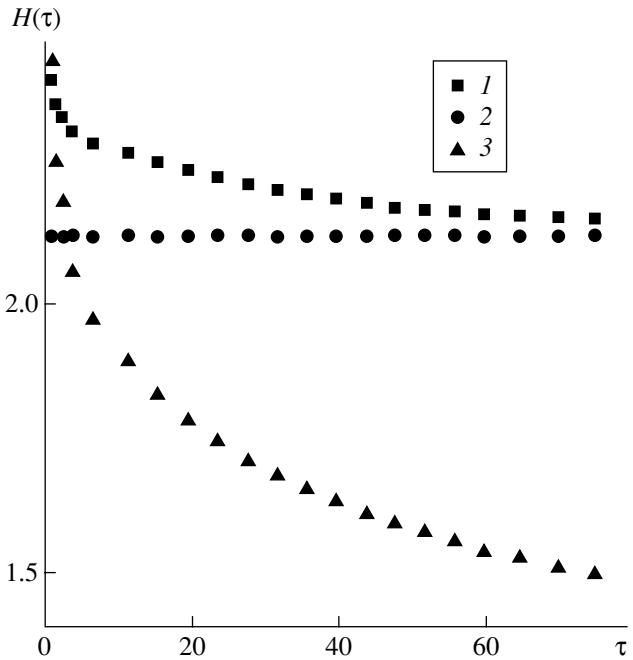

Fig. 3. Entropy of the random processes as functions of the scaling factor τ (*1*) $\phi_i^{(\tau)}$, (*2*) $\chi_i^{(\tau)}$, and (*3*) white noise.

decreases with increasing the scaling factor, the entropy of the random process $\chi_i^{(\tau)}$ does not vary. This indicates the self-similarity of the latter process. The entropy of the random process $\phi_i^{(\tau)}$ decreases (but much slower than that of the white noise) and tends to the constant entropy H of the process $\chi_i^{(\tau)}$.

The realizations of roughened random processes $\phi_i^{(\tau)}$ and $\chi_i^{(\tau)}$ for $\tau = 32$ are shown in the upper insert in Fig. 1. They evidently differ slightly. The Pearson correlation coefficient for $\tau = 32$ is equal to 0.9. With a further increase in the scaling factor, the difference of the realizations tends to zero.

In the case of $\tau = 32$, the distribution functions for $\phi_i^{(\tau)}$ and $\chi_i^{(\tau)}$ practically coincide and are approximated by the formula

$$P(\chi) = C\chi^2 \exp\left(-\frac{|\chi|}{\sigma_\chi}\right). \quad (6)$$

The exponential factor in (6) describes long-wave fluctuations of the random process with the 1/*f* power spectrum. This is consistent with the results of [15], namely, the scaling function for the roughened distribution of certain periodic signals with the 1/*f* spectrum is a distribution of extreme fluctuations. Our results testify to the fact that under the scaling transformation, the Gaussian distribution of a stochastic process with the 1/*f* spectrum also turns into the exponential distribution.

ACKNOWLEDGMENTS

This work was supported by the Russian Foundation for Basic Research, project no. 03-02-16215 and by the Program for Basic Research of Russian Academy of Sciences.

REFERENCES

1. Sh. M. Kogan, Usp. Fiz. Nauk **145**, 285 (1985) [Sov. Phys. Usp. **28**, 170 (1985)].
2. M. B. Weissman, Rev. Mod. Phys. **60**, 537 (1988).
3. Yu. L. Klimontovich, *Statistical Theory of Open Systems* (Yanus, Moscow, 1995; Kluwer, Dordrecht, 1995).
4. A. V. Yakimov and F. N. Hooge, Physica B (Amsterdam) **291** (1–2), 97 (2000).
5. V. P. Koverda, V. N. Skokov, and V. P. Skripov, Zh. Éksp. Teor. Fiz. **113**, 1748 (1998) [JETP **86**, 953 (1998)].
6. V. N. Skokov, V. P. Koverda, and A. V. Reshetnikov, Pis'ma Zh. Éksp. Teor. Fiz. **69**, 590 (1999) [JETP Lett. **69**, 636 (1999)].
7. V. N. Skokov, A. V. Reshetnikov, and V. P. Koverda, Teplofiz. Vys. Temp. **38**, 786 (2000).
8. A. V. Reshetnikov, A. V. Vinogradov, V. P. Koverda, and V. N. Skokov, Dokl. Ross. Akad. Nauk **374**, 481 (2000) [Dokl. Phys. **45**, 515 (2000)].
9. V. N. Skokov, V. P. Koverda, and A. V. Reshetnikov, Zh. Éksp. Teor. Fiz. **119**, 613 (2001) [JETP **92**, 535 (2001)].
10. V. N. Skokov, A. V. Koverda, A. V. Reshetnikov, *et al.*, Int. J. Heat Mass Transf. **46**, 1879 (2003).
11. P. Bak, C. Tang, and K. Wiesenfeld, Phys. Rev. A: Gen. Phys. **38**, 364 (1988).
12. H. J. Jensen, *Self-Organized Criticality* (Cambridge Univ. Press, Cambridge, 1998).
13. H. J. Jensen, K. Christinsen, and H. C. Fogetby, Phys. Rev. B: Condens. Matter **40**, 7425 (1989).
14. M. Costa, A. L. Goldberger, and C.-P. Peng, Phys. Rev. Lett. **89**, 068102-1 (2002).
15. T. Antal, M. Droz, G. Gyorgyi, and Z. Racz, Phys. Rev. Lett. **87**, 240601-1 (2001).

Translated by V. Chechin

Doklady Physics, Vol. 48, No. 11, 2003, pp. 619–621. Translated from Doklady Akademii Nauk, Vol. 393, No. 2, 2003, pp. 188–190.

PHYSICS

Traveling Pulse of an Exothermic Reaction

E. N. Rumanov

Presented by Academician A.G. Merzhanov June 25, 2003

Received July 1, 2003

Traveling pulses are one of the basic varieties of autowaves [1–3]. Complex regimes (rotating spirals, circular waves diverging from a leading center, etc.) can be constructed from these pulses. In the present paper, a regime is analyzed. This regime differs from a combustion wave in the fact that the initial content of a mixture is recovered beyond the reaction zone due to transverse (with respect to the wave propagation direction) flow through the system. The temperature and concentration profiles make it possible to isolate four zones in the pulse structure, namely, the heating zone, reaction zone, cooling zone, and recovery zone. An estimate for the parameters of these zones is given. A limit for the pulse propagation is determined. At high Damcöler numbers, the magnitude of this limit tends to the combustion limit.

1. A system composed of two diffusion equations with nonlinear sources is often used as the mathematical model of a pulse. The source intensity increases with the concentration of one of the components (i.e., the activator) and decreases with the concentration of the other component (i.e., the inhibitor). In the case of an exothermic reaction, heat plays the role of the activator. The exponential dependence of the reaction rate on temperature results in the appearance of a certain large parameter, namely, the Zel'dovich number

$$Z = E\frac{T_b - T_0}{T_b^2}. \quad (1)$$

Here, E is the activation energy;

$$T_b = T_0 + \frac{Q}{c}, \quad (2)$$

T_0 is the thermostat temperature; Q is the reaction heat; and c is the specific heat. Thus, we may apply the asymptotic method developed for the first time in [4]. The considered effects exhibited here contrast greatly when compared to autowaves produced by power nonlinearity. At the same time, in the qualitative sense these phenomena are intrinsic to waves generated by power sources.

We write out the set of relevant equations in the form;

$$\frac{\partial\eta}{\partial t} - L\frac{\partial^2\eta}{\partial x^2} = \Phi(\eta, \theta) - \frac{\eta}{D}, \quad (3)$$

$$\frac{\partial\theta}{\partial t} - \frac{\partial^2\theta}{\partial x^2} = Z\Phi - \frac{\theta + Z}{S}, \quad (4)$$

$$\Phi = (1-\eta)\exp\frac{\theta}{1 + A\theta}. \quad (5)$$

Here, the reaction time τ_R at a temperature T_b is a scale of time t; the quantity $\sqrt{\chi\tau_R}$; serves as a scale for the coordinate x; χ is the thermal diffusivity; η is the concentration of a reaction product (for definiteness, the first-order reaction is considered); θ is temperature counted off from T_b in the AT_b scale; $A = \frac{T_b}{E}$ is the Arrhenius number; D is the Damcöler number, i.e., the ratio of the flow-through time to τ_R; L is the Lewis number, i.e., the ratio of diffusivity to thermal conductivity; and S is the Semenov number, i.e., the ratio of the heat removal time to τ_R. An object being described by Eqs. (3), (4) can be represented as a chain of small reactors of instantaneous mixing. Adjacent chain elements are linked to one another by both diffusion and heat conduction.

The solutions in the form of solitary waves correspond to the boundary conditions

$$x \to \pm\infty, \quad \frac{\partial\eta}{\partial x} = 0, \quad \frac{\partial\theta}{\partial x} = 0. \quad (6)$$

For a system close to that described by Eqs. (3)–(6), switching waves between high-temperature and low-temperature states have been studied [5]. The switching-wave velocity is low compared to that of combustion waves. In the latter, the reaction reprocesses the substance located in the path of the wave. The higher the reaction rate, the higher the wave velocity. In the case of switching waves, the substance is reprocessed

Institute of Structural Macrokinetics and Materials Science, Russian Academy of Sciences,
Chernogolovka, Moscow oblast, 142432 Russia
e-mail: ed@ism.ac.ru

1028-3358/03/4811-0619$24.00

in the hot reactor zone, which is carried by the transverse flow so that the reaction rate is limited by the flow intensity. The quantity $\frac{1}{\sqrt{S}}$ serves as a wave velocity scale. In the dimensional form, the scale corresponds to the quantity $\sqrt{\frac{\chi}{\tau}}$, where τ is the time of the heat removal into a thermostat. In this case, the condition $\tau \gg \tau_R$ is always valid. If this condition is not fulfilled then the temperature in the reactor is practically equal to T_0, and the reaction being studied can be ignored.

2. In the system under consideration, the traveling pulse is a wave. Both ahead of and behind this wave, the reactor state is low-temperature, and the content of a mixture that flows through these sections is almost invariable. The pulse forepart weakly differs from the combustion wave. In the reaction zone, the substance residing at the given point of the reactor at the moment the pulse passes through it is reprocessed. The transverse flow through the reaction zone can be ignored: the increase brought by this flow is proportional to $\frac{1}{D}$. At the same time, as we will see, the pulse can propagate only in the case of sufficiently large Damcöler numbers. Thus, the pulse velocity is almost independent of D and is close to the combustion rate at given L, S, and Z. Beyond the reaction zone, the temperature is high. All the substance brought by the flow is immediately reprocessed so that the intensity of a thermal source in Eq. (4) is close to $\frac{Z}{D}$. However, this is insufficient to compensate for the heat loss. Indeed, the quantity S cannot exceed D because other channels of the heat removal are possible along with the flow. Therefore, behind the reaction zone, the temperature drops (the cooling zone). At $e^{-\theta} > D$, the reaction does not manage to reprocess the incoming mixture. The quantity η decreases from the value close to unity to almost zero (the recovery zone).

The structure described exists in the case of

$$\frac{S}{D} < 1 - Z^{-1}\left(\frac{\ln D}{1 + A\ln D}\right). \tag{7}$$

In the opposite case, a fast wave switching the regime from low-temperature to high-temperature propagates in the system under consideration. The velocity of this wave is high compared to that found in [5]. The fast wave differs from that described in [5] by a temperature maximum in its forepart, which ensures a high velocity. The condition of the passage from the slow inflammation wave to the fast one, which is accompanied by a velocity jump, is obtained in [6]. The second term in condition (7) is only a correction. When this correction is not small, the difference between the high-temperature state and low-temperature state of the reactor and between the cooling zone and the recovery zone degenerates.

The heating zone and the reaction zone have widths on the order of that of a combustion wave. For estimating the width of both the cooling zone and the recovery zone, we make use of an approximation proposed in [4]. The reaction zone is considered to be a surface at which a heat flux jump Zu occurs, while the pulse velocity is determined by the condition

$$u^2 = u_0^2 e^{\theta_m}. \tag{8}$$

Here, u_0 is the combustion wave velocity as $S \to \infty$, and θ_m is the temperature in the reaction zone. We now assume that at the boundary between the cooling and recovery zones,

$$\theta = \theta_1, \quad \exp\frac{\theta_1}{1 + A\theta_1} \sim \frac{1}{D}, \tag{9}$$

and in the recovery zone, the quantity Φ can be ignored, whereas in the cooling zone, $\Phi \approx \frac{1}{D}$. Evidently, the widths of the heating and recovery zones are $\sim\frac{1}{u}$ and $\sim Du$ (excluding the unreal case of $L \gg Du^2$), respectively. In the coordinate system moving at a velocity u, we place the reaction zone at the point $x = 0$, while at the boundary between the cooling and recovery zones, $x = x_1$. In this case, we have at the point $x = 0$,

$$Z + \theta_m = \frac{SZ}{D} + C_+ + C_-, \tag{10}$$

$$k_+(Z + \theta_m) - k_+C_+ - k_-C_- = Zu,$$

$$k_\pm = \frac{u}{2} \pm \sqrt{\frac{u^2}{4} + \frac{1}{S}}. \tag{11}$$

At the same time, we have at the point $x = x_1$,

$$\frac{SZ}{D} + C_+e^{k_+x_1} + C_-e^{k_-x_1} = Z + \theta_1, \tag{12}$$

$$k_+C_+e^{k_+x_1} + k_-C_-e^{k_-x_1} = k_-(Z + \theta_1). \tag{13}$$

Equations (8)–(13) allow us to find six quantities, namely, u, θ_m, x_1, θ_1, C_+, and C_-. Excluding C_+, and $C_+e^{k_+x_1}$ from (10)–(13), we find (in the limit $Su^2 \gg 1$) the width of the cooling zone,

$$x_1 \approx Su\ln\frac{1 - \frac{S}{D}}{1 + \frac{\theta_1}{Z} - \frac{S}{D}}. \tag{14}$$

Vanishing the denominator in the right-hand side of expression (14) corresponds to the condition (7): the pulse transforms into a fast inflammation wave, and the recovery zone is absent.

According to conditions (12)–(14), the quantity $|C_+|$ must be exponentially small. Then, it follows from relationships (10), (11) that

$$\theta_m \approx -\frac{Z}{u^2}\left(\frac{2}{S} - \frac{1}{D}\right). \quad (15)$$

As is seen from formulas (8), (15), at $S > S_{th}$, where

$$S_{th} = 2\left[\frac{u_0^2}{Ze} + \frac{1}{D}\right]^{-1}, \quad (16)$$

there are two solutions (the slow wave is unstable). At $D \gg D_0 = Zeu_0^{-2}$, the quantity S_{th} tends to the combustion limit (see [4]). It follows from expressions (7), (16) that traveling pulses can exist at

$$D > D_1 \approx D_0\left[1 + \frac{2}{Z}\ln D_0\right].$$

3. In the coordinate system moving with the combustion wave, the heating zone for this wave can be considered (see [3]) as a plane flow-type reactor. At $L < 1$, the enthalpy excess in the reactor results in relaxation oscillations [7, 8]. In the laboratory coordinate system, the oscillations look like alternating events of deceleration and acceleration of a wave, i.e., a sequence of short flares and long depressions. Pulses traveling over the disk reactor produce a rotating spiral, which corresponds to the spin regime.

Numerically modeling the spin combustion in the three-dimensional setting of the problem (see [9]) makes it possible to compare the data obtained with predictions about traveling pulses in this reactor. The profiles of temperature and concentration in the direction of the moving combustion center, which are calculated in [9], correspond to the four-zone structure. The quantity η rapidly rises up to one near the temperature maximum, and this value is preserved within a segment of a finite length. The temperature at this segment drops. Furthermore, the quantity η begins to decrease and the temperature curve has no singularities at the point at which this decrease starts to occur. The combustion center does not penetrate the axial part of a cylindrical sample. This is consistent with the fact that the circle length along which the pulse runs cannot be shorter than the pulse size. The distance between the loops, which was found in [9], is on the order of the heating-zone width (see [10]), although, numerically, it is longer by an approximate factor of two.

The effective value of $Z \approx 7$ is determined according to the magnitude of the temperature maximum. We can estimate the effective value of the Damcöler number according to the width of the recovery zone: $D \sim 100 \approx \frac{1}{u_a^2}$ (u_a is the velocity of motion along the cylinder axis). In other words, in the units employed in this paper, this is the content renewal time in the heating zone (in a reactor). Using plots for η and θ, which are presented in [9], we find $x_1 \approx 60$ and $\theta_1 \approx -3.5$, whereas from (9), we obtain $\theta_1 \approx -3.7$ (with allowance for $A \approx 0.06$). Finally, substituting the obtained numerical values into expression (14), we find $S \approx \frac{D}{2} \sim 50$. The relation between the quantities S and D can be clarified if we remember that the mass exchange in a disk reactor proceeds only in the axial direction, whereas the heat removal occurs in both axial and radial directions. Meanwhile, the value of S obtained is lower than the quantity S_{th} determined from formula (16). This implies that the model of a disk reactor, as applied to the spin combustion, needs to be modified. To do this, it is necessary to take into account the stabilizing action of heated condensed products (see [11]). The thermal reservoir adjoining the disk must decrease the threshold for propagating the pulses.

ACKNOWLEDGMENTS

The author is grateful to A.Yu. Dovzhenko, T.I. Ivleva, and A.G. Merzhanov for fruitful discussions.

This work was supported by the Russian Foundation for Basic Research, project no. 01-03-32772.

REFERENCES

1. V. A. Vasil'ev, Yu. M. Romanovskiĭ, and V. G. Yakhno, Usp. Fiz. Nauk **128**, 625 (1979) [Sov. Phys. Usp. **22**, 615 (1979)].
2. B. S. Kerner and V. V. Osipov, Usp. Fiz. Nauk **157**, 201 (1989) [Sov. Phys. Usp. **32**, 101 (1989)].
3. A. G. Merzhanov and E. N. Rumanov, Rev. Mod. Phys. **71**, 1173 (1999).
4. Ya. B. Zel'dovich, Zh. Éksp. Teor. Fiz. **11**, 159 (1941).
5. A. G. Merzhanov, V. V. Barelko, I. I. Kurochka, and K. G. Shkadinskiĭ, Dokl. Akad. Nauk SSSR **221**, 1114 (1975).
6. E. N. Rumanov, Int. J. Self-Propag. High-Temp. Synth. **10**, 367 (2001).
7. D. A. Frank-Kamenetskiĭ and I. E. Sal'nikov, Zh. Fiz. Khim. **17**, 79 (1943).
8. D. A. Vaganov, N. G. Samoilenko, and V. G. Abramov, Chem. Eng. Sci. **33**, 1133 (1978).
9. T. P. Ivleva and A. G. Merzhanov, Dokl. Akad. Nauk **369**, 186 (1999) [Dokl. Phys. **44**, 739 (1999)].
10. B. V. Novozhilov, Dokl. Akad. Nauk **326**, 485 (1992).
11. A. G. Merzhanov, Arch. Combust. **191**, 23 (1981).

Translated by G. Merzon

Doklady Physics, Vol. 48, No. 11, 2003, pp. 622–626. Translated from Doklady Akademii Nauk, Vol. 393, No. 3, 2003, pp. 321–325.

PHYSICS

Model of Redistribution of Components in Surface Layers of Amorphous Alloys in a Metal–Metalloid System Under Deformation and Low-Temperature Loadings

M. A. Baranov, I. B. Volkova, and V. Ya. Bayankin

Presented by Academician A.M. Lipanov August 11, 2003

Received July 30, 2003

In this paper, a model is constructed explaining diffusion of metalloid atoms in amorphous bodies of a metal–metalloid systems under mechanical and low-temperature actions. The model is based on previous experimental results related to nonequilibrium segregations in amorphous alloys in low-temperature conditions (room and lower temperatures). While developing the model, the theory of motion of macroscopic inclusions which has been proposed by Geguzin and Krivoglaz was used. The limits of applicability of the model are determined.

In spite of the fact that diffusion in amorphous alloys has already been studied for three decades, the problem cannot be considered closed. The low-temperature region (in the order of room temperatures and lower) remains the least understood. The investigation of the problem is hampered by the fact that diffusion is suppressed at low temperatures. Therefore, it is impossible to use direct methods to obtain quantitative characteristics of the process. However, it seems to be possible to study quantitative characteristics of diffusion in amorphous alloys by indirect methods, namely, by analyzing results of experiments in which nonequilibrium segregations were studied in conditions of external actions.

1. THE RESULTS OF ORIGINAL EXPERIMENTS

In this study, we analyze two experimental results testifying to the redistribution of chemical components in surface layers of amorphous alloys of the metal–metalloid type in the presence of external actions (nonequilibrium segregations). These experimental results cannot be explained on the basis of classical diffusion models [1, 2].

Physicotechnical Institute, Ural Division, Russian Academy of Sciences, ul. Kirova 132, Izhevsk, 426000 Russia

In [3], deformation of a rapidly hardened $Fe_{80}B_{20}$ amorphous 10-μm thick band was realized. The hardening was performed by the method of simple bending on a holder whose diameter was commensurable with the band thickness. The calculated degree of deformation of band surface layers attained 100%. The analysis was carried out by local Auger electron spectroscopy using a JAMP/10s probe accompanied by a layer-by-layer analysis based on etching the sample with argon ions. The etching rate was ~1.0 nm min^{-1}. In all measurements, the relative error of the quantitative analysis did not exceed 15%. The atomic structure of both the original and processed samples was verified by X-ray radiography methods. According to the results of X-ray radiography, after mechanical processing the samples conserved their amorphous structure. As is seen from Fig. 1, the tensile deformation raised the iron atom content in near-surface layers by 16 at.% and lowered the boron atom content by 13 at.% with respect to the initial concentration. In contrast, for the case of compression of the amorphous band, an excess of 3% boron atomic content was found. It is worth noting once more that the amorphous band was bent at room temperature when the diffusion of the components was suppressed. In order to describe similar processes, the classical formula (see [4])

$$\mathbf{I} = \frac{D}{3fkT}\nabla\sigma \tag{1}$$

and the formula describing the average velocity of a diffusing particle

$$\mathbf{v} = \frac{D\omega}{3fkT}\nabla\sigma \tag{2}$$

are commonly used. Here, I is the flow intensity for a diffusing chemical element, D is diffusivity, ω is the atomic volume, T is the absolute temperature, k is the Boltzmann constant, f is the correlation factor, and $\nabla\sigma$ is the stress gradient.

Data on metalloid diffusion in amorphous alloys at room temperature are practically nonexistent. Assuming that no Arrhenius-like dependence for light atoms

1028-3358/03/4811-0622$24.00

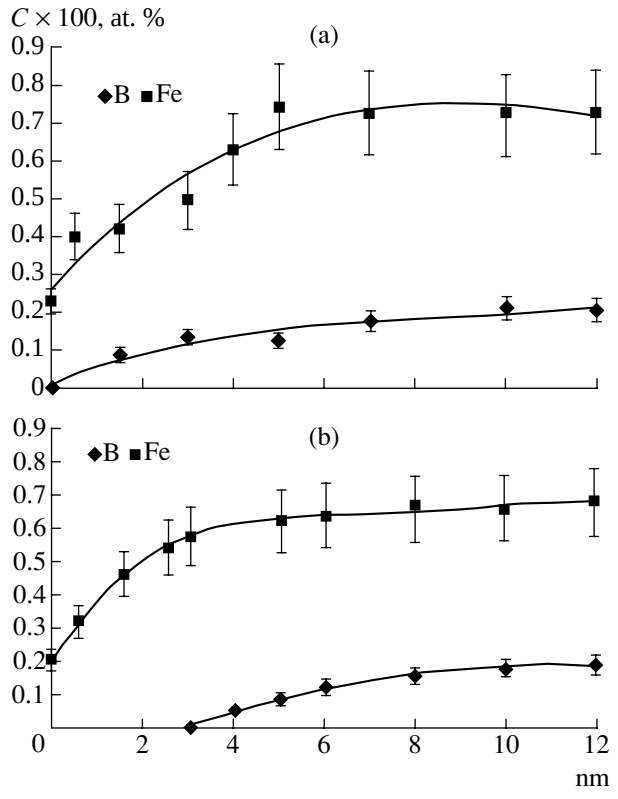

Fig. 1. Distribution of chemical elements in the surface layer of the amorphous $Fe_{80}B_{20}$ sample: (a) initial distribution; (b) post-deformation distribution.

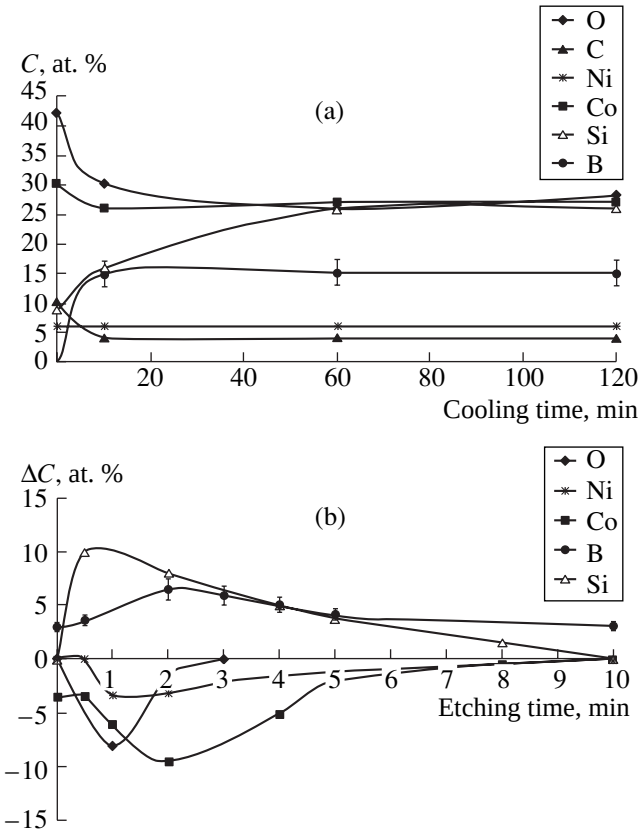

Fig. 2. Distribution of chemical elements in the case of low-temperature processing of amorphous $Co_{57}Ni_{10}Fe_5Si_{11}B_{17}$ alloy: (a) surface concentration as a function of processing time; (b) depth variation of the concentration in the case of holding in liquid nitrogen for 10 min.

within the given temperature interval is observed [1, 2], the maximal diffusion coefficient of boron atoms can be estimated as $D \sim 10^{-22}$ m^2 s^{-1}. With allowance for $T \sim 10^2$ K, and $\omega \sim 10^{-29}$ m^3, $\sigma = K\frac{\delta V}{V}$, $K \sim 165.5 \times 10^9$ J m^{-3}, $\frac{\delta\sigma}{L_k} = \frac{1}{V}K\frac{\delta V}{\delta x} \sim 10^{15}$–$10^{16}$ J m^{-4}, we arrive at $v \sim 10^{-15}$–10^{-17} m s^{-1}, or $v \sim 10^{-6}$–10^{-8} nm s^{-1}. The value of the diffusion rate found by this method is smaller by several orders of magnitude than experimental values. This implies that at least from the classical standpoint, an explanation of this phenomenon is not evident.

An even more surprising experimental fact concerns the migration of boron atoms while freezing amorphous samples. In [5], redistribution of chemical elements in an amorphous magnetically soft $Co_{57}Ni_{10}Fe_5Si_{11}B_{17}$ alloy was studied in low-temperature conditions (77 K). Samples in the form of amorphous bands ~20 μm thick and ~10 mm wide were held in liquid nitrogen for 10, 60, and 120 s. Furthermore, at room temperature, the layer-by-layer elemental analysis using Auger electron spectroscopy was performed. As in the first experiment, the atomic structure of both the original and processed samples was verified using the X-ray radiography method. It was revealed that low-temperature processing did not lead to noticeable changes in the alloy structure: according to X-ray radiography, the samples remained amorphous. The surface redistribution of the components was estimated during the 30 s ionic cleaning of the samples. After this cleaning of the surface (~0.5 nm), impurities and adsorbed admixtures were practically absent. As follows from Fig. 2, the low-temperature processing stimulated concentration changes in the surface layers of the alloy. These changes correlate with variations of mechanical and corrosion properties of the material. Using formula (2), and the value of $\frac{\delta\sigma}{L_k} \sim K\alpha_v \nabla T \sim 10^9$–$10^{10}$ J m^{-4}, $T \sim 10^2$ K, we arrive at $v \sim 10^{-19}$–10^{-21} m s^{-1} (where K is Young's modulus, and α_v is the coefficient of volume expansion). In the case under consideration, the classical approach predicts an even lower value for the diffusion rate. The given experimental data are not unique. In recent years, similar systematized data appeared [6, 7].

We can attempt to explain these experimental results under the assumption that boron atoms move together

with metal–metalloid clusters. The existence of such clusters, or at least of strong bonds between atoms of metalloid and metal, is confirmed by the experimental data of [8] and theoretical conclusions of [9], as well as by the results of molecular-dynamic modeling in [10, 11].

In spite of these results, the most well-known models describing motion of metalloids in amorphous alloy either do not take into account the aforementioned fact or exploit assumptions that make it possible to easily ignore it [3, 6, 7].

One of the most adequate theories describing the motion of such clusters seems to be the theory of motion of macroscopic inclusions in solids which was proposed by Geguzin and Krivoglaz [4]. In the first turn, this theory was developed for the description of the behavior of microscopic pores filled with gas inside crystalline solids. However, we may state that there are no constraints prohibiting the application of this theory in describing the motion of microscopic-size metal–metalloid clusters in amorphous bodies. This statement is based on the following facts.

(1) The theory of Geguzin and Krivoglaz is phenomenological and does not describe the microscopic mechanism of migrating inclusions. For successful application of the theory, only the appearance of certain conditions on the inclusion–matrix interface is necessary. In our case, this is the assumption on the feasibility of near-boundary (surface) diffusion of amorphous-alloy atoms along the cluster-amorphous-alloy interface. In the same study [4], a wide list of experimental data was presented confirming the possibility of applying the theory describing motion of macroscopic inclusions that reside in different aggregate states (gas, liquid, solid) in solids.

(2) A possibility of using the theory of Geguzin and Krivogaz to describe microscopic-size objects is also proved in [4]. It is theoretically shown there that decreasing inclusion size does not restrict the applicability range of the theory. In this case, the inclusions acquire an ability of migrating not only in the presence of a gradient of a certain (temperature, elastic-stress, vacancy concentration) field but owing to their independent Brownian motion. In that study, the experimental confirmation of this concept is given, as an example, for Brownian motion of gas-filled cavities in UO_2 plates (with a minimal cavity size of ~ 33Å).

As one more argument favoring the validity of this theory, we can present the results of molecular-dynamical modeling performed in [10, 11]. In these studies, the possibility of migrations of boron atoms incorporated into FeB clusters is shown for an $Fe_{80}B_{20}$ system, as an example, for conditions simulating experimental ones in the case of mechanical and low-temperature loading amorphous bands. The direction of cluster motion corresponded to that in the experiments. The migration of boron incorporated into clusters was confirmed visually according both to dynamics of cluster images in numerical experiments and to the results of analysis of the radial distribution function.

Here, it is worth emphasizing that for more successful application of the given theory, we should introduce an important assumption on the existence of a boundary layer (planar formations) around the clusters. Below, we analyze the results of employing the theoretical approach proposed in [4] to the explanation of our experimental results described above.

2. APPLICATION OF THE MODEL FOR DESCRIBING THE EXPERIMENT ON BENDING A $Fe_{80}B_{20}$ AMORPHOUS BAND

In accordance with the data obtained in [4], the inclusion velocity of motion in the stress field caused by surface diffusion flows is determined by the formula

$$\mathbf{v} = -\frac{10}{3}\frac{\omega D_s}{f_s kT}\frac{a}{R}\sigma_1 \mathbf{e}_z. \quad (3)$$

Here, $\mathbf{v}$ is the macroscopic-inclusion velocity of motion with respect to the surface; $\sigma_1 \sim \frac{\delta\sigma_{nn}}{L_k}$ is the stress gradient; L_k is the mean cluster size; D_s is the boundary diffusivity of matrix atoms (Fe, in our case); ω is the atomic volume; T is temperature; f_s is the surface correlation factor; $\mathbf{e}_z$ is the unit vector co-directed with the stress gradient; R is the distance on the order of the inclusion radius; and a is the thickness of the localization layer for boundary flow.

We try to apply formula (3) to describe the experiment with mechanical action on the amorphous alloy. If we take $\frac{\delta\sigma_{nn}}{L_k} \sim \frac{1}{V}K\frac{\delta V}{\delta x} \sim 10^{15}$–$10^{16}$ J m^{-4}, $\frac{a}{R} \sim 10^{-1}$–10^{-3}, $T \sim 10^2$ K, $\nu \sim 10^{-9}$ m s^{-1}, $\omega \sim 10^{-29}$ m^3, then we can calculate $D_s \sim 10^{-11}$–10^{-16} m s^{-2}.

We now analyze, whether this value of the boundary diffusion coefficient is reliable. It is well known [12] that in crystals, the activation energy of boundary diffusion is smaller by a factor of two to three than the activation energy of the bulk diffusion. At the same time, in most cases the value of the pre-exponential factor lies within the range 10^{-9}–10^{-6} m^2 s^{-1}. Assuming that this situation is preserved in amorphous alloys (i.e., the activation energy for boundary diffusion is smaller by a factor of two to three than that of bulk diffusion in amorphous alloys), the value D_s at 300 K can attain 10^{-14} m^2 s^{-1}, which is consistent with the required value. Undoubtedly, this analysis is not a rigorous proof. However, the assumed existence of a high boundary diffusion coefficient is plainer than that of a high bulk diffusion coefficient because it follows from classical premises.

As follows from formula (3), the direction of motion for clusters containing boron coincides with the direction observed in experiments. Moreover, if we consider

that the stress gradient in the displacement region is constant, then the boron concentration at an arbitrary moment of time is determined by the parallel transfer formula $c(x, t) = c_0(x + vt)$, which is actually observed in experiments, Fig. 1.

3. APPLICATION OF THE MODEL FOR DESCRIBING THE EXPERIMEMT OF COOLING THE $Co_{57}Ni_{10}Fe_5Si_{11}B_{17}$ AMORPHOUS BAND

In the experiment associated with the influence of low temperature on an amorphous alloy, the quantity $\frac{\delta\sigma}{L_k}$ is determined by the formula

$$\frac{\delta\sigma}{L_k} = K\alpha_v|\nabla T|, \quad (4)$$

where K is the bulk Young modulus, α_v is the coefficient of volume expansion, and ∇T is the temperature gradient that arises while cooling samples. It follows from the aforementioned that, in the framework of the model proposed, the displacement of atoms in the near-surface layers of the amorphous band occurs only during its cooling.

We now make an attempt to estimate the diffusion coefficient for which the indicated mechanism is feasible. To do this, we first evaluate the cooling rate for amorphous samples placed into liquid nitrogen. In accordance with the results of [13] and when the Biot criterion is $\mathrm{Bi} \ll 0.01$, the formula

$$\Theta = \frac{x^2}{2r^2}\mathrm{Bi}e^{-\mathrm{Bi}\cdot\mathrm{Fo}} \quad (5)$$

is true, where Bi is the Biot criterion [13] and Fo is the Fourier criterion (Fourier number) [13]; r is the half-width of the plate being cooled (in this case, of the amorphous band); x is the coordinate of the point at which the temperature is calculated; and Θ is the dimensionless temperature determined by the formula

$$\Theta = \frac{T - T_{\mathrm{am}}}{T_0 - T_{\mathrm{am}}}. \quad (6)$$

In formula (6), T is the current temperature of the plate and T_{am} is the temperature of the ambient medium. Here, we understand (similarly to the approach of [6, 7]) that when immersing the sample in liquid nitrogen, its surface does not instantaneously acquire the temperature of the liquid nitrogen. Formula (5) is obtained under the assumption that a temporal layer is formed around the sample. This layer consists of nitrogen vapor and prevents intense heat loss. Thus, the boundary conditions proposed are more rigid for constructing the model compared to those proposed in [6, 7], because these conditions lead to appearance of considerably weaker thermodynamic forces.

In our case, $\mathrm{Bi} \sim 10^{-4}$ and $\mathrm{Fo} \sim 10^4$, where τ is the temperature relaxation time. Hence, the characteristic time of plate (amorphous band) cooling is on the order of 1 s. For this time, the temperature gradient on the order of 10^3 K m^{-1} exists on the plate surface. During this time, metalloid atoms must shift by a distance on the order of 1 nm, i.e., the cluster motion velocity must be about 1 nm s^{-1} or 10^{-9} m s^{-1}. In addition, $\omega \sim 10^{-29}$ m^3, $k \sim 10^{-23}$ J K^{-1}, $f_s \sim 1$, $a \sim 10^{-10}$ m, $R \sim 10^{-9}$–10^{-8} m, and $\frac{\delta\sigma}{L_k} \sim 10^9$–$10^{10}$ J m^{-4}. As a result, we find the value for the coefficient of the boundary diffusion: $D_s \sim 10^{-8}$–10^{-13} m^2 s^{-1}, which corresponds to the range obtained from the experiment of bending the amorphous band.

DISCUSSION

The advantage of the proposed mechanism of the migration of metalloid atoms incorporated into metal–metalloid clusters is that it brings the possibility of jointly explaining three experimental results at once:

The existence of nonequilibrium segregations caused by mechanical action on an amorphous alloy;

The presence of nonequilibrium segregations caused by low-temperature action on an amorphous alloy;

A possibility of diffusion of metalloid atoms in the case of simultaneous existence of metal–metalloid clusters in amorphous alloys.

In addition, in the framework of the mechanism proposed, we have managed to explain the deviation of the diffusion coefficient from the Arrhenius dependence, which was observed in a number of experiments [1, 2]. It is well known that the behavior of the diffusion coefficient for light atoms in amorphous alloys does not obey the Arrhenius law, and the value of this coefficient at temperatures of 250–300 K lies within the interval 10^{-20}–10^{-24} K. As was noted previously, according to the theory of the motion of macroscopic inclusions, it was shown [4] that macroscopic inclusions are capable of Brownian motion. In this case, the diffusion coefficient D_{cl} for a macroscopic inclusions (in our case for a metal–metalloid cluster) and the coefficient of boundary diffusion are linked by the relationship

$$D_{\mathrm{cl}} \approx \left(\frac{a}{R}\right)^4 D_s.$$

Thus, the value of D_{cl} is on the order of 10^{-19}–10^{-22} m^2 s^{-1}, which is very consistent with experimental data (provided that the cluster diffusion coefficient corresponds to the boron diffusion coefficient measured in the experiments).

Analysis of nonequilibrium segregations in amorphous alloys made it possible to propose a mechanism of migration of metalloid atoms in amorphous alloys, which are incorporated into metal–metalloid clusters.

The model proposed is based on the theory of the motion of macroscopic inclusions developed by Geguzin and Krivoglaz [4]. For successful application of the given theory, it is assumed that boundaries (planar formations) exist around the clusters. The adequacy of the model proposed is stipulated by the possibility of exhaustive explanation of four independent experimental results and the results of molecular-dynamic modeling.

REFERENCES

1. *Glassy Metals*, Vol. 2: *Atomic Structure and Dynamics, Electronics Structure, Magnetic Properties*, Ed. by H. J. Güntherodt and H. Beck (Springer, Heidelberg, 1984; Mir, Moscow, 1986).
2. *Proceedings of the 5th International Conference on Quick Hardened Metallic Alloys*, Ed. by S. Shtib and G. Varlimont (Metallurgiya, Moscow, 1989), pp. 151–159.
3. I. B. Volkova and V. Ya. Bayankin, Fiz. Met. Metalloved. **79** (5), 107 (1995).
4. Ya. E. Geguzin and M. A. Krivoglaz, *Motion of Macroscopic Inclusions in Solids* (Metallurgiya, Moscow, 1971).
5. V. Ya. Bayankin, V. Yu. Vasil'ev, I. B. Volkova, and L. Yu. Marizina, Fiz. Khim. Obrab. Mater., No. 3, 48 (1994).
6. S. G. Zaĭchenko, A. M. Glezer, E. A. Gan'shina, *et al.*, Dokl. Akad. Nauk **367**, 478 (1999) [Dokl. Phys. **44**, 545 (1999)].
7. S. G. Zaĭchenko and A. M. Glezer, Materialovedenie, No. 11, 2 (2002).
8. *Amorphous Metallic Materials*, Ed. by A. I. Manokhin (Nauka, Moscow, 1984), pp. 28–33.
9. M. Kh. Shorshorov, *Ultradisperse Structural State of Metal Alloys* (Nauka, Moscow, 2001).
10. I. B. Volkova, M. A. Baranov, and V. Ya. Bayankin, Materialovedenie, No. 6, 2 (1998).
11. M. A. Baranov and V. Ya. Bayankin, Materialovedenie, No. 4, 18 (1999).
12. B. S. Bokshteĭn, *Diffusion in Metals* (Metallurgiya, Moscow, 1978).
13. A. V. Lykov, *The Theory of Heat Transfer* (Vyssh. Shkola, Moscow, 1967).

Translated by G. Merzon

Doklady Physics, Vol. 48, No. 11, 2003, pp. 627–632. Translated from Doklady Akademii Nauk, Vol. 393, No. 3, 2003, pp. 326–331.

PHYSICS

Time Features of the Dynamic Failure of Metals Attributable to the Hierarchic Properties of Dissipative Structures—Cascade of Failure Centers

Academician R. I. Il'kaev, V. T. Punin, A. Ya. Uchaev*, S. A. Novikov, E. V. Kosheleva, L. A. Platonova, N. I. Sel'chenkova, and N. A. Yukina

Received July 24, 2003

Results presented in [1–4] point to the universal properties of the behavior of metals dynamically destroyed under the action of intense radiation pulses. These properties are attributed to the self-organization of the failure centers and instabilities in dissipative structures (failure center cascades) providing the basis of the resistance of a body to an external action. The amplitude of the pulse pressure can be in the area of a few to a few hundred kilobars for longevity ranges $t \sim 10^{-6}$–10^{-10} s. In this case, the evolution under dynamic failure of micro- and mesoscopic defects and of failure center cascades constitutes the general properties of the invariant behavior of solids subjected to a thermal shock induced by intense radiation pulses (initial temperature $T_0 \sim 4\text{K} - 0.8T_\text{m}$, energy-insertion rate $\frac{dE}{dt} \sim 10^6$–10^{12} K/s, and absorbed energy density 10–10^4 J/g) [1–4].

It is known that metals under failure exhibit plastic deformation in both quasistatic ($t > 10^{-3}$ s) and dynamic ($t < 10^{-6}$ s) longevity ranges [5]. For small plastic strains, this process is attributed to the evolution of various crystal defects, which, interacting with each other and subjected to an external action, remain individual structural units with inherent properties. Plastic deformation is attributed to the ergodic behavior [6] of the set of defects whose trajectories gradually fill all the phase space. The thermodynamic potential of the set of defects has the form of a "regular" distribution of minima, the lowest of which corresponds to the stable state of the set of defects and others to metastable states. In this case, hierarchical subordination in the behavior of defects of the crystal lattice is also absent. For small plastic strains, the evolution of the set of crystal lattice defects under plastic deformation is represented as a chain of thermal fluctuation Debye processes for overcoming energy barriers [6, 7].

For large plastic strains, the density of various crystal-structure defects can reach critical values. Collective effects are manifested in the behavior of defects, or the appearance of certain bonds in the ensemble of defects. A coupling in an ensemble of one structural level of defects stimulates the self-similar formation of another structural level of defects, which serves as the initial structural level for the higher level [8]. Nonequilibrium hierarchical coordination systems, where the upper state can be achieved only when lower states are achieved, are usually nonergodic [6, 9]. In a hierarchical system where a relaxation time spectrum exists, fast processes responsible for overcoming the lowest potential barriers proceed at the start. This behavior gives rise to the nonergodic behavior of hierarchical systems, such as a broken solid with dynamic longevity.

As an example, we consider the self-organization of various dissipative structures that occurs on three levels in the bulk of the destroyed solid in the dynamic longevity range. As was shown in [1–4], the crystal lattice loses the long-range order near the formed failure centers. The structure of shear bands in metals was studied for various types of pulsed loads. Figure 1 shows the hierarchy of shear bands around failure centers in titanium after the shock wave load [10]. Data presented in Fig. 1 shows that the cascade of shear bands around failure centers is a fractal cluster. Fractal systems are hierarchical. Therefore, the adequate description of dynamic failure by classical kinetic methods is questionable.

As was shown previously [1–4, 11, 12], the cascade of failure centers, which determines the dynamic failure of metals, is a fractal cluster. Represented in the universal coordinates, the distribution of failure centers for various materials is obtained by the similarity transformation. This indicates that dynamic failure proceeds in metals through one predominant process—accumu-

Russian Federal Nuclear Center All-Russia Research Institute of Experimental Physics, pr. Mira 37, Sarov, Nizhegorodskaya oblast, 607188 Russia

** e-mail: uchaev@expd.vniief.ru*

1028-3358/03/4811-0627$24.00

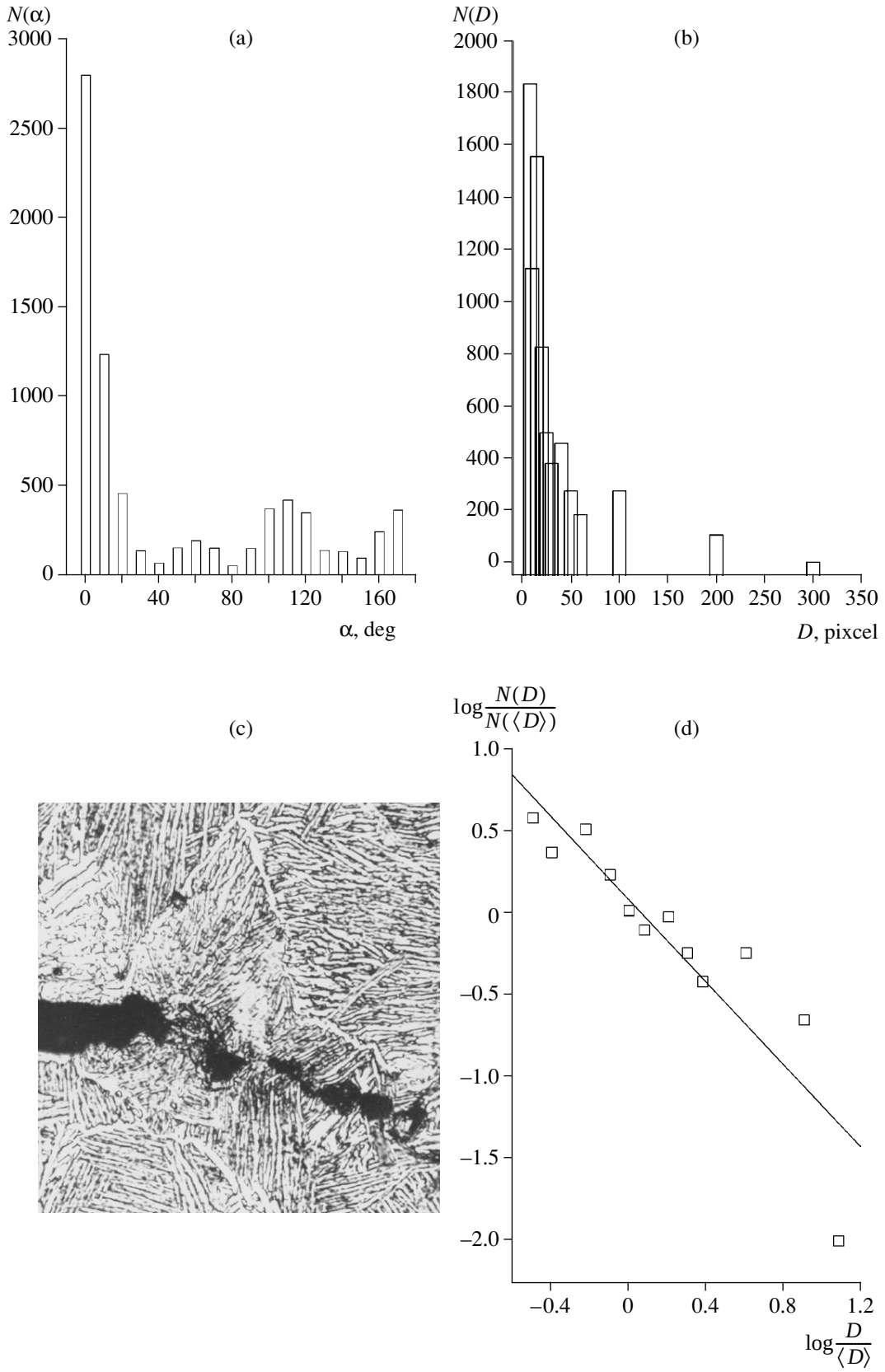

Fig. 1. Results of the treatment of the Ti metallographic specimen ($T = -196$°C, magnification of 300) as obtained by the software package of the interactive system of image analysis [4, 9]: (a) angular and (b) size distributions of shear bands, (c) metallographic specimen pattern, and (d) fractal dimension of shear bands.

lation and growth of failure centers—ensuring the principal part of longevity. The spectral size distribution of failure centers in loaded metallographic specimens parallel and perpendicular to the failure surface has the form $N(D) \sim D^{-\alpha}$, where N and D are the number and size of failure centers, respectively, and $\alpha > 1$. Investigations revealed the correlated behavior and appearance of the self-organization of the cascade of failure centers in the destroyed-specimen scale [1–4, 11].

The size of failure centers and their density in a destroyed solid at the final stage of the dynamic failure are controlled by the concentration criterion [1, 2]. The results shown in Fig. 2 testify to the collective behavior of the ensemble of failure centers, which is attributed to the nonequilibrium state of the solid (absorbed energy density is commensurate with the energy parameters of the crystal lattice) [1–4]. The self-maintaining behavior of the cascade of failure centers when the concentration criterion is satisfied is caused by the loss of ergodicity in the behavior of the ensemble of failure centers, which is, in turn, associated with hierarchical coordination [6].

As was previously shown in [4], the thermodynamic potential, enthalpy, determines the dynamic failure in the dynamic longevity range. The ratio of the absorbed energy density to the energy parameters of the crystal lattice (enthalpy and phase-transition heat) is an invariant of the metal behavior with respect to external actions. In this case, the limiting deformation energy density of the local volume of the broken body (near failure centers) can be taken as (see, e.g., [13])

$$Q^{\max} = \int_{T'}^{T_m} C_p^{(T)} dT + L_m.$$

Here, L_m is the latent melting temperature of the crystal lattice, $H = \int_{T'}^{T_m} C_p dT$ is enthalpy, C_p is the heat capacity at constant pressure, T' is the temperature below which the contribution of thermal atomic oscillations to the internal energy density is negligible, and T_m is the melting point.

The potential energy of an n-level system is written in the form

$$U_2 = U_2(\rho_1, U_1),$$
$$U_3 = U_3(\rho_2, U_2),$$
$$\ldots$$
$$U_n = U_n(\rho_{n-1}, U_{n-1}),$$

where ρ_n is the density of structural units at the nth level. The total energy is expressed as

$$U_{tot} = \sum_i U_i \rho_i.$$

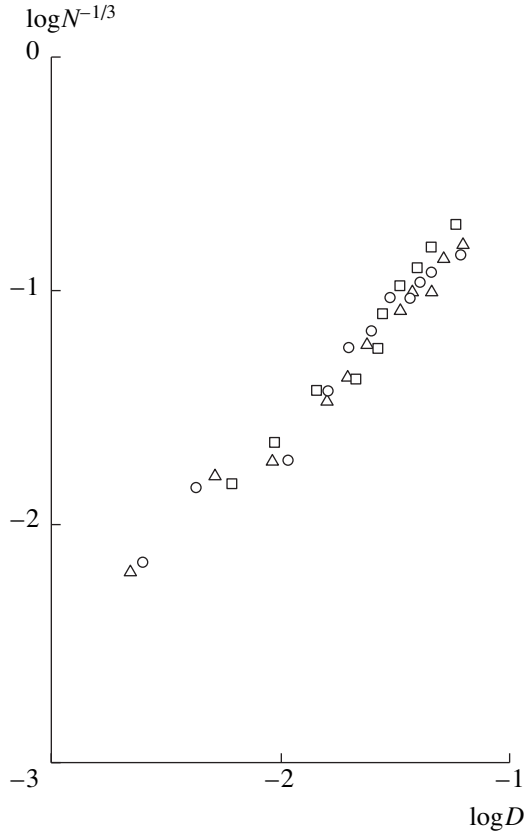

Fig. 2. Average distance $\langle r \rangle = N^{-1/3}$ between failure centers as a function of the failure-center size D for (triangles) copper, 0.37 mm; (circles) bronze, 0.3 mm, and (squares) iron, 0.5 mm.

Since the maximum energy density that can be accumulated in the unstable zones of the crystal lattice [4] without change in the aggregation state is equal to $E = H + L_m$,

$$\sum_i U_i \rho_i = \int_{T_0}^{T_m} C_p dT + L_m. \quad (1)$$

This expression considerably simplifies the description of a dynamically loaded solid in the dynamic longevity range.

Figure 3a shows systematized data [14] for the charge-number z dependence of the binding energy E_b, lattice constant a, elastic modulus E, and enthalpy and phase-transition heat $H + L_m$. These data testify to the absence of correlation in these parameters. Figure 3b shows the charge-number dependence of the critical energy E_{cr} leading to the failure of indicated metals in the dynamic longevity range under the action of the thermal shock induced by intense radiation pulses [4].

Generalizing and analyzing the results taken from [1–4] with the use of expression (1), we arrive at

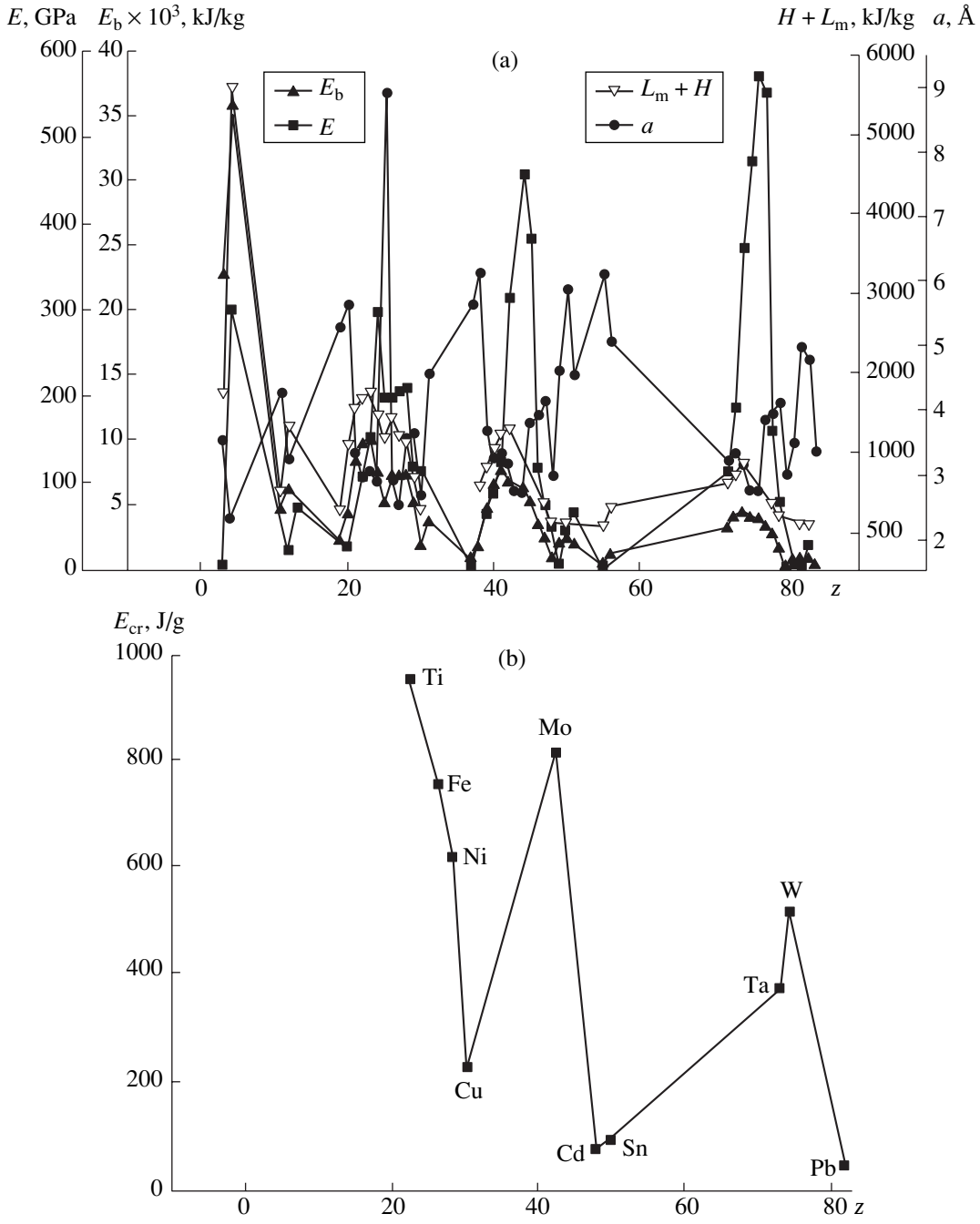

Fig. 3. Atomic-number dependence of (a) (close triangles) binding energy E_b, (circles) lattice constant a, (squares) elastic modulus E, (open triangles) enthalpy and phase-transition heat $H + L_m$, and (b) critical pressure E_{cr} leading to the failure of indicated metals for a longevity of about 10^{-8} s.

the failure surface shown in Fig. 4 in the coordinates including the dynamic invariant $I(t) = \dfrac{P_{cr}(t)}{\Gamma\rho(H + L_m)}$, atomic number z of the element, and longevity t. The dashed lines on the failure surface are experimental data for Al, Ti, Fe, Ni, Cu, Cd, Sn, Ta, W, and Pb [1–4]. To adequately describe dynamic failure induced by a thermal shock, it is necessary to know the dynamic invariant $I(t) = \dfrac{E(t)}{H + L_m}$, where $E(t)$ is the critical absorbed energy leading to macroscopic failure changing the connectivity of the body for certain longevity t. This dynamic invariant takes values in the range $I \sim 0.3–1$ (dynamic longevity range is $t \sim 10^{-6}–10^{-10}$ s). With an increase in I, when $I > 1$ (milling, dispersing), it is not necessary to consider the process at different scale levels.

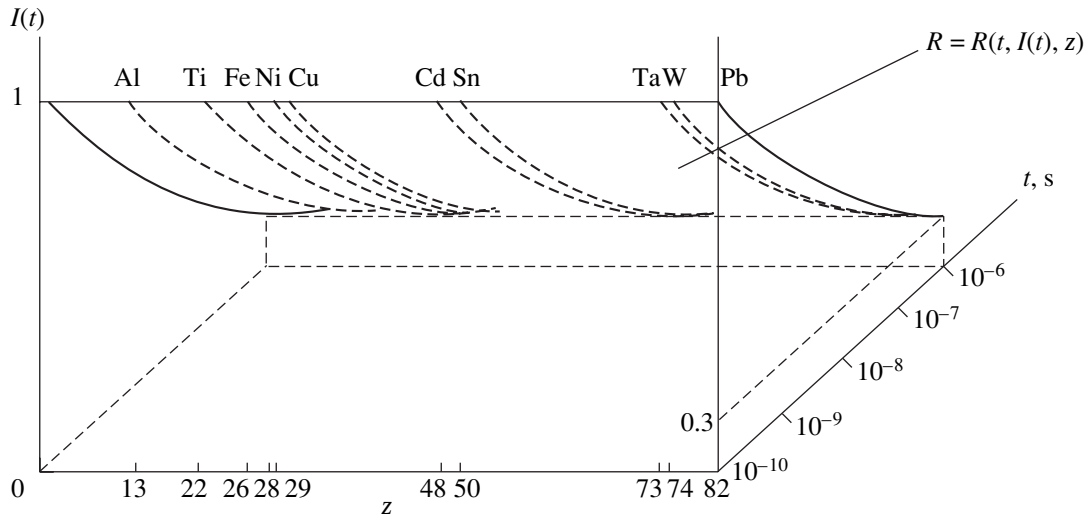

Fig. 4. Schematic representation of the failure surface in the coordinates including the dynamic invariant $I(t) = \frac{P_{cr}(t)}{\Gamma\rho(H+L)}$, atomic number z of the element, and longevity t.

The potential energy U corresponding to each hierarchic level of the dissipative structures, which is characterized by its order parameter n_i, distribution function f_i, and relaxation time t_i, enters into quantity $I(t)$ in the integral form. For the dynamic invariant $I(t) < 0.3$–1, the absorbed energy E is lower than the energy E_{cr} leading to macroscopic failure. To predict the resource of various-geometry materials under multiple loading, it is necessary to study several structural levels of the loaded solid.

Real fractal structures such as the cascade of microcracks, failure centers, and shear bands attract attention after the introduction of the concept of structural levels of deformation and failure [11, 12]. A characteristic feature of such dissipative structures is that their fractal structure is manifested at the simultaneous realization of several structural levels whose scales are so different that it is difficult to represent a graphic geometric (fractal) image in a given scale level. The observation and identification of multiscale structures are hindered. They can be consistently described in the framework of the fractal concept, because such nonequilibrium systems are large ensembles consisting of hierarchically coordinated statistical ensembles that, in turn, consist of a set of subensembles, etc.

Interest in fractals has increased substantially after numerous phenomena and problems had been described where the fractal structure (dimension) was the fundamental characteristic of a system. In [11], we successfully applied such an approach to determine the quantitative characteristics of dissipative structures arising in the process of the dynamic failure of metals and explosives, as well as in the process of the modification of the structure of metals and alloys subjected to pulsed high-current beams of relativistic electrons in the dynamic longevity range ($t \sim 10^{-6}$–10^{-10} s). According to the available data, systems formed under strongly nonequilibrium conditions are fractal systems and characterized by the fractal dimension.

Dynamic failure in specific temperature–time ranges ($t \sim 10^{-6}$–10^{-10} s, $T_0 \sim 4$ K–$0.8T_m$, $\frac{dE}{dt} \sim 10^8$–10^{12} K/s) [1–4, 11] is hierarchic and proceeds through one mechanism—appearance, growth, and accumulation of failure centers—where the bulk of the body near failure centers that are appearing and growing serves as a thermostat.

The reported investigations reveal the hierarchy of the structural levels of dissipative structures determining the dynamic failure of metals in the longevity range $t < 10^{-6}$ s. The formation of dissipative structures is possible only when several structural levels are simultaneously realized. The fractal dimension of the structural levels is a quantitative characteristic of dissipative structures. Dissipative structures at the macroscopic failure threshold have the total potential energy $E = H + L_m$. The proposed method of estimating the total energy of an n-level hierarchic system enables one to introduce a particular mathematical formalism for each structural level of a loaded solid without detailed analysis of each structural level.

The above method determines the possibility of predicting the behavior of unstudied metals under extreme conditions and allows computer "construction" of materials stable to certain test conditions.

REFERENCES

1. A. Ya. Uchaev, N. I. Zavada, R. I. Il'kaev, *et al.*, in *Book of Scientific Works of Russian Federal Nuclear Center*

All-Russia Research Institute of Experimental Physics (RFNC-VNIIÉF, Sarov, 2002), Vol. 3, pp. 304–313.

2. E. K. Bonyushkin, N. I. Zavada, S. A. Novikov, and A. Ya. Uchaev, *Kinetics of Dynamic Fracture of Metals under Pulsed Volumetric Heating* (RFNC-VNIIÉF, Sarov, 1998).
3. E. K. Bonyushkin, B. L. Glushak, N. I. Zavada, *et al.*, Prikl. Mekh. Tekh. Fiz., No. 6, 105 (1996).
4. R. I. Il'kaev, A. Ya. Uchaev, S. A. Novikov, *et al.*, Dokl. Akad. Nauk **384**, 328 (2002) [Dokl. Phys. **47**, 341 (2002)].
5. V. V. Rybin, *Large Plastic Deformations and Fracture of Metals* (Metallurgiya, Moscow, 1986).
6. G. Röpke, *Statistische Mechanik für das Nichtgleichgewicht* (Springer-Verlag, Berlin, 1987; Mir, Moscow, 1990).
7. W. Horsthemke and R. Lefever, *Noise Induced Transitions. Theory and Applications in Physics, Chemistry, and Biology* (Springer-Verlag, Heidelberg, 1984; Mir, Moscow, 1987).
8. V. E. Panin, Yu. V. Grinyaev, V. I. Danilov, *et al.*, *Structural Levels of Plastic Deformation and Failure* (Nauka, Novosibirsk, 1990).
9. R. G. Palmer, Adv. Phys. **31**, 669 (1982).
10. V. K. Golubev, S. A. Novikov, Yu. S. Sobolev, and N. A. Yukina, Fiz.-Khim. Mekh. Mater., No. 2, 112 (1984).
11. A. Ya. Uchaev, N. I. Zavada, E. V. Kosheleva, *et al.*, in *Book of Scientific Works of Russian Federal Nuclear Center All-Russia Research Institute of Experimental Physics* (RFNC-VNIIÉF, Sarov, 2002), Vol. 3, pp. 322–331.
12. V. L. Popov and V. E. Panin, Dokl. Akad. Nauk **352**, 51 (1997) [Phys. Dokl. **42**, 28 (1997)].
13. R. V. Romashov and V. V. Fedotov, Zavod. Lab., No. 2, 229 (1975).
14. M. A. Shtremel', *Strength of Alloys*, Part 1: *Deformation* (Mosk. Inst. Stali Splavov, Moscow, 1997).

Translated by R. Tyapaev

Doklady Physics, Vol. 48, No. 11, 2003, pp. 633–636. Translated from Doklady Akademii Nauk, Vol. 393, No. 3, 2003, pp. 332–335.

PHYSICS

Acoustic Waves in Microinhomogeneous Media with Quadratic Elastic Nonlinearity and Relaxation

V. E. Nazarov and A. V. Radostin

Presented by Academician V.I. Talanov May 16, 2003

Received June 9, 2003

It is common practice to describe propagation of one-dimensional acoustic waves in media possessing quadratic elastic nonlinearity and relaxation properties by the integro-differential equation [1]

$$\frac{\partial V}{\partial x} + \frac{\alpha}{C_0^2} V \frac{\partial V}{\partial \tau} = \frac{m}{2C_0} \frac{\partial}{\partial \tau} \times \int_{-\infty}^{\tau} \frac{\partial V(\tau_1)}{\partial \tau_1} \exp\left(-\frac{\tau - \tau_1}{T}\right) d\tau_1. \quad (1)$$

Here, V is the velocity of particles in the medium; C_0 and C_∞ are low-frequency ($\omega \ll T^{-1}$) and high-frequency ($\omega \gg T^{-1}$) limits of the wave phase velocity; T is the relaxation time; $\tau = t - \frac{x}{C_0}$, $m = \frac{C_\infty^2 - C_0^2}{C_0^2} \ll 1$; and α is the parameter of quadratic nonlinearity. Equation (1) is derived on the basis of the following relaxation equation of state for a medium [1]:

$$p'(\rho') = C_0^2 \rho' + m C_0^2 \int_{-\infty}^{t} \frac{\partial \rho'(\tau_1)}{\partial \tau_1} \times \exp\left(-\frac{t - \tau_1}{T}\right) d\tau_1 + \chi \rho'^2, \quad (2)$$

where p' and ρ' are perturbations of pressure and density, respectively, χ = const, and $\rho' \ll \frac{C_0^2}{\chi}$.

Equation of state (2) corresponds to a homogeneous medium. Its rheological model consists of a chain of equal links. Each of these links is a parallel connection of a standard linear viscous-elastic body and a nonlinear spring [2] (Fig. 1a). In this case, the equation of state for the entire chain coincides with the equation of state for one link of the chain.

Equation (1) describes propagation of steady-state waves of the symmetric-jump type, as well as formation of shock waves or solitons, while exciting periodic perturbations in the medium [1, 3]. As is seen from the rheological model (Fig. 1a) and from Eqs. (1), (2), in a homogeneous medium, only linear relaxation takes place, its nonlinearity being inertialess and frequency-independent.

In [4, 5], the rheological model of a nonlinear microinhomogeneous medium with relaxation properties and containing various microdefects (cracks, dislocations, etc.) was proposed. In these papers, the nonlinear equations were obtained, notably the equation of state and the wave equation for one-dimensional acoustic waves. This model represents a chain of rigid linear springs connected in series and a small number (per unit length of the chain) of soft nonlinear viscous-elastic defects (Fig. 1b). In the case of a microinhomogeneous medium containing identical defects and exhibit-

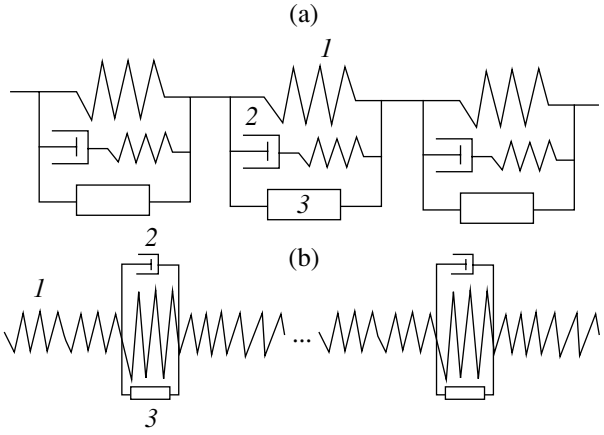

Fig. 1. Rheological models of (a) homogeneous and (b) microinhomogeneous nonlinear media possessing relaxation properties: (*1*) spring; (*2*) linear damper; (*3*) nonlinear element.

Institute of Applied Physics, Russian Academy of Sciences, ul. Ul'yanova 46, Nizhni Novgorod, 603600 Russia
e-mail: nazar@hydro.appl.sci-nnov.ru

1028-3358/03/4811-0633$24.00 © 2003 MAIK "Nauka/Interperiodica"

ing quadratic elastic nonlinearity, these equations have the form

$$\sigma(\varepsilon) = E[\varepsilon - \nu R(\varepsilon) - \nu\gamma\zeta R[R^2(\varepsilon)]], \quad (3)$$

$$\frac{\partial V}{\partial x} + \frac{\nu}{2C}\frac{\partial}{\partial\tau}R(V) - \frac{\nu\gamma\zeta}{2C^2}\frac{\partial}{\partial\tau}R[R^2(V)] = 0, \quad (4)$$

where σ and ε are the stress and strain; E and C are the Young modulus and the wave velocity for a medium free of defects (the value of C also corresponds to the high-frequency limit of the wave velocity in a medium with defects); ν, ζ, Ω, and γ are the concentration ($\nu \ll 1$), relative elasticity ($\zeta \ll 1$), relaxation frequency, and the parameter of the quadratic nonlinearity of defects respectively, $\tau = t - \frac{x}{C}$,

$$R(V) = \frac{\Omega}{\zeta}\int_{-\infty}^{\tau} V(\tau_1)e^{-\Omega(\tau-\tau_1)}d\tau_1,$$

$$V(R) = \frac{\zeta}{\Omega}\frac{\partial R}{\partial\tau} + \zeta R, \quad \gamma\zeta R[R^2(\varepsilon)] \ll |R(\varepsilon)|$$

or

$$\frac{\gamma\zeta}{C}R^2(V) \ll |V|.$$

In such a medium, the small dispersion parameter $m \ll 1$ is determined by the expression $m = \frac{\nu}{\zeta}$. In the model, it is assumed that the linear defect size is much smaller than both the acoustic wavelength and distances between defects. In addition, it is supposed that a lot of defects correspond to the wavelength distance, and their distribution in the chain is statistically uniform [6].

Comparison of rheological models (Fig. 1), of equations of state (2), (3), and of wave equations (1), (4) for above-described media demonstrates certain differences. The basic difference consists in the fact that in addition to the linear relaxation, a microinhomogeneous medium also possesses nonlinear relaxation. This results in a dependence of nonlinearity of a medium on frequencies of interacting acoustic waves, i.e., in dispersion of nonlinearity [4, 5]. In turn, the dispersion of nonlinearity can qualitatively change the character of nonlinear wave propagation in a microinhomogeneous medium (compared to a homogenous medium).

In this paper, we analyze in the framework of Eq. (4) nonlinear wave processes in microinhomogeneous media possessing relaxation properties. We imply propagation of steady-state waves of the asymmetric-jump type and distortion of low-frequency (LF) and high-frequency (HF) initially harmonic waves.

From cumbersome integro-differential equation (4) with respect to the variable V, after simple transformations analogous to those performed in [1] we can obtain the following simpler evolution equation with respect to V and $R(V)$:

$$\frac{\partial}{\partial x}\left(\frac{1}{\Omega}\frac{\partial V}{\partial\tau} + V\right) + \frac{\nu}{2C\zeta}\frac{\partial}{\partial\tau}\left(V - \frac{\gamma\zeta}{C}R^2(V)\right) = 0, \quad (5)$$

$$\frac{\partial}{\partial x}\left(\frac{1}{\Omega^2}\frac{\partial^2 R}{\partial\tau^2} + \frac{2}{\Omega}\frac{\partial R}{\partial\tau} + R\right) + \frac{\nu}{2C\zeta}\frac{\partial}{\partial\tau} \times\left(\frac{1}{\Omega}\frac{\partial R}{\partial\tau} + R - \frac{\gamma}{C}R^2\right) = 0. \quad (6)$$

Furthermore, similarly to [1], we seek the steady-state solution to Eq. (6) in the form $R = R(\eta)$, where $\eta = \tau - bx$, and b = const. Assuming $\gamma > 0$, $R(\infty) = R_0 = \frac{V_0}{\zeta} > 0$, $R(-\infty) = 0$ (and in both cases, $\frac{dR}{d\eta} = 0$), we obtain from (6) the equation for the nonlinear oscillator in the case of $Q = \frac{R}{R_0}$. This oscillator determines the profile of a steady-state wave, namely, of asymmetric jump $1 \to 0$, which moves at a velocity $C_S(\mu)$ with respect to the immobile coordinate system:

$$\frac{d^2Q}{d\theta^2} + (1-\mu)\frac{dQ}{d\theta} - \mu Q(1-Q) = 0, \quad (7)$$

$$C_S(\mu) = C\left(1 + \frac{\nu}{2\zeta(1+\mu)}\right)^{-1} C, \quad (8)$$

where

$$b = \frac{\nu}{2\zeta C(1+\mu)}, \ \mu = \frac{\gamma V_0/\zeta C}{1 - \gamma V_0/\zeta C}1,$$

$$\frac{\gamma V_0}{\zeta C} \ll 1, \ \theta = \Omega\eta.$$

We failed to solve Eq. (7) in the analytical form, therefore we analyze it furthermore numerically. However, we may note at once one of the important properties of this equation: in contrast to the solution to Eq. (1), its solution is continuous and unambiguous. Mathematically, this property is explained by the fact that Eq. (7) is linear with respect to the derivatives $Q_{\theta\theta}$ and Q_θ. The physical reason for the continuity and uniqueness of the profile for the jump $1 \to 0$ is the nonlinear relaxation. This relaxation damps the elastic nonlinearity of a microinhomogeneous medium in the HF region ($\omega \ll \Omega$) [4, 5]. This prevents an increase in the

wave front steepness and appearance of ambiguity of the profile $V = V(\theta)$, its maximal steepness being equal to $Q_{\theta\max} = \dfrac{\mu}{4(1-\mu)}$.

The results of numerically calculating profiles of steady-state waves for $W(\theta) = \dfrac{V(\theta)}{V_0}$ and for different values of the dimensionless parameter μ are plotted in Fig. 2. It follows from this figure and from the analysis of linearized equation (7) near the equilibrium states $Q_1 = 1$ and $Q_2 = 0$ that in the case of $\mu \le (3 - 2\sqrt{2})$, the wave profile represents the monotonous drop (the same as in a homogeneous medium [1]). In the case of $\mu > (3 - 2\sqrt{2})$, in the profile (near the equilibrium state $Q_1 = 1$), oscillations occur. Their amplitude and frequency increase with μ, whereas the front duration decreases.

We now consider the propagation of an initially harmonic wave ($V(x = 0, \tau) = V_0 \sin\omega\tau$) in such a medium. Assuming in Eq. (4) that

$$W(\vartheta, z) = \frac{V(\vartheta, z)}{V_0}, \quad \vartheta = \omega\tau, \quad z = \frac{\nu\gamma V_0 \omega x}{\zeta C^2},$$

$$D = \frac{C}{2\gamma V_0}, \quad d = \frac{\omega}{\Omega},$$

we arrive at

$$\frac{\partial W}{\partial z} + \frac{D}{d}\frac{\partial S}{\partial \vartheta} - \frac{1}{2d^3}\frac{\partial S[S^2]}{\partial \vartheta} = 0, \qquad (9)$$

where $S[W(\vartheta, z)] = \int\limits_{-\infty}^{\vartheta} W(\vartheta_1, z)\exp\left(-\dfrac{\vartheta - \vartheta_1}{\mu}\right)d\vartheta_1$.

In the low-frequency limit ($d \ll 1$), we have from (9), we obtain an equation similar to the Korteweg–de Vries–Bürgers equation [1]. The equation obtained differs from the latter one by a small nonlinear term $2d\dfrac{\partial^2 W^2}{\partial \vartheta'^2}\left(2d\left|\dfrac{\partial^2 W^2}{\partial \vartheta'^2}\right| \ll \left|W\dfrac{\partial W}{\partial \vartheta'}\right|\right)$:

$$\frac{\partial W}{\partial z} - W\frac{\partial W}{\partial \vartheta'} + 2d\frac{\partial^2 W^2}{\partial \vartheta'}$$

$$= dD\left[\frac{\partial^2 W}{\partial \vartheta'^2} - d\frac{\partial^3 W}{\partial \vartheta'^3}\right], \ \vartheta' = \vartheta - Dz. \qquad (10)$$

The solution to Eq. (10) (without the term $2d\dfrac{\partial^2 W^2}{\partial \vartheta'^2}$) was thoroughly studied in [1]. In particular, this solution describes the asymmetric distortion of a harmonic wave and formation of weak pulsations near its vertex.

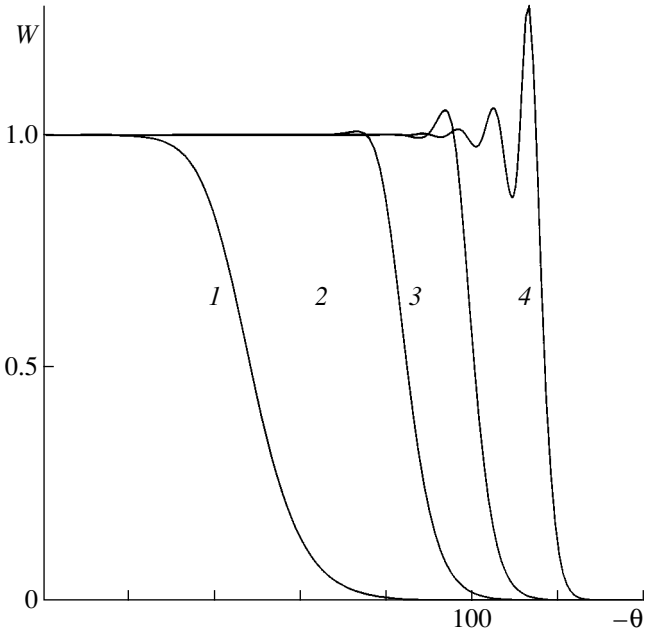

Fig. 2. Profiles of steady-state waves of the asymmetric-jump type in a microinhomogeneous medium for different values of the parameter μ: (*1*) $\mu = 0.15$; (*2*) 0.25; (*3*) 0.35; (*4*) 0.6.

Apparently, it should be expected that the existence of this term does not qualitatively change the general evolution pattern for the LF wave.

In the other (HF) limit when $d \gg 1$, we obtain from Eq. (9)

$$\frac{\partial^2 S}{\partial \vartheta \partial z} + \frac{1}{d}\frac{\partial S}{\partial z} + \frac{D}{d}\frac{\partial S}{\partial \vartheta} - \frac{S^2}{2d^3} = 0. \qquad (11)$$

As is seen from Eq. (11), in this case, the nonlinearity of the medium is strongly suppressed. Thus, the HF wave propagating at a velocity C undergoes only linear attenuation whose decrement is determined by the expression $\theta_0 = \dfrac{\nu\Omega}{4\pi\zeta\omega}$.

More detailed and exact pattern of evolution of harmonic waves (particularly for $\omega \approx \Omega$) can be obtained by numerically solving Eqs. (9)–(11).

The authors hope that the results of the performed study could be useful in the development of nonlinear acoustic (and seismoacoustic) methods of diagnostics of microinhomogeneous media. These media contain various viscous-elastic defects that have more complicated (compared to that analyzed in this study) distribution over parameters Ω and ζ and possess not only quadratic (or cubic) elastic nonlinearity but a nonlinearity

of another type (e.g., hysteresis, or dissipative nonlinearity). These nonlinear relaxation properties are intrinsic to many polycrystalline rocks and a few metals.

ACKNOWLEDGMENTS

The work was supported by the Russian Foundation for Basic Research, project nos. 01-05-64417, 02-02-16237; and 02-02-08021 INNO.

REFERENCES

1. O. V. Rudenko and S. I. Soluyan, *Theoretical Foundations of Nonlinear Acoustics* (Consultants Bureau, New York, 1977; Nauka, Moscow, 1975).
2. R. M. Davies, Appl. Mech. Rev. **6**, 1 (1953); *Stress Waves in Solids* (Inostrannaya Literatura, Moscow, 1961).
3. O. V. Rudenko and V. A. Robsman, Dokl. Akad. Nauk **384**, 755 (2002) [Dokl. Phys. **47**, 443 (2002)].
4. V. E. Nazarov, V. Yu. Zaitsev, and I. Yu. Beliaeva, Acoust. Lett. **22** (12), 236 (1999).
5. V. E. Nazarov, V. Yu. Zaitsev, and I. Yu. Beliaeva, Acust. Acta Acust. **88**, 40 (2002).
6. M. A. Isakovich, *General Acoustics* (Nauka, Moscow, 1973).

Translated by G. Merzon

Doklady Physics, Vol. 48, No. 11, 2003, pp. 637–639. Translated from Doklady Akademii Nauk, Vol. 393, No. 2, 2003, pp. 191–193.

TECHNICAL PHYSICS

Pulsed Radiation from a Coaxial Line into an Irregular Waveguide

V. I. Koroza and M. N. Golikov*

Presented by Academician V.N. Mikhaĭlov April 17, 2003

Received April 25, 2003

Pulses of transverse electromagnetic waves (TEM) propagating from coaxial lines, where they are formed, to irregular waveguides with simply connected sections are transformed into pulses with the structure of longitudinal waves (TM waves). These processes determine the operation efficiency of certain devices such as pulsed radiation antennas. The fast development of equipment for ultrawideband electromagnetic pulses [1, 2] has recently increased the interest in these processes. Nevertheless, they remain poorly studied due primarily to difficulties in the mathematical simulation of pulsed operation modes for irregular channels. These difficulties are aggravated by the presence of topologically discontinuous connections between transmission lines with doubly connected sections and waveguides with simply connected sections. As is shown in this study, the corresponding generalization of the model of connected strings for irregular waveguides with a conserved topology of sections [3, 4] makes it possible to perform such calculations with a high level of accuracy.

Figure 1 exemplifies such a channel with Z-axial symmetry. The boundaries $r = a(z)$ and $r = b(z)$ of the inner and outer ideal conductors, respectively, as well as the characteristics (ε and μ) of the medium, are assumed to be independent of the azimuth angle φ. The boundaries are chosen in the form of cylinders $a(z) = a_0 = \text{const}$ and $b(z) = b_0 = \text{const}$ for $z \le 0$ (regularity region) that are transformed to the ellipsoid of revolution

$$a(z) = a_0\left(1 - \frac{z^2}{a^{*2}}\right)^{1/2}$$

and to the one-sheeted hyperboloid of revolution

$$b(z) = b_0\left(1 + \frac{z^2}{b^{*2}}\right)^{1/2},$$

respectively, for $z > 0$.

The set of time-dependent waveguide equations has the matrix form [3, Eq. (7)]

$$\frac{\partial}{\partial z}\left[G(z)\frac{\partial \mathbf{f}}{\partial z} + Q(z)\mathbf{f}\right] - Q^{\tau}(z)\frac{\partial \mathbf{f}}{\partial z} - P(z)\mathbf{f} - T(z)\frac{\partial^2 \mathbf{f}}{\partial t^2} = 0, \quad (1)$$

where the z coordinate and time t are independent variables. The components $f_j(z, t)$ of the unknown column vector $\mathbf{f}(z, t)$ are the amplitudes of the reference-waveguide modes in the expansion of the azimuthal magnetic-field component, which is the only nonzero component in the case under consideration:

$$H(\mathbf{r}_\perp, z, t) = \sum e_j(\mathbf{r}_\perp, z) f_j(z, t). \quad (2)$$

The dimensions $[N]$ of the column vector $\mathbf{f}(z, t)$ and of the $[N \times N]$ square matrix functions $\mathbf{G}(z)$ and $\mathbf{Q}(z)$, together with the transposed matrix functions $\mathbf{Q}^{\tau}(z)$, $\mathbf{P}(z)$, and $\mathbf{T}(z)$ in set (1), are determined by the number N of the terms taken into account in sum (2). These matrix

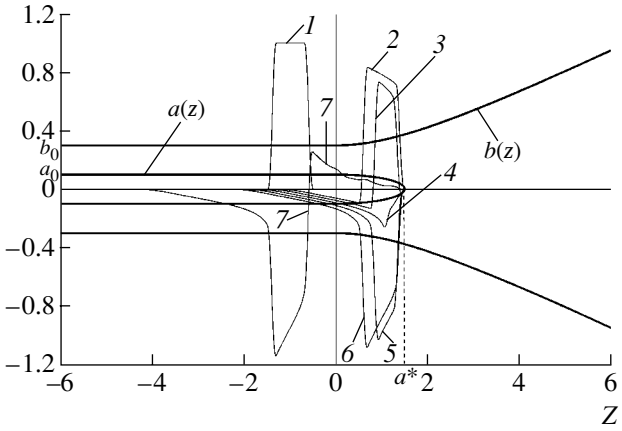

Fig. 1.

Institute of Strategic Stability, Moscow, Russia
** e-mail: iss@niiit.ru*

1028-3358/03/4811-0637$24.00

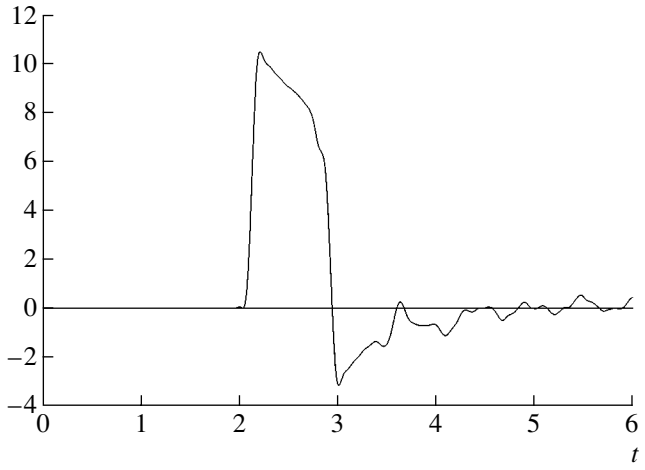

Fig. 2.

functions are given by their matrix elements

$$G_{ns}(z) = \int\limits_{S(z)}\int \varepsilon^{-1} e_s e_n dS, \quad T_{ns}(z) = \int\limits_{S(z)}\int \mu e_s e_n dS,$$

$$Q_{ns}(z) = \int\limits_{S(z)}\int \varepsilon^{-1} (e_s)_z e_n dS, \tag{3}$$

$$P_{ns}(z) = \int\limits_{S(z)}\int \varepsilon^{-1}\{(e_s)_z (e_n)_z + r^{-2}(re_s)_r (re_n)_r\} dS,$$

where $S(z)$ are the plane sections of the channel that are orthogonal to the Z axis and the subscripts z and r stand for the differentiation with respect to these variables.

In what follows, dimensionless variables and parameters will be used. The dimensionless variables are obtained by dividing all quantities that have a dimension of length (space coordinates, functions $a(z)$ and $b(z)$, etc.) by a certain convenient linear scale L, while time t is divided by $\frac{L}{c}$ (c is the speed of light in vacuum). The dimensionless values are denoted by the same symbols. In this case, $c = 1$.

The field distribution functions in the corresponding reference waveguides are used as a set $\{e_j(\mathbf{r}_\perp, z)\}$ in expansion (2).

(i) For doubly connected $S(z)$ in the range $z < a^*$, we take

$$e_1 = \frac{1}{r}; \quad e_{k+1} = N_0(\lambda x_k) J_1\left(x_k \frac{r}{a}\right)$$

$$- J_0(\lambda x_k) N_1\left(x_k \frac{r}{a}\right), \quad k = 1, 2, \ldots. \tag{4}$$

Here, $\lambda = \frac{b}{a}$; and x_k ($0 < x_1 < x_2 < x_3 < \ldots$) are the roots of the equation

$$N_0(\lambda x_k) J_0(x_k) - J_0(\lambda x_k) N_0(x_k) = 0.$$

Since $\lambda = \lambda(z)$, $x_k = x_k(z)$. In this case, the amplitude $f_1(z, t)$ corresponds to the magnetic field of the TEM mode, whereas the remaining amplitudes $f_{k+1}(z, t)$ ($k \geq 1$) correspond to the magnetic fields of the TM_{0k} modes (E-type waves).

(ii) For $z > a^*$, when $S(z)$ are simply connected, to provide the continuity of the functions in the set $\{e_j(\mathbf{r}_\perp, z)\}$ with identical numbers j on either side of the section $S(a^*)$, we supplement the basis set $\{e_j(\mathbf{r}_\perp, z)\}$ with the surplus function $e_1 = \frac{1}{r}$ and simultaneously set $f_1(z, t)$ to zero. As a result, we have

$$e_1 = \frac{1}{r}; \quad e_{k+1} = N_0(\nu_k) J_1\left(\nu_k \frac{r}{b}\right), \quad k = 1, 2, \ldots. \tag{5}$$

Here, ν_k are the roots of the equation $J_0(\nu_k) = 0$ ($0 < \nu_1 < \nu_2 < \nu_3 < \ldots$). The normalization coefficients $N_0(\nu_k)$ are involved in (5) to provide the continuity of the set $\{e_j(\mathbf{r}_\perp, z)\}$ for $z = a^*$. We emphasize that TE_{0j} modes (H-type waves) are assumed to be absent for $t = 0$; they also do not arise for $t > 0$ and, therefore, are ignored here.

Set (1) for the pulse with the TEM initial ($t = 0$) structure (Fig. 1, trapezoidal curve *1* with the base in the range $-1.5 \leq z \leq -0.5$, top in the range $-1.3 \leq z \leq -0.7$, and smoothed lateral sides against the background of the channel configuration) was numerically solved by using an explicit finite difference scheme with mesh sizes of $hz = 0.01$ and $ht = 0.002$. In this case, solutions to set (1) were joined at $z = a^*$ in correspondence with the continuity conditions for the transverse components of magnetic and electric fields. For specific calculations, we took $a_0 = 0.1$, $a^* = 1.5$, $b_0 = 0.3$, $b^* = 2$, $\varepsilon = \mu = 1$, and $N = 7$. In addition, Fig. 1 shows the calculations of the magnetic field for the TEM component of the pulse [function $f_1(z, t)$] in the times: $t =$ (*2*) 2; (*3*) 2.25; (*4*) 2.5; (*5*) 2.75; (*6*) 3; and (*7*) 5.

The curves show the characteristic behavior features for the magnetic-field TEM component of the pulse near the $S(a^*)$ section. First, the width of the pulse decreases (curves *2* and *3*), because the trailing edge approaches the leading edge that stops when it achieves the $S(a^*)$ section and cannot overcome it. Then, the magnetic-field pulse changes polarity (curve *4*); i.e., the propagation direction changes. Finally, the pulse width is restored (curves *5*–*7*).

In the time interval $2 < t < 3$, the transformation of transverse waves into TM-type longitudinal waves is intensified simultaneously with the formation of the reflected pulse. This can be directly seen in Fig. 2 show-

ing the time dependence of the electric field directed along the *Z* axis at this point.

The calculation error was estimated from the relative spread of the total electromagnetic energy accumulated in the pulse and calculated when solving set (1). This value was no more than 0.1% for various times *t*.

Thus, we showed that the fast qualitative reorganization of ultrawideband short electromagnetic pulses passing through the topologically discontinuous connections of coaxial-type waveguides and irregular waveguides with simply connected sections can be efficiently simulated and calculated with a high accuracy. The structure of pulses, which are initially transverse waves and are partially reflected as well as transformed into forward-propagating longitudinal waves, changes in the vicinity of the topologically discontinuous sections during the short time that pulses pass through.

REFERENCES

1. *Ultra-Wideband, Short-Pulse Electromagnetics 3*, Ed. by C. E. Baum, L. Carin, and A. P. Stone (Plenum, New York, 1997).

2. *Ultra-Wideband, Short-Pulse Electromagnetics 4*, Ed. by E. Heyman, B. Mandelbaum, and J. Shiloh (Kluwer, New York, 1999).

3. V. I. Koroza, Pis'ma Zh. Tekh. Fiz. **22** (21), 6 (1996) [Tech. Phys. Lett. **22**, 865 (1996)].

4. M. N. Golikov, V. I. Koroza, and V. N. Mikhailov, Dokl. Akad. Nauk **385**, 51 (2002) [Dokl. Phys. **47**, 504 (2002)].

Translated by V. Bukhanov

Doklady Physics, Vol. 48, No. 11, 2003, pp. 640–643. Translated from Doklady Akademii Nauk, Vol. 393, No. 3, 2003, pp. 336–340.

TECHNICAL PHYSICS

Criterion of the Appearance of Diamond-Shaped Pores in Dispersely Filled Polymers

S. L. Bazhenov, O. A. Serenko, I. L. Dubnikova, and Academician A. A. Berlin

Received July 8, 2003

Introduction of a small fraction of large particles often embrittles a polymer, and the rupture of the polymer occurs at small relative elongation. The sharp loss of the deformability of the composite is caused by the appearance of so-called diamond-shaped pores [1] observed previously in [2, 3]. It was shown that the size of particles responsible for the appearance of diamond-shaped pores is determined by the critical crack opening and, therefore, by the breakdown viscosity of the matrix polymer.

Rupture of particles or their separation from the matrix under tension gives rise to the formation of pores whose shape is determined by the size of particles [1]. Small and large particles form oval pores and diamond-shaped pores, respectively. With further tension, the two types of pores that appear behave differently. An oval pore develops only along the material-elongation direction. A diamond-shaped pore grows in three directions, parallel and perpendicular to the sample tension axis, in particular, along the sample thickness, which leads to early failure. In polymers deformed by the propagation of a neck, the problem is compounded, because the growth of pores is often localized in the narrow formed neck. As a result, the material breaks down at small macroscopic strain. Although the fracture process (growth of diamond-shaped pores) is typically plastic at the mesoscale, the material behaves as a brittle material at the macroscale. This work aims to determine the dependence of the critical size of particles at which diamond-shaped cracks appear on the properties of the polymer matrix.

Lukoten F 3802 medium-density polyethylene, Lipol A4-70 polypropylene, and 168030-070 low-density polyethylene are used for composites. Polymers were filled with powdered-rubber particles with sizes from 50 to 600 μm. A monodisperse filler was obtained by grading the polymers into grain sizes with a standard set of sieves. Each polymer was mixed with rubber particles in a single-screw laboratory extruder. The filler concentration was equal to 1–2 vol %. Plates with a thickness of 2 mm were pressed from obtained mixtures.

In addition, isotactic polypropylene with $M_v = 6.3 \times 10^5 \left(\frac{M_v}{M_n} = 3.5\right)$ was mixed with monodisperse $Al(OH)_3$ particles with sizes 8, 25, and 55 μm in a Brabender mixer. The conditions of the production of the mixture and its pressing were presented in [4]. The filler concentration was equal to 5 vol %.

Pure-polymer 0.5-mm-thick films were pressed in the same regime as mixtures. Unfilled isotactic polypropylene was treated in the Brabender mixer in the regime of composite formation and was then pressed.

Specimens in the form of double-sided blades with 5×35-mm working parts were cut out of the plates. Mechanical tests of composites were carried out on a Shimadzu Autograph AGS—10kNG universal testing machine with a tension rate of 20 mm/min. The surface of broken specimens was analyzed by both a Hitachi S-520 scanning electron microscope and a $Q \times 3$ optical microscope. The particle sizes in the composite were estimated when analyzing the material by a microscope.

Specimens with a notch were tested on a testing minidevice, where a specimen is stretched with a rate of 2 mm/min in the field of vision of the $Q \times 3$ optical microscope. The specimen was periodically photographed in the tension process. The notch was made by a blade. The length of the crack was equal to 0.8–1 mm.

Figure 1 shows a diamond-shaped pore that appears in the neck region due to the breakdown of a large particle under the tension of a filled polymer. The tension direction is indicated by the arrow. The pore is strongly elongated along the tension direction, and its length reaches 1.5 mm. The sides of the diamond-shaped pore are curved. The pore opening angles are equal to 25°–30° and 140°–160°. Small remainders of the rubber particles, whose main mass is often separated and rejected from the pore, are seen in acute angles. Analysis of the pore with large magnification shows that the pore is much shallower near two acute angles than at

Institute of Synthetic Polymeric Materials, Russian Academy of Sciences, ul. Profsoyuznaya 70, Moscow, 117393 Russia

1028-3358/03/4811-0640$24.00

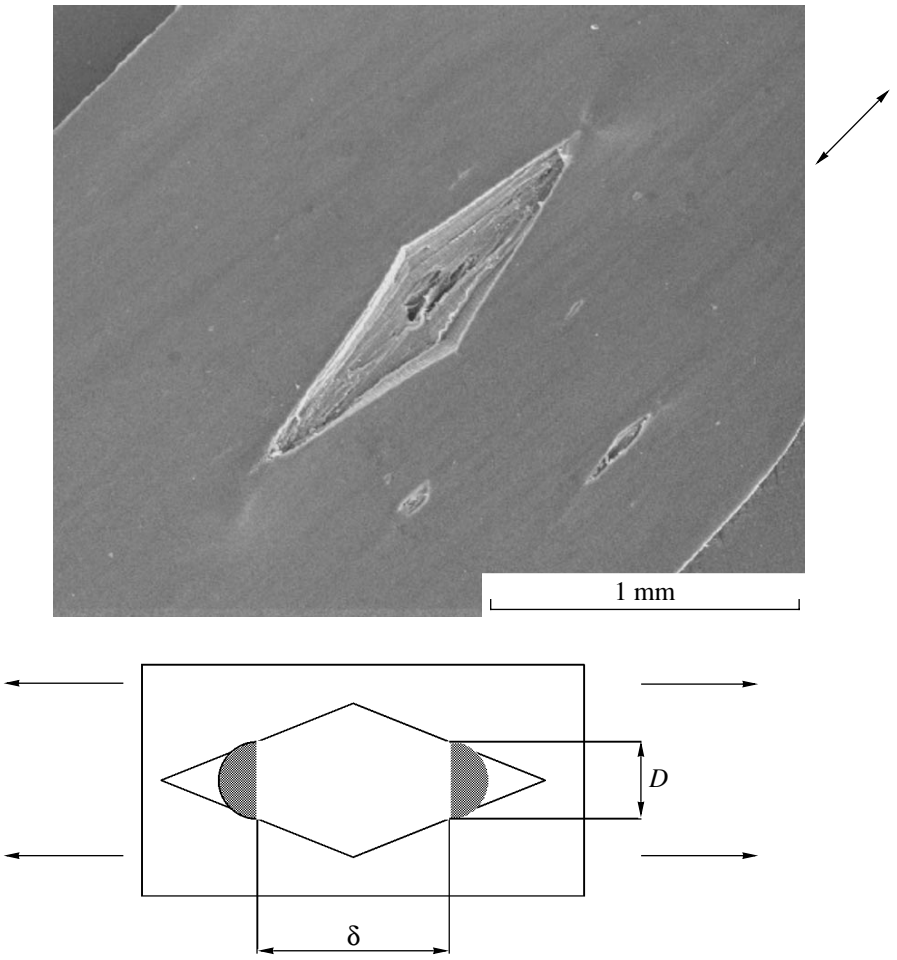

Fig. 1. (Upper) Image of a diamond-shaped pore in a medium-density polyethylene with 2 vol % rubber particles as obtained by a scanning electron microscope and (lower) scheme of the pore.

the center. Therefore, the pore grows not only in the width (perpendicularly to the arrow shown in Fig. 1) but also in the depth (thickness) of the specimen. Moreover, with larger magnification, traces of tearing apart of polyethylene are seen on the line joining two neighboring vertices of the pore, which indicates that the pore grows in depth. Several oval pores are also observed in the neighborhood. Figure 2 shows the typical form of an oval pore. This pore is much smaller than the diamond-shaped pore and has a length of about 100 μm. Remainders of the destroyed particle pressed out of the matrix are seen at the vertices of the pore.

The table presents the minimum size of filler particles near which diamond-shaped pores are formed. The critical size of a particle depends on the type of matrix polymer.

Pores that are formed under the rupture of large particles grow microcracks. Half of the diamond-shaped pore is similar to the tip of a notch in the unfilled polymer [5]. Optical microphotographs shown in Fig. 3 demonstrate the development of a crack under the tension of unfilled medium-density polyethylene. For small strains of the specimen, the crack edge becomes smooth, and its tip has a round shape similar to the shape of the oval pore (Fig. 3a). Further tension leads to a gradual opening of the crack. At a certain time, the geometry of the crack tip changes from round to wedge, and the crack begins to grow. Further opening of the crack gives rise to an increase in the size of the wedge,

Minimum size of particles near which diamond-shaped pores are formed and critical crack opening in 168030-070 low-density polyethylene (LDPE), Lukoten F 3802 medium-density polyethylene (MDPE), Lipol A4-70 polypropylene (PP1), and isotactic polypropylene (PP2)

Polymer	Filler	Minimum size of particles, μm	Critical crack opening, μm
LDPE	Rubber	400	1150
MDPE	Rubber	100	680
PP1	Rubber	80	550
PP2	$Al(OH)_3$	25	143

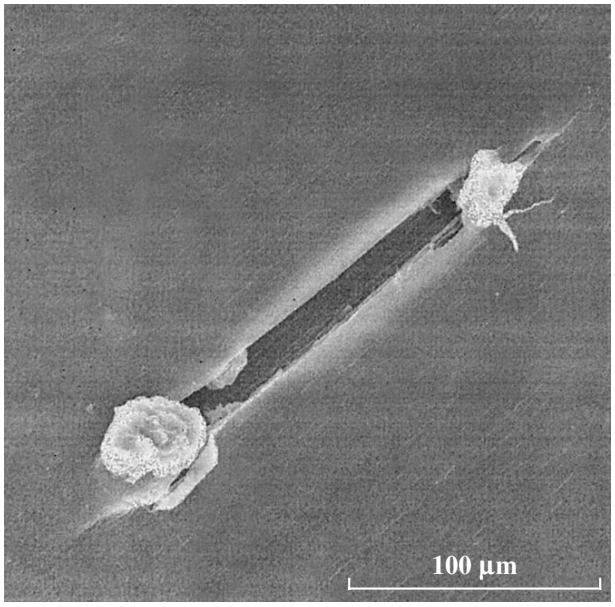

Fig. 2. Same as in the upper panel of Fig. 1, but for an oval pore.

whose angle remains unchanged. In this case, the tip of the crack is similar to half the diamond-shaped pore whose angle is virtually equal to the angle of the tip of the crack (Fig. 1 and right panel in Fig. 3). A similar behavior was observed in all polymers under investigation with both hard inorganic and elastic fillers.

The table presents the critical opening of the crack for which the formation of an edge begins at the tip of the crack for various polymers. The critical size of particles near which diamond-shaped pores are formed correlates with the critical opening of the crack δ_c. The critical size of filler particles near which diamond-shaped pores are formed increases with the critical opening of the crack δ_c.

Breakdown of a filler particle leads to the appearance of a pore. Rubber particles usually break down, but they can also be separated from the matrix. Particles of the mineral filler did not break down, and pores were formed through the separation of filler particles. According to linear fracture mechanics, a crack begins to grow when its opening at the tip reaches the critical value δ_c which is independent of the crack length [5, 6]. Knowing the critical size of filler particles for which diamond-shaped pores appear, one can determine the critical opening of a pore for which the development of the pore as a crack begins.

We consider a spherical particle with diameter D. Stress in the filler due to its breakdown is ignored. The opening of a formed pore along the tension axis is equal to the distance between the fragments of the particle (Fig. 1), i.e.,

$$\delta = (\lambda - 1)D, \tag{1}$$

where λ is the elongation degree of the matrix polymer.

We assume that pores behave as microcracks; i.e., the formation of a diamond-shaped pore from an oval pore begins when the opening of the latter pore δ reaches the critical opening of the crack δ_c. In other words, the equality $\delta = \delta_c$ is a criterion of the beginning of the growth of the micropore transversely to the elongation direction (formation of the diamond-shaped

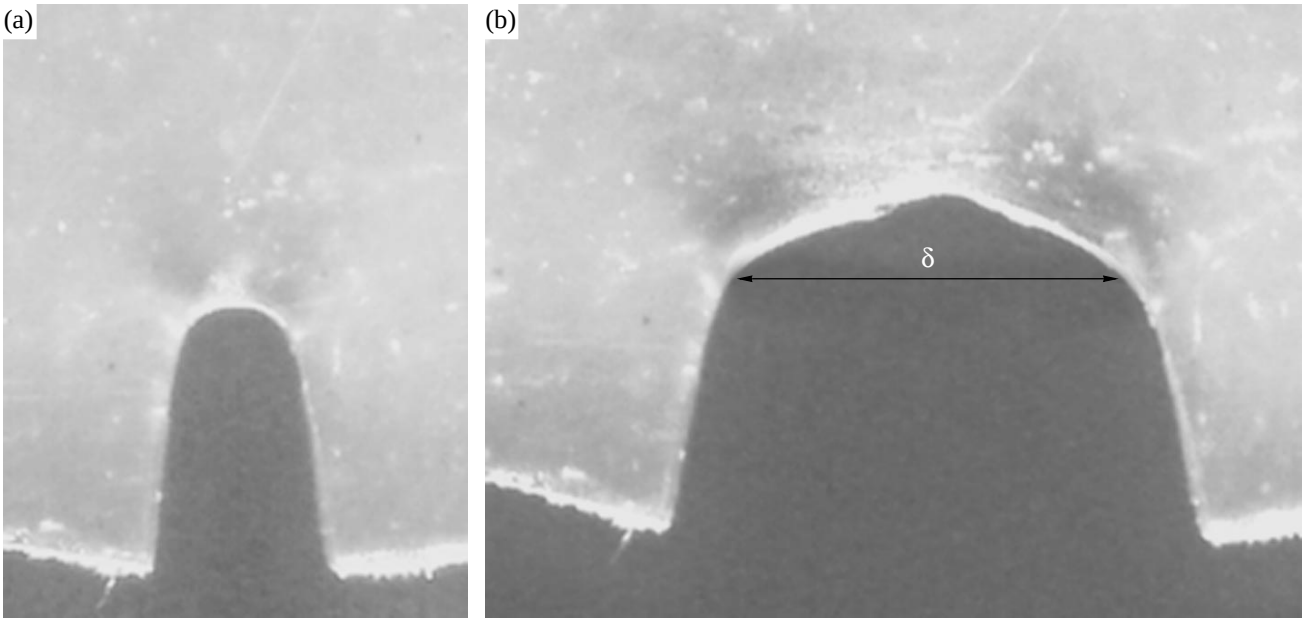

Fig. 3. Development of a notch in a medium-density polyethylene: (a) oval geometry of the crack tip and (b) edge formation.

pore). In this case, the critical size of particles is determined as

$$D_c = \frac{\delta_c}{\lambda - 1}. \quad (2)$$

In this work, we studied only composites based on polymers deformed with the formation of a neck, where λ is equal to the natural elongation degree of the matrix polymer λ_d. The appearance of diamond-shaped pores was observed both in the process of the propagation of the neck and at the reinforcement stage, when λ exceeds λ_d. However, data presented below refer only to the neck region. Figure 4 shows a correlation between the quantity $\frac{\delta_c}{\lambda_d - 1}$ and the experimentally determined critical sizes of particles whose breakdown (separation) is accompanied by the formation of diamond-shaped pores. The dependence can be approximated by a straight line whose slope is close to unity. This means that the transition of oval pores to diamond-shaped pores is really caused by the achievement of the critical opening δ_c. The behaviors of composites filled with the hard mineral filler and rubber particles are similar to each other. We emphasize that δ_c characterizes the material cracking resistance, which is described by one of three parameters: breakdown viscosity G_{Ic}, critical intensity coefficient K_{Ic}, or δ_c. Thus, the critical size of particles in the filled composite is determined by the cracking resistance of the matrix polymer.

Using the well-known relation between the breakdown viscosity G_{Ic} and critical opening of a crack $G_{Ic} \approx \sigma_y \delta_c$ [6], where σ_y is the yield stress of the matrix polymer, we represent Eq. (2) in the form

$$D_c = \frac{G_{Ic}}{\sigma_y(\lambda - 1)}. \quad (3)$$

This formula can be written in the form

$$\lambda = \frac{G_{Ic}}{\sigma_y D} + 1, \quad (4)$$

which describes the elongation degree for which diamond-shaped pores are formed as a function of the size of particles.

The above experimental data are given only for polymers deformed by neck propagation. However, they are probably general and are similar for materials deformed through uniform plastic flow. Thus, the breakdown or separation of large particles is responsible for the appearance of defects that first grow as oval pores under tension and then are transformed to diamond-shaped pores. The latter pores are microcracks growing transversely to the tension direction. A diamond-shaped pore is formed when the opening (elongation) of the pore reaches the critical opening of a crack in the unfilled polymer with a notch. The size of particles for which diamond-shaped pores appear is limited by the breakdown viscosity of the matrix polymer. A filler particle can be called large if its size is close to or larger than D_c.

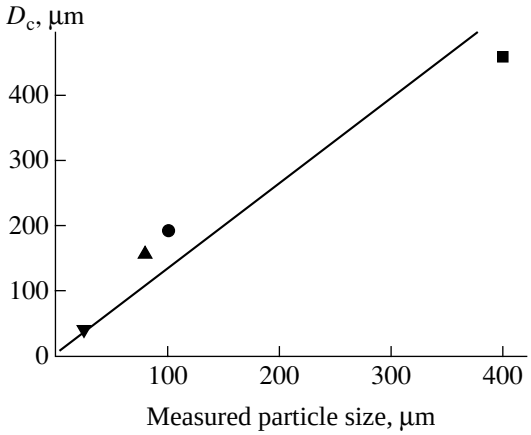

Fig. 4. Calculated vs. measured critical sizes of particles in (■) 168030-070 low-density polyethylene, (●) Lukoten F 3802 medium-density polyethylene, (▲) Lipol A4-70 polypropylene, and (▼) isotactic polypropylene (PP2).

ACKNOWLEDGMENTS

This work was supported by the Russian Foundation for Basic Research (project no. 03-03-32259) and by the Division of Chemistry and Material Sciences, Russian Academy of Sciences (State contract no. 10002-251/OKhNM-03/128-126/250603-843).

REFERENCES

1. O. A. Serenko, I. N. Nasrullaev, and S. L. Bazhenov, Vysokomol. Soedin., Ser. A **45** (5), 759 (2003).
2. I. Narisawa, *Strength of Polymers* (Khimiya, Moscow, 1987), translated from Japanese.
3. J. X. Li, M. V. Twigg, A. Hiltner, and E. Baer, J. Appl. Polym. Sci. **52**, 285 (1997).
4. I. L. Dubnikova, V. G. Oshmyan, and A. Ya. Gorenberg, J. Mater. Sci. **32**, 1613 (1997).
5. S. Bazhenov, J. Mater. Sci. **32**, 797 (1997).
6. V. Z. Parton and E. M. Morozov, *Mechanisms of Elastoplastic Fracture* (Nauka, Moscow, 1985).

Translated by R. Tyapaev

Doklady Physics, Vol. 48, No. 11, 2003, pp. 644–648. Translated from Doklady Akademii Nauk, Vol. 393, No. 1, 2003, pp. 42–46.

MECHANICS

Quasilinear Self-Excited Oscillations of a Helmholtz Resonator

L. D. Akulenko* and S. V. Nesterov

Presented by Academician V.F. Zhuravlev June 16, 2003

Received June 18, 2003

The thermal gas-dynamic model of self-excited oscillations of a Helmholtz resonator is analyzed. We introduce dimensionless variables and parameters that provide an adequate description of periodic motions by a third-order quasilinear system. The conditions of existence, uniqueness, and stability of the limiting cycles are ascertained. By the methods of local integral manifolds, averaging, and the Lyapunov–Poincaré method, a first-approximation solution is constructed and basic qualitative and quantitative characteristics of self-excited oscillations of the Helmholtz resonator are established. This thermal–mechanical system has not yet been satisfactorily studied.

1. The Helmholtz resonator was used as a simple acoustic device for both the efficient determination of the frequencies of acoustic oscillations and their absorption [1]. At present, devices and coatings based on the properties of the resonator are widely used in both architecture and technical acoustics [2]. The Helmholtz resonator includes a closed vessel that has volume V and a hole with area S. The hole is tightly connected with a tube open at both ends. This tube has length l and an inner cross section corresponding to the hole. The vessel and tube is filled with a gas, e.g., air. It was shown [1] that, under certain conditions, this device is a lumped linear oscillatory system, where the gas column in the tube and the gas in the vessel characterize lag and elasticity, respectively. The frequency ω_0 of small free oscillations disregarding dissipation is equal to

$$\omega_0 = c_0\sqrt{\frac{S}{lV}}, \quad c_0^2 = \gamma\frac{P_0}{\rho_0}, \tag{1}$$

where c_0 is the speed of sound in the gas, γ is the adiabatic index, P_0 is the pressure, and ρ_0 is the gas density. According to Eq. (1), the frequency ω_0 is independent of the shapes of the vessel V and hole S. For conventional atmospheric conditions and $V \sim 10^2$ cm^3, $S \sim 1$ cm^2, and $l \approx 10$ cm, we have $\omega_0 \sim 10^3$ s^{-1}, i.e., $\frac{\omega_0}{2\pi} \sim 10^2$ Hz, which corresponds to the frequency of audible acoustic oscillations for $c_0 = 3.4 \times 10^4$ cm s^{-1}.

Free oscillations of the gas in the resonator tube rapidly damp due to dissipation. However, by heating the gas in the vessel, one can realize positive feedback and sustain oscillations of the gas column for a long time, i.e., realize self-excited oscillations of the thermal gas-dynamic system with the frequency ω close to ω_0 given by Eq. (1). This mechanism and simple mathematical model were proposed by Teodorchik [3]. He emphasized that similar thermomechanical oscillations were often observed both in technical devices and in nature: acoustic oscillations of air in tubes under glass-blowing operations, "singing" of vapor in long pores of a thick layer of deposits before liquid boiling, self-excited oscillations of a gas in boiler tubes, geysers as an oscillation geothermal phenomenon, Cepheid variable stars as an astrophysical phenomenon, etc.

A simplified model provides not only qualitative but also satisfactorily quantitative determination of the conditions of appearance and basic characteristics of self-excited oscillations for various parameters of the thermomechanical system. Following [3], we represent the relations describing the dynamics of the system. A substantial condition is that the steady-state temperature T_x of the resonator walls has significant gradient near the point $x = 0$ of the connection between the vessel and tube. The x dependence of T_x is usually approximated as [3]

$$T_x = T_0 + k_1 x - k_3 x^3, \quad |x| \le d \ll l, \tag{2}$$

where $k_{1,3} > 0$ are constants and T_0 is the average temperature for $x = 0$.

Further, the thermal balance condition

$$mc\dot{\theta} = K(k_1 x - k_3 x^3 - \theta), \quad T = T_0 + \theta \tag{3}$$

is applied to the gas element with mass m, which is in interval (2) near $x = 0$. Here, T is the current tempera-

Institute for Problems in Mechanics,
Russian Academy of Sciences,
pr. Vernadskogo 101-1, Moscow, 119526 Russia
** e-mail: kumak@ipmnet.ru*

1028-3358/03/4811-0644$24.00

ture, θ is the deviation from the average temperature T_0, c is the heat capacity at a constant gas volume, and K is the thermal conductivity.

Under the assumption that the displacement x of a gas column with the mass $m_0 = \rho_0 S l$ in the tube is small, the equation of motion (after division by m_0) has the form

$$\ddot{x} + 2\delta\dot{x} + \omega_0^2 x + \beta\theta = 0, \quad |x| \le d \ll l \tag{4}$$

in the approximation of linear dissipation and thermal expansion. Here, 2δ is the dissipation coefficient and β is the coefficient of thermal expansion relating the thermal variable θ to mechanical variables x and $\dot{x}$. We note that the point $\theta = x = \dot{x} = 0$ is the steady state of the set of Eqs. (3) and (4), which is further analyzed by asymptotic methods. It is of interest to analyze both the stability conditions for the rest point and the possibility of self-excited oscillations of the Helmholtz resonator in the quasilinear model. There are attempts of analytical analysis of the system. However, a satisfactory solution to the problem of undamped periodic motion is absent. In this work, self-excited regimes are constructed and analyzed for various resonator parameters under the assumption that the dimensionless coefficients of self-excitation and dissipation are small.

2. The dimensional set of Eqs. (3) and (4) involves four variables θ, x, $\dot{x}$, and t and eight parameters ω_0, δ, β, m, c, K, k_1, and k_3 in certain combinations. To obtain completely dimensionless equations, it is convenient to remove the variable θ, which has no mechanical meaning, and pass to the third-order equation in the variable x. This operation is performed through, first, the differentiation of Eq. (4) with respect to t and, second, the expression of θ and $\dot{\theta}$ in terms of x, $\dot{x}$, and $\ddot{x}$. Then, the resulting equation reduces to the third-order equation involving only three dimensionless parameters ε, κ, and σ:

$$\dddot{\xi} + (\kappa + \varepsilon\sigma)\ddot{\xi} + (1 + \varepsilon\sigma\kappa)\dot{\xi} + (\kappa + \varepsilon)\xi - \varepsilon\xi^3 = 0,$$

$$\tau = \omega_0 t, \quad \xi = \frac{x}{d}, \quad d^2 = \frac{k_1}{k_3}, \quad \kappa = \frac{K}{mc\omega_0}, \quad \kappa \sim 1, \tag{5}$$

$$\varepsilon = \frac{\kappa\beta k_1}{\omega_0^2}, \quad \varepsilon \ll 1, \quad \varepsilon\sigma = \frac{2\delta}{\omega_0}.$$

Here, the dot represents the derivative with respect to the dimensionless variable τ and the length unit d is the interval characterizing the temperature gradient according to Eq. (2). The dimensionless quantity ε is considered as a small parameter in the problem of oscillations of the quasilinear system specified by Eqs. (5), which has the rest state $\xi = \dot{\xi} = \ddot{\xi} = 0$. We analyze the Lyapunov stability of this solution. According to the Routh–Hurwitz criterion, the conditions of asymptotic stability have the form

$$\kappa + \varepsilon\sigma > 0, \quad \varepsilon\sigma(1 + \kappa^2 + \varepsilon\sigma\kappa) - \varepsilon > 0, \quad \kappa + \varepsilon > 0. \tag{6}$$

The first and third conditions are automatically satisfied. The second inequality is a relation implied on the parameters of the system after the transition to dimensional variables according to Eq. (5). According to conditions (6), this relation can be violated if the dissipation coefficient σ is quite small, in particular, for $\sigma \sim \varepsilon \ll 1$. In this case, the inverse inequality is satisfied, and the rest point is exponentially unstable. Indeed, the roots of the characteristic linearized equation (5) for quite small $\varepsilon > 0$ are represented as

$$\lambda = \lambda_{1,2,3}(\varepsilon), \quad \lambda(\varepsilon) = \lambda^0 + \varepsilon\lambda^1 + \varepsilon^2\ldots,$$

$$\lambda^0_{1,2} = \pm i, \quad \lambda^1_{1,2} = \pm\frac{i}{2}\frac{\kappa}{1+\kappa^2} + \frac{1}{2}\left(\frac{1}{1+\kappa^2} - \sigma\right), \tag{7}$$

$$\lambda^0_3 = -\kappa, \quad \lambda^1_3 = -\frac{1}{1+\kappa^2}, \quad i = \sqrt{-1}.$$

For $\sigma \le (1 + \kappa^2)^{-1}$, the real parts of the complex conjugate roots $\lambda_{1,2}$ (7) are positive, which corresponds to the violation of the second of conditions (6) for small ε. Thus, indicated σ values are of interest for analysis of motion of the system near the stationary point, as well as for determination of the possibility of self-excited oscillations and Lyapunov stability.

The problem of existence and approximate construction of the stationary periodic motions (self-excited oscillations) can be solved by the Lyapunov–Poincaré method. Their stability is analyzed by the Andronov–Witt theorem [5]. However, this approach is very cumbersome. Moreover, the behavior of the system near the periodic motion is of applied interest. These investigations require effective asymptotic methods of nonlinear mechanics such as the method of local integral manifolds [6, 7] and averaging [8, 9]. To apply these methods, it is necessary to reduce Eq. (5) to the standard system by changing the variables ξ, $\dot{\xi}$, and $\ddot{\xi}$ to the variables a, ψ, z:

$$\xi = a\sin\psi + z, \quad \dot{\xi} = a\cos\psi - \kappa z, \quad \ddot{\xi} = -a\sin\psi + \kappa^2 z. \tag{8}$$

Here, a is the amplitude, ψ is the phase, and z is the variable determining the asymptotically stable local

integral manifold. In view of Eq. (5), the differentiation of Eqs. (8) provides the standard system [6, 7]

$$\dot{a} = \varepsilon A(a, \psi, z), \quad A \equiv (\kappa\cos\psi - \sin\psi) f, \quad a > 0,$$

$$\dot{\psi} = 1 + \varepsilon\Psi(a, \psi, z), \quad \Psi \equiv -a^{-1}(\kappa\sin\psi + \cos\psi) f,$$
$$\dot{z} + \kappa z = \varepsilon Z(a, \psi, z), \tag{9}$$

$$Z \equiv f = (1 + \kappa^2)^{-1}(\xi^3 - \xi - \sigma\kappa\dot{\xi} - \sigma\ddot{\xi}).$$

Expressions (8) for ξ, $\dot{\xi}$, and $\ddot{\xi}$ are substituted into the function f. The right-hand side is a 2π periodic function of ψ. For $\varepsilon = 0$, the general solution of system (9) is easily constructed. The periodic solution for ξ corresponds to $z \equiv 0$.

3. Estimating the solution of set (9), one can show that, after a relatively short time interval

$$\Delta\tau \approx \kappa^{-1}\ln(|z^0|\varepsilon^{-1}) \ll \varepsilon^{-1}, \quad z(0) = z^0, \tag{10}$$

motion is bounded in the ε vicinity of $z = 0$. It was found [6, 7] that, for $\tau > \Delta\tau$, the system moves in the ε vicinity of the stable local integral manifold

$$z = \varepsilon h(a, \psi, \varepsilon), \qquad h(a, \psi + 2\pi, \varepsilon) \equiv h(a, \psi, \varepsilon). \tag{11}$$

The unknown function h is determined as the solution of the partial differential equation

$$h'_\psi + \kappa h = H(a, \psi, \varepsilon[h]), \quad H \equiv Z - \varepsilon h'_\psi\Psi - \varepsilon h'_a A,$$
$$|h| \le h_0, \quad 0 < a^- \le a \le a^+ < \infty, \quad |\varepsilon| \le \varepsilon_0, \tag{12}$$

which is 2π periodic with respect to ψ. Since Eq. (12) is an analytic function of h, ε, and a, the desired function h can be constructed by the recurrence procedure

$$h^*_{(j+1)}(a, \psi, \varepsilon)$$
$$= \int_{-\infty}^{\psi} \exp[-(\psi - \varphi)]H(a, \varphi, \varepsilon[h_{(j)}])d\varphi, \tag{13}$$
$$h^*_{(1)}(a, \psi)$$
$$= \int_{-\infty}^{\psi} \exp[-(\psi - \varphi)]Z(a, \varphi, 0)d\varphi, \quad j = 1, 2, \ldots$$

with a given accuracy for sufficiently small ε_0. The function $h^*_{(j)}$ can be represented at each step of the procedure not only in operator form (13) but also in the form of a trigonometric polynomial of order $N = N(j)$. Since the function $h^*_{(j)}$ is representable as a power series of ε, expression (13) can be recurrently represented as

$$h^*(a, \psi, \varepsilon) = h^*_{(j)}(a, \psi, \varepsilon) + O(\varepsilon^j)$$
$$= h_1(a, \psi) + \varepsilon h_2(a, \psi) + \ldots + \varepsilon^{j-1}h_j(a, \psi) + O(\varepsilon^j),$$
$$h_j(a, \psi) = \int_{-\infty}^{\psi} \exp[-(\psi - \varphi)]H_j(a, \varphi)d\varphi, \tag{14}$$
$$H = Z(a, \psi, 0) + \varepsilon H_2 + \ldots + \varepsilon^{j-1}H_j + O(\varepsilon^j),$$

where the operator function H has form (12) and the coefficients h_j are trigonometric polynomials of ψ with the period 2π. The procedure specified by Eqs. (13) or (14) provides the desired solution $h^*(a, \psi, \varepsilon)$ with the required accuracy in ε.

The substitution of the expression $z = \varepsilon h^*$ into Eq. (9) for a, ψ on the local integral manifold leads to the following standard set with the rotating phase:

$$\dot{a} = \varepsilon A^*(a, \psi, \varepsilon), \quad A^* \equiv A(a, \psi, \varepsilon h^*(a, \psi, \varepsilon)),$$
$$\dot{\psi} = 1 + \varepsilon\Psi^*(a, \psi, \varepsilon), \tag{15}$$
$$\Psi^* = \Psi(a, \psi, \varepsilon h^*(a, \psi, \varepsilon)).$$

Set (15) is much simpler for analysis than set (9). The solution $a^*(\tau, \varepsilon)$, $\psi^*(\tau, \varepsilon)$ of set (15) for certain input data and a similar solution $a(\tau, \varepsilon)$, $\psi(\tau, \varepsilon)$, $z(\tau, \varepsilon)$ of set (9) have the properties [6]

$$|z(\tau, \varepsilon) - \varepsilon h^*(a^*(\tau, \varepsilon), \psi^*(\tau, \varepsilon), \varepsilon)| \le C\exp(-\kappa_*\tau),$$
$$|\xi(\tau, \varepsilon) - a^*(\tau, \varepsilon)\sin\psi^*(\tau, \varepsilon)| \le C\exp(-\kappa_*\tau), \tag{16}$$
$$C, \kappa_* > 0.$$

Therefore, self-excited oscillations of system (5) equivalent to Eqs. (9) are on the stable local manifold $z = \varepsilon h^*$ specified by Eqs. (11)–(14) and are described by Eqs. (15). These oscillations can be approximately constructed and analyzed by the Lyapunov–Poincaré methods [5, 7].

4. The evolution of the osculating variables a and ψ according to Eqs. (15) is analyzed by the averaging method [6–9]. The recurrence procedure separating a and ψ is very cumbersome and requires symbolic computer calculations. However, the first-approximation

solution is easily constructed and reduces to the integration of the system

$$\begin{aligned}\dot{a} &= \varepsilon A_1(a), \quad A_1 \equiv \langle A^*(a, \psi, 0)\rangle_\psi \\ &= \frac{a}{2}\left(\frac{1}{1+\kappa^2} - \sigma\right) - \frac{3}{8}\left(\frac{a^3}{1+\kappa^2}\right), \\ \dot{\psi} &= 1 + \varepsilon\Psi_1(a), \quad \Psi_1 \equiv \langle \Psi^*(a, \psi, 0)\rangle_\psi \\ &= -\frac{\kappa}{1+\kappa^2}\left(\frac{3}{8}a^2 - \frac{1}{2}\right),\end{aligned} \tag{17}$$

where the angular brackets mean the averaging over ψ. Equations (17) are integrated for given initial conditions, in particular,

$$\begin{aligned}a^{-2} - (a^0)^{-2}e^{-\varepsilon\gamma\tau} &= \frac{\chi}{\gamma}(1 - e^{-\varepsilon\gamma\tau}), \quad \gamma \neq 0; \\ a^{-2} - (a^0)^{-2} &= \varepsilon\chi\tau, \quad \gamma = 0; \\ \gamma &= (1+\kappa^2)^{-1} - \sigma, \quad \chi = \frac{3}{4}(1+\kappa^2)^{-1}.\end{aligned} \tag{18}$$

When dissipation is large, i.e., $\gamma \le 0$, the oscillation amplitude $a \to 0$ vanishes in the limit $\tau \to \infty$; i.e., self-excited oscillations do not arise. When dissipation is small, i.e., $\gamma > 0$, the amplitude $a(\varepsilon\tau, a^0)$ tends to the stable limiting value

$$a_* = \left(\frac{\gamma}{\chi}\right)^{1/2} = \sqrt{\frac{4}{3}}(1 - \sigma(1+\kappa^2))^{1/2}, \quad a_* \sim 1 \tag{19}$$

independently of $a^0 > 0$.

Value a_* (19) is the asymptotically (exponentially) stable stationary point of Eq. (17) for a. The point $a = 0$ is unstable. According to the Lyapunov–Poincaré method [5, 7], the desired periodic solution of systems (5), (9), and (15) exists, is unique for sufficiently small ε_0 values, and is an analytic function of ε, and the value a_* is the first approximation of the amplitude of self-excited oscillations with respect to ε.

In the first approximation, the frequency $\nu(a, \varepsilon)$ of nonstationary oscillations is determined by the equation for ψ in set (17), and the phase is represented in quadrature for the function $a(\varepsilon\tau)$ known according to Eqs. (18). For steady self-excited oscillations,

$$\nu(a_*, \varepsilon) = 1 + \frac{\varepsilon}{2}\sigma\kappa, \quad \psi = \left(1 + \frac{\varepsilon}{2}\sigma\kappa\right)\tau + \psi^0. \tag{20}$$

We represent the resulting expressions in the original dimensional variables according to Eqs. (3)–(5). The condition of existence $\gamma > 0$ and limiting cycle in the variables x, $\dot{x}$, and θ are described by the relations

$$\begin{aligned}2\delta &< \beta k_1 mcK(K^2 + m^2c^2\omega_0^2)^{-1}; \\ x &= da_*\sin\psi, \quad \dot{x} = d\omega_0 a_*\cos\psi, \\ \theta &= d\kappa k_1 a_*\left[\frac{1 - \frac{3}{4}a_*^2}{1+\kappa^2}(\kappa\sin\psi - \cos\psi)\right. \\ &\left. + \frac{a_*^2(\kappa\sin 3\psi - 3\cos 3\psi)}{4(9+\kappa)^3}\right],\end{aligned} \tag{21}$$

$$\begin{aligned}a_* &= \sqrt{\frac{4}{3}}\left(1 - \frac{2\delta}{\beta k_1 mcK}(K^2 + m^2c^2\omega_0^2)\right)^{1/2}, \\ d &= \left(\frac{k_1}{k_3}\right)^{1/2}, \quad \kappa = \frac{K}{mc\omega_0}.\end{aligned}$$

Using formulas (5), (17), and (20), we obtain the dimensional frequency ω and time ζ of reaching the limit cycle in the form

$$\begin{aligned}\omega &= \omega_0\left(1 + \frac{\delta K}{mc\omega_0^2}\right), \quad \zeta = \frac{1}{\varepsilon q\omega_0}, \quad \varepsilon\omega_0 = \frac{\beta k_1 K}{mc\omega_0^2}, \\ q &= \frac{m^2c^2\omega_0^2}{K^2 + m^2c^2\omega_0^2} - \frac{2\delta}{\varepsilon\omega_0}.\end{aligned} \tag{22}$$

Formulas (21) and (22) determine the characteristics of self-excited oscillations of the Helmholtz resonator specified by Eqs. (3) and (4) in the original thermal and gasdynamic variables. These formulas are considerably simplified if the dissipation coefficient δ can be ignored in calculations; i.e., if $\sigma \sim \varepsilon$. In this case, in the first approximation, $da_* = \left(\frac{4k_1}{3k_3}\right)^{1/2}$, the frequency ω is constant, and the constant ζ decreases.

Analysis of self-excited oscillations for moderate parameters ε defined in Eqs. (5) is of considerable interest. This analysis requires the development of numerical–analytical methods [10].

ACKNOWLEDGMENTS

This work was supported by the Russian Foundation for Basic Research, project nos. 02-01-00252 and 02-01-00157.

REFERENCES

1. J. W. Strutt (Lord Rayleigh), *The Theory of Sound* (Macmillan, London, 1896; Gostekhizdat, Moscow, 1955).
2. E. Skudrzyk, *The Foundations of Acoustics* (Springer, New York, 1971; Mir, Moscow, 1976).
3. K. F. Teodorchik, *Self-Oscillatory Systems* (Gostekhizdat, Moscow, 1952).
4. P. M. Morse, *Vibration and Sound* (McGraw-Hill, New York, 1936; GITTL, Moscow, 1949).
5. I. G. Malkin, *Some Problems of the Theory of Nonlinear Oscillations* (Gostekhizdat, Moscow, 1956).
6. Yu. A. Mitropol'skiĭ and O. B. Lykova, *Integral Manifolds in Nonlinear Mechanics* (Nauka, Moscow, 1973).
7. L. D. Akulenko, Izv. Ross. Akad. Nauk, Mekh. Tverd. Tela, No. 3, 26 (1995).
8. N. N. Bogolyubov and Yu. A. Mitropol'skiĭ, *Asymptotic Methods in the Theory of Nonlinear Oscillations* (Nauka, Moscow, 1974).
9. V. M. Volosov and B. I. Morgunov, *Averaging Methods in the Theory of Nonlinear Oscillations* (Mosk. Gos. Univ., Moscow, 1971).
10. L. D. Akulenko, L. I. Korovina, and S. V. Nesterov, Izv. Ross. Akad. Nauk, Mekh. Tverd. Tela, No. 3, 42 (2002).

Translated by R. Tyapaev

Doklady Physics, Vol. 48, No. 11, 2003, pp. 649–653. Translated from Doklady Akademii Nauk, Vol. 393, No. 1, 2003, pp. 47–51.

MECHANICS

Various Regimes of Motion of a Spherical Cavity at a Negative External Pressure

M. A. Guzev[1], K. V. Koshel'[2,*], and D. V. Stepanov[2,]**

Presented by Academician V.P. Myasnikov March 12, 2002

Received March 22, 2002

1. Study of the behavior of defects in the internal structure of a solid is of fundamental importance for simulation of its behavior under external action. The problem of the behavior of a spherical cavity is a classical problem for point defects. As early as in 1917, Rayleigh [1] showed that the absolute value of the velocity of the cavity boundary in an ideal incompressible fluid increases as $R^{-3/2}$ with a decease in the cavity radius R to zero. The compression of the cavity in a viscous medium with surface tension can lead to several collapse regimes [2–4]. The basic properties of cavity-collapse regimes under such conditions were studied by methods of the qualitative theory of differential equations in [5].

In this work, we analyze motion of a cavity at negative external pressure, i.e., when liquid is subjected to tension. It is shown that exact solutions of the dynamic equation for the cavity boundary in the viscous incompressible fluid exist for certain pressure values. These solutions correspond to the separatrix of the equation under consideration and make it possible to analyze the effect of pressure on the formation of the regimes of the collapse and growth of the cavity.

2. It is known [3] that the motion of the cavity boundary in the viscous incompressible fluid is described by the Rayleigh equation

$$\frac{3}{2}v^2 + Rv\frac{dv}{dR} + \frac{2\sigma}{\rho R} + \frac{4\mu v}{\rho R} = -\frac{P_\infty}{\rho}. \qquad (1)$$

Here, $v = \dfrac{dR}{dt}$ is the velocity of the boundary, σ is the surface tension, ρ is the medium density, μ is the dynamic viscosity, and P_∞ is the external pressure. We assume that the cavity is free of gas and $P_\infty < 0$; i.e., the applied pressure is tensile. In terms of the dimensionless variables u, r, and P introduced as

$$v = \frac{\sigma}{6\mu}u, \quad R = \frac{48\mu^2}{\rho\sigma}r, \quad -P_\infty = \frac{\rho\sigma^2}{24\mu^2}P, \qquad (2)$$

Eq. (1) is represented in the form

$$u^2 + \frac{2}{3}ru\frac{du}{dr} + \frac{1}{r} + \frac{u}{3r} = P. \qquad (3)$$

Equation (3) describes motion of the dissipative dynamic system, which generally has no integral of motion. However, Eq. (3) is integrable for certain P values. Direct calculation shows that

$$u \equiv U = 1 - \frac{1}{r} \text{ at } P = 1 \text{ and } u = -3 \text{ at } P = 9 \qquad (4)$$

satisfy Eq. (3) for $P = 1$ and 9, respectively. Although solutions are constructed only for two P values, they make it possible to separate trajectories corresponding to different types of motion of the cavity boundary.

3. For further analysis, we consider integral curves of Eq. (3) on the (u, r) phase plane. Solution (4) for $P = 1$ corresponds to separatrix *1* in Fig. 1a. It includes the point A, where $u = 0$ and $r_0 = 1$. The radius $r_0 = 1$ is determined only by the properties of the continuum and has the sense of the critical radius separating the regimes of collapse and extension of the cavity, e.g., in dimensional variables (2) $R_0 = 0.67 \times 10^{-6}$ m and $-P_\infty = 2.2$ atm for water.

For $P = 1$, the second separatrix *2* passes through the point A. The point A is a singular saddle point for Eq. (3). This point is absent for a positive external pressure. Separatrices *1* and *2* separate the phase plane into the regions with different regimes of motion of the cav-

[1] *Institute of Automation and Control Processes, Far East Division, Russian Academy of Sciences, ul. Radio 5, Vladivostok, 690041 Russia*
e-mail: guzev@iacp.dvo.ru, mikail@mail.primorye.ru
[2] *Pacific Oceanological Institute, Far East Division, Russian Academy of Sciences, ul. Baltiĭskaya 43, Vladivostok, 690041 Russia*
* *e-mail: kvkoshel@poi.dvo.ru*
** *e-mail: demon@freemail.vladivostok.ru*

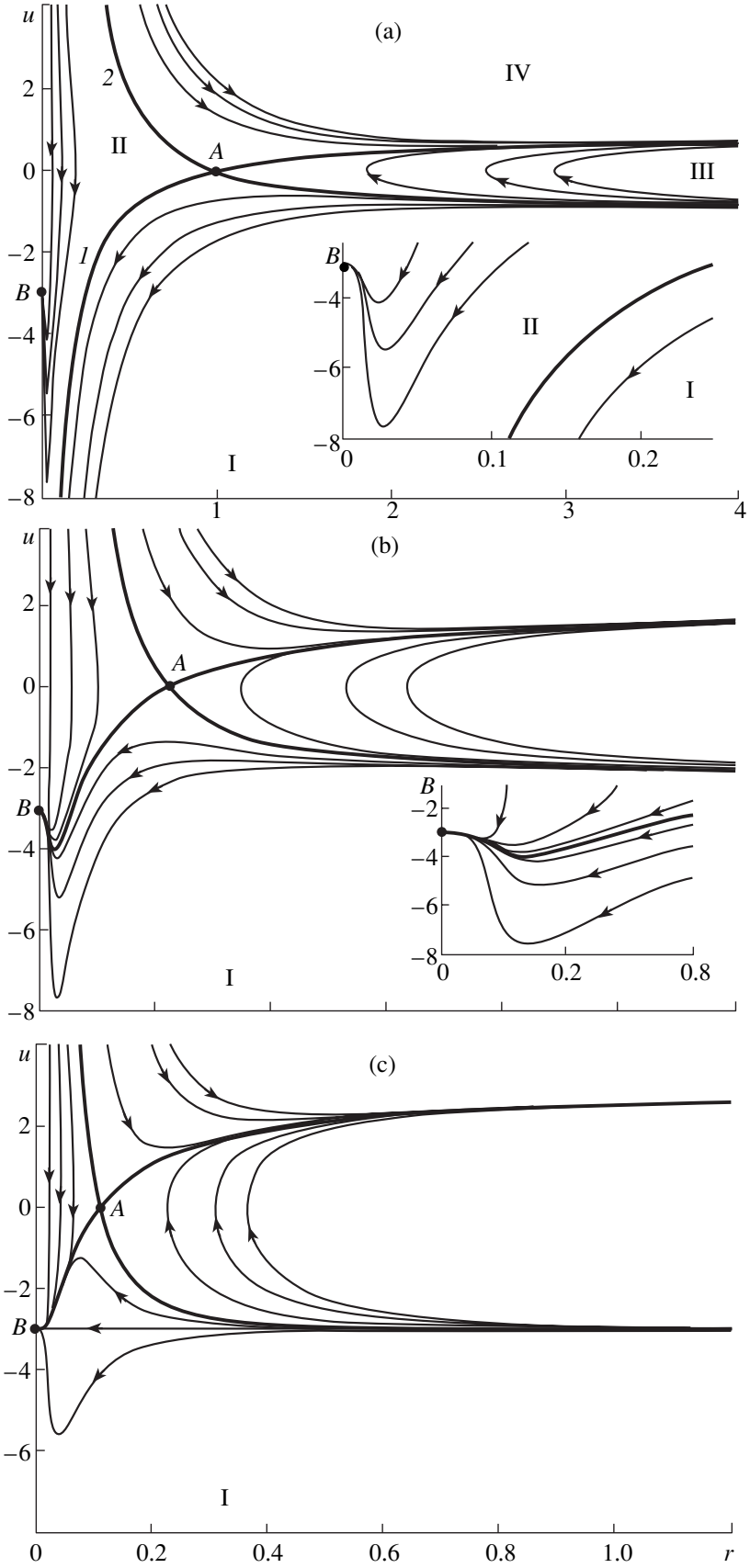

Fig. 1. Integral curves of Eq. (3) on the (u, r) phase plane for P = (a) 1, (b) 4.5, and (c) 9.

ity boundary. The direction of motion of the boundary is indicated by the arrow. Along integral curves located in region I, the absolute value of the velocity increases for $r \to 0$. All integral curves located in region II, i.e., between the axis $r = 0$ and separatrices, enter the point $B = (-3, 0)$ with the same slope. The point B has a saddle–node singularity and has one node sector in the physical region $r > 0$. This point is also absent for a positive pressure [5]. In region III, curves have a turning point, where the velocity $u = 0$. In region IV, the cavity boundary grows monotonically along integral curves.

We consider the case $P \neq 1$. The coordinates of the crossing point A of the separatrices can be found from Eq. (3) by setting $u = 0$. In this case, $r_0 = \frac{1}{P}$. The singularity type of this point coincides with the type for the case $P = 1$. Since the solution u on the separatrix has a zero at $r = r_0$, it should be represented in the form

$$u = \left(P - \frac{1}{r}\right) f, \tag{5}$$

where f is a certain function. We analyze the asymptotic behavior of separatrices *1* and *2* in the leading order in r for $r \gg r_0$. We consider the function f as a function of the variable $x = \frac{r_0}{r}$. Substituting expression (3) into Eq. (5), we arrive at the equation

$$f^2(3 - x) - 2x(1 - x) f \frac{df}{dx} + fx = \frac{3}{P} \tag{6}$$

for f. Substituting $f = \sum_{n=0}^{\infty} x^n f_n$ into this equation and equating terms with the same x powers, we obtain $f_0 = \pm\frac{1}{\sqrt{P}}$ in the leading (zeroth) order in $x \ll 1$. Therefore, according to Eq. (5), the solution u on separatrices *1* and *2* has the form $u \sim \pm\sqrt{P}$ in the leading order in x. Thus, separatrices *1* and *2* in the asymptotic region $r \gg r_0$ are symmetric with respect to the axis $u = 0$.

Numerical analysis shows that separatrix *1* has a minimum for $P > 1$ and is a monotonic function for $P \leq 1$. For $P \leq 1$ and $r \ll r_0$, Eq. (6) reduces to the equation

$$f^2(3t^2 - 1) + t(t^2 - 1) f \frac{df}{dt} + f = \frac{3t^2}{P}$$

for the function $f(t)$ in the new variable $t = \sqrt{\frac{1}{x}} = \sqrt{\frac{r}{r_0}}$. Substituting $f = \sum_{n=0}^{\infty} t^n f_n$ into this equation and equating terms with the same t powers, we obtain $f_0 = 1$ or 0 in the leading order in $t \ll 1$. Since the solution on the separatrix is singular for $r \ll r_0$, $u \sim P - \frac{1}{r}$.

We consider collapsing trajectories neighboring the separatrix and analyze the asymptotic behavior of the velocity of the cavity boundary for small r values. We take $P = 1$ because exact solution (4) is known for the velocity on the separatrix in this case. Substituting

$$u(r) = U(r) - \frac{g(r)}{r^{3/2}} = 1 - \frac{1}{r} - \frac{g(r)}{r^{3/2}} \tag{7}$$

into Eq. (3), we obtain the equation

$$\frac{2}{3} r^{1/2} \frac{\partial g}{\partial r}(r^{3/2} - r^{1/2} - g) + rg = 0$$

for the function $g = g(r)$. For certain $r = r_1$, the velocity $U(r_1) = u_1 < 0$, and $u(r_2) = u_1$ for neighboring trajectories with $r_2 = r_1 + \varepsilon$, where $0 < \varepsilon \ll 1$. Therefore, $g(r_2) = \frac{\varepsilon\sqrt{r_1 + \varepsilon}}{r_1}$ according to Eq. (7). Since we seek the asymptotic behavior of the function u for small r and ε, we take $r_1 = \varepsilon^{2\gamma}$, where $0 < 2\gamma < 1$. Then, replacing $g(r) \to g(r_2) \sim \frac{\varepsilon}{\sqrt{r_1}} = \varepsilon^{1-\gamma}$ in Eq. (7) in the leading order in $\varepsilon^{1-\gamma}$, we obtain

$$u(r) \sim 1 - \frac{1}{r} - \frac{\varepsilon^{1-\gamma}}{r^{3/2}}. \tag{8}$$

Therefore, the Rayleigh law of cavity collapse, i.e., $|u| \sim r^{-3/2}$, is observed when $\sqrt{r} \ll \varepsilon^{1-\gamma}$. At the same time, the contribution on the separatrix dominates in Eq. (8) when $\varepsilon^{1-\gamma} \ll \sqrt{r} \ll \sqrt{\varepsilon}$. Indeed, relation (8) can be represented in the form

$$u(r) \sim 1 - \frac{1}{\varepsilon^{2(1-\gamma)}}\left(\frac{1}{z} + \frac{1}{z^{3/2}}\right), \tag{9}$$

where $z = r\varepsilon^{2(1-\gamma)}$. The contribution on the separatrix dominates when $\sqrt{z} \gg 1$, i.e., $\sqrt{r} \gg \varepsilon^{1-\gamma}$. The latter condition is consistent with the condition $\sqrt{r} \ll \sqrt{\varepsilon}$, because $\gamma < \frac{1}{2}$. When $z \sim 1$, i.e., $\sqrt{r} \sim \varepsilon^{1-\gamma}$, the terms in

the parentheses in relation (9) are of the same order of smallness.

The appearance of a minimum on separatrix *1* for $P > 1$ changes the behavior of integral curves located in region I for $r \to 0$. These curves, as well as the separatrix, enter the point B with the same slope $3(P - 9)$. The curves in region II have the same slope. The singularity type of the point B is similar to the case $P = 1$, but there are two node sectors for $P > 1$. Figure 1b shows integral curves for $P = 4.5$. The distance between any two curves entering the point B is exponentially small for $r \to 0$. Indeed, any two solutions u_2 and u_1 of Eq. (3) satisfy the relation

$$u_-(u_1 + u_2) + \frac{2}{3}r\left(u_1\frac{\partial u_-}{\partial r} + u_-\frac{\partial u_2}{\partial r}\right) + \frac{u_-}{3r} = 0,$$

where the function $u_- = u_2 - u_1$ determines the difference between the trajectories. Since $u_1, u_2 \to -3$ and $r\frac{\partial u_2}{dr} \to 0$ for $r \to 0$, u_- satisfies the equation $u_-\left(-6 + \frac{1}{3r}\right) = 2r\frac{\partial u_-}{\partial r}$ whose general solution has the form

$$u_- = \frac{u_0}{r^3}\exp\left(-\frac{1}{6r}\right).$$

For $r \to \infty$, trajectories that lie in regions III and IV and correspond to the growth of the cavity asymptotically approach separatrix *1*, i.e., $u \to \sqrt{P}$. It can be shown (similarly to the consideration for the point B) that the distance between any two trajectories decreases as $\frac{1}{r^3}$.

Let us analyze the asymptotic behavior of separatrix *2* and trajectories in region II for $r \to 0$ and $u > 0$. Since the solutions of Eq. (3) that correspond to the separatrix and trajectories vanish for certain $r = a$, u can be represented as $u = \left(P - \frac{a}{r}\right)f$. The parameter a specifies trajectories, in particular, $a = 1$ for the separatrix. Taking

$$f = \frac{1}{\sqrt{x}}\varphi(x), \quad x = \frac{Pr}{a},$$

we arrive at the equation

$$2\varphi^2 x(x-1) + 2x(x-1)^2\frac{d\varphi}{dx}\varphi + \frac{1}{a}(x-1)\sqrt{x}\varphi = -\frac{3}{Pa}x^2 + \frac{3}{Pa}x^3$$

for φ. The formal asymptotic expansion of the function φ for $x \to 0$ must be written in terms of $\sqrt{x}$ powers beginning with zeroth power, i.e.,

$$\varphi = \varphi_0 + \sum_{n=1}^{\infty} x^{n/2}\varphi_n.$$

The leading asymptotic term φ_0 is determined by the parameters of a trajectory in region II, and the other expansion terms φ_n are calculated in terms of φ_0. Therefore, trajectories in region II for $u > 0$ have the velocity asymptotic behavior $u \sim r^{-3/2}$ for $r \to 0$.

For $P = 9$, the minimum of the separatrix coincides with the point B (Fig. 1c), and corresponding solution (4) appears. To reveal the physical meaning of this solution, we consider trajectories in region I that have extrema where $\frac{\partial u}{\partial r} = 0$. From Eq. (3), the second derivative of the velocity at the extremum r_* is calculated as

$$\frac{d^2u}{dr^2} = \frac{u_* + 3}{2u_*r_*^3},$$

where $u_* = u(r_*)$. Therefore, r_* is the point of maximum and minimum if $u_* > -3$ and $u_* < -3$, respectively. For solution (4), the second derivative of the velocity is equal to zero. Thus, the solution $u = -3$ is the line of inflection for trajectories in region I.

The qualitative behavior of trajectories in regions III and IV does not change with P.

4. The above analysis of motion of the cavity boundary at a negative external pressure shows that both regimes of growth and collapse can be realized by choosing initial data. The phase plane is separated by two separatrices into four regions of different types of motion. The behavior of the separatrix corresponding to the collapse regime depends on the external pressure P. For $P = 1$, exact solution (4) whose singular behavior in the limit $r \to 0$ does not change for $P < 1$ is constructed for this trajectory. The asymptotic behavior of a collapsing trajectory neighboring the separatrix for small r values and $P = 1$ depends on the relation between r and the parameter characterizing the initial distance between this trajectory and the separatrix. For $P > 1$, collapsing trajectories, as well as the separatrix, have a finite velocity at the instant of closure, and the distance

between any trajectories is exponentially small in r. Trajectories corresponding to the growth regime have asymptotic behavior $\sim\sqrt{P}$.

ACKNOWLEDGMENTS

This work was supported by the Russian Foundation for Basic Research (project no. 01-01-96904) and in part by the Council of the President of the Russian Federation for Support of Leading Scientific Schools (project no. 00-15-98608).

REFERENCES

1. J. W. Strutt (Lord Rayleigh), Philos. Mag., Ser. 6 **34**, 94 (1917).
2. E. I. Zababakhin, Prikl. Mat. Mekh. **24**, 1129 (1960).
3. A. D. Pernik, *Problems of Cavitation* (Sudostroenie, Leningrad, 1966).
4. Yu. L. Levkovskiĭ and V. P. Il'in, Inzh.-Fiz. Zh. **14**, 903 (1968).
5. A. V. Kononov, Prikl. Mat. Mekh. **53**, 346 (1989).

Translated by R. Tyapaev

Doklady Physics, Vol. 48, No. 11, 2003, pp. 654–656. Translated from Doklady Akademii Nauk, Vol. 393, No. 3, 2003, pp. 341–344.

MECHANICS

On the Inversion of the Lyapunov Theorem on Asymptotic Stability in the First Approximation

O. V. Druzhinina

Presented by Academician V.V. Rumyantsev June 19, 2003

Received July 4, 2003

The notions of both asymptotic stability and exponential stability for a solution to an ordinary multidimensional differential equation were introduced by Lyapunov [1] (see also [2–4]). The question on the most natural generality of these notions was treated in [5, 6].

In this paper, we prove the reversibility of the Lyapunov theorem about asymptotic stability (of exponential type) of the solution $x = 0$ of the nonlinear differential equation

$$\frac{dx}{dt} = Ax + g(t, x), \quad x \in R^n, \tag{1}$$

provided that the constant $n \times n$ matrix A of the linear approximation

$$\frac{dx}{dr} = Ax, \quad x \in R^n \tag{2}$$

is stable, and the vector function $g(t, x)$ continuous on the set $R^+ \times \{|x| < h\}$ satisfies the condition

$$\exists h > 0, \quad \frac{|g(t, x)|}{|x|} \to 0 \ \text{ as } \ x \to 0, \quad |x| < h,$$

uniformly with respect to $t \in R^+$, where $|\cdot|$ is an arbitrary norm of the vector function.

We recall that a matrix is referred to as stable (semistable) matrix if all its eigenvalues have negative (nonpositive) real parts.

Definition 1 [1]. The solution $x = 0$ of Eq. (1) is referred to as an exponentially asymptotically stable (or exponentially stable) solution if there exist (as $t \to +\infty$) numbers $c > 0$, $r_0 > 0$, and $\omega > 0$ such that each solution $x(t)$ of Eq. (1) under the initial condition $|x(0)| \le r_0$ meets the inequality

$$|x(t)| \le c|x(0)|\exp(-\omega t). \tag{3}$$

Russian Open State Technical University of Railway Transport, ul. Chasovaya 22/2, Moscow, 125993 Russia

The exponential asymptotic stability of the solution $x = 0$ of Eq. (1) with a stable matrix A was proved by Lyapunov [1] for the case of an analytical right-hand side and by Cotton [7], Perron [8], and Petrowsky [9] for the case of nonanalytical right-hand sides.

We now represent the Lyapunov theorem on the asymptotic stability in the first approximation.

Theorem 1 [8]. *Let* (1) *A be a constant stable $n \times n$ matrix and* (2) *a continuous function $g(t, x)$* of *(t, x) satisfy the condition*

$$g(t, x) = o(|x|) \ \text{ as } \ x \to 0, \quad |x| < h, \tag{4}$$

uniformly with respect to $t \in R^+$, where $o(|x|)$ is a function infinitesimal as $x \to 0$.

In this case, the solution $x = 0$ of Eq. (1) *is exponentially stable as $t \to +\infty$ in the sense of Definition* 1.

The proof of Theorem 1 can be found, e.g., in [10, 11].

Remark 1. Hypothesis (3) in Theorem 1 can be substituted by one of the following conditions [10, 11]. (1) The inequality

$$\forall k > 0 \quad |g(t, x)| < k|x| \quad \forall t > t_0 \tag{5}_1$$

is satisfied for all sufficiently small $|x(t)|$; and for any arbitrary number $\varepsilon > 0$ there exist numbers $\delta > 0$ and $\tau > 0$ such that

$$|g(t, x)| \le \varepsilon|x| \quad \forall t \ge \tau \quad \forall |x| \le \delta. \tag{5}_2$$

(2) The inequality

$$\forall k > 0 \quad |g(t, x)| < k|x| + |x|^{1+a}t^a \quad \forall t > t_0 \tag{6}_1$$

is satisfied for certain numbers $a > 0$ and $b > 0$ and for all $|x|$ sufficiently small in norm, and for every number $\varepsilon > 0$, there exist numbers $\delta > 0$ and $\tau > 0$ such that

$$|g(t, x)| \le \varepsilon|x| + |x|^{1+a}t^b \quad \forall t \ge \tau \tag{6}_2$$

for all $|x| < \delta$.

Remark 2. Theorem 1 remains valid if the matrix A in Eq. (1) is substituted by a periodic matrix $A(t)$. In this case, eigenvalues of A are substituted by characteristic indices of the linear equation $\dot{y} = A(t)y$. Indeed, Eq. (1)

1028-3358/03/4811-0654$24.00

can be transformed into an equation with a constant matrix by the change of variables $x = By$, where B is a periodic matrix with the determinant satisfying the inequalities $|\det B| < c$ and $|\det B^{-1}| < c$ [11].

Theorem 1 cannot be generalized for the case when the constant matrix A and its eigenvalues are substituted by a continuous matrix $A(t)$ bounded on R^+, and its characteristic indices, respectively. We now consider an example.

Example [8]. The linear approximation to the nonlinear equations

$$\dot{x}_1 = -ax_1, \quad \dot{x}_2 = (\sin\ln t + \cos\ln t - 2a)\dot{x}_2 + x_1^2 \quad (7)$$

has the form

$$x_1 = -ax_1, \quad \dot{x}_2 = (\sin\ln t + \cos\ln t - 2a)\dot{x}_2. \quad (8)$$

The characteristic indices $-a$ and $1 - 2a$ of Eqs. (8) are negative for $a > \frac{1}{2}$. Hence, for $a > \frac{1}{2}$, the zero solution $x_1 = x_2 = 0$ to Eqs. (8) are exponentially stable as $t \to +\infty$. However, for $a \in \left(\frac{1}{2}, \frac{1}{2} + \frac{1}{4}e^{-\pi}\right)$, the zero solution $x_1 = x_2 = 0$ of nonlinear equations (7) is unstable as $t \to +\infty$ in the Lyapunov sense.

The following theorem is valid.

Theorem 2. *Let* (1) *a $n \times n$ matrix C be nonsingular and a continuous vector function $f(t, y)$ of (t, y) satisfy the condition*

$$f(t, y) = o(|y|) \ \text{ as } \ y \to 0 \ \text{ uniformly with respect to } t \in R^+, \quad (9)$$

and let (2) *the solution $y = 0$ of the nonlinear differential equation*

$$\frac{dy}{dt} = Cy + f(t, y) \quad (10)$$

be exponentially stable as $t \to +\infty$ in the Lyapunov sense. In this case, the matrix C is semistable.

Proof by contradiction. We assume that one of eigenvalues of the matrix C has a positive real part. Since the perturbation $f(t, y)$ satisfies condition (9), then, according to the Lyapunov theorem on the instability in the first linear approximation, the solution $y = 0$ of Eq. (10) is unstable as $t \to +\infty$ in the Lyapunov sense. Thus, we arrive at the contradiction, and Theorem 2 is proved.

We now prove the following theorem, which is inverse to Theorem 1, on exponential stability as $t \to +\infty$ in the linear approximation.

Theorem 3. *Let* (1) *a $n \times n$ matrix A be nonsingular and a continuous vector function $g(t, x)$ of (t, x) satisfy condition* (3), *and let* (2) *the solution $x = 0$ to nonlinear differential equation* (1) *be exponentially stable as $t \to +\infty$. In this case, the solution $x = 0$ to linear differential equation* (2) *is exponentially stable as $t \to +\infty$.*

Proof. Let the assumptions of Theorem 3 be fulfilled. To prove Theorem 3, we must argue that the matrix A is stable and, hence, the solution $x = 0$ of Eq. (2) is exponentially stable as $t \to +\infty$. Since the solution $x = 0$ to nonlinear equation (1) is exponentially stable as $t \to +\infty$, there exists a number $\omega > 0$ and, for each $\varepsilon > 0$, there is a number $r_0 = r_0(\varepsilon)$ such that the solution $x(t)$ of Eq. (1) under the initial conditions $|x(t_0)| < r_0$ satisfies the inequality

$$|x(t)| < \exp\{-\omega(t - t_0)\} \quad \forall t \geq 0. \quad (11)$$

Performing the change of variables $x = y\exp(-\omega t)$, we reduce Eq. (1) to the form

$$\frac{dy}{dt} = (A - \omega E)y + |y|\mu(t, y)\exp(-\omega, t), \quad (12)$$

where E is the unit matrix, and the function $\mu(t, x) :: = |y|^{-1} g(t, y)$, continuous in (t, y), satisfies the condition

$$\mu(t, y) \to 0, \text{ as } y \to 0 \ \text{ uniformly with respect to } t \in R^+. \quad (13)$$

We now verify that the solution $y = 0$ to Eq. (12) is stable as $t \to +\infty$ in the Lyapunov sense. Indeed, let $\varepsilon > 0$ be a given number. By virtue of the assumption (2) of Theorem 3, for an arbitrary $t_0 \geq 0$, there exists a number $r_0 = r_0(t_0, \varepsilon)$ such that an arbitrary solution $x(t)$ of Eq. (1) under the initial condition $|x(t_0)| < r_0$ satisfies the inequality

$$|x(t)| \leq \varepsilon\exp(-\omega t_0)\exp\{-\omega(t - t_0)\} \quad \forall t \geq 0. \quad (14)$$

Hence,

$$|x(t)| < \varepsilon\exp(-\omega t) \quad \forall t > t_0. \quad (15)$$

Let $y(t)$ be a solution to Eq. (12) under the initial condition satisfying the inequality $|y(t_0)| < r_0$. In this case,

$$|x(t)|\exp(\omega t_0) < r_0 \quad (16)$$

and

$$|x(t_0)| < r_0. \quad (17)$$

It follows from (16) and (17) that

$$|x(t)| < \varepsilon\exp(-\omega t) \quad \forall t > t_0. \quad (18)$$

Hence,

$$|y(t)|\exp(-\omega t) < \varepsilon\exp(-\omega t) \quad \forall t > t_0, \text{ or } |y(t)| < \varepsilon \quad \forall t > t_0. \quad (19)$$

Relationship (19) implies that the solution $y = 0$ to Eq. (12) is stable as $t \to +\infty$ in the Lyapunov sense.

We set

$$C_1 = A - \omega E, \quad f(t, y) = |y|\mu(t, y)\exp(-\omega t). \quad (20)$$

In this case, Eq. (12) takes the form

$$\frac{dy}{dt} = C_1 y + f(t, y), \quad (21)$$

where the continuous function $f(t, y)$ of (t, y) satisfies condition (3). Since the solution $y = 0$ of Eq. (20) is stable in the Lyapunov sense as $t \to +\infty$, according to Theorem 2, the matrix C_1 is semistable and, hence, the real parts of eigenvalues of the matrix A are smaller than or equal to $-\omega$, i.e., they are negative. Therefore, linear equation (2) is exponentially stable as $t \to +\infty$. Thus, Theorem 3 is proved.

It is important to note that the reversibility of Theorem 1 on the exponential stability in the first approximation is applicable only to Eq. (1) with a constant matrix A. Let us consider the vector equation

$$\frac{dx}{dt} = F(x), \quad F(0) = 0, \tag{22}$$

defined in the neighborhood of a point $x_0 \in R^n$, where $F(x)$ is a smooth function (of the C^1 type) on the differentiable manifold V_n.

The exponential stability of the solution $x = 0$ of the first approximation

$$\frac{dx}{dt} = F'(x(t))x \tag{23}$$

along the solution $x(t)$ of Eq. (22) does not ensure the stability as $t \to +\infty$ for this solution in the Lyapunov sense.

It was proved in [12, 13] that the exponential asymptotic stability of the solution $x = 0$ to Eq. (22) does not remain valid, and all exponentially stable solutions form a dense set.

We refer to the property P of solutions to nonlinear equation (22) as: (1) a typical property in the C^1 topology if all mappings $F \in C^1(R^n, R^n)$ having this property form a dense set in the space $C^1(R^n, R^n)$; (2) a C^1-preserving property if there exists a neighborhood U of an element F in the C^1 topology, such that for all elements $G \in U$ the equilibrium state $x = 0$ for the equation $\dot{x} = G(x)$ has this property; and (3) a C^1-nonpreserving property if it is not the C^1-preserving property.

The exponential stability under consideration is a typical property in the C^1 topology. Namely, the following propositions are consequences of the results of [12, 13].

Proposition 1. *Let all nonlinear differential equations* (22) *form a set $\mathcal{F}$ having the C^1 topology, and let a $\mathcal{F}_1$ ($\mathcal{F}_2$) be a subset of the set $\mathcal{F}$ formed by Eqs.* (22) *for which the equilibrium state $x = 0$ is asymptotically* (*exponentially*) *stable. In this case, the subset $\mathcal{F}_2$ is typical in the subset $\mathcal{F}_1$, i.e., $[\mathcal{F}_2] = \mathcal{F}_1$, where $[\mathcal{F}_2]$ is the closure of the subset $\mathcal{F}_2$ in the C^1 topology.*

Proposition 2. *The asymptotic stability of the equilibrium state $x = 0$ of Eq.* (22) *is a C^1-nonpreserving property if $F \in \mathcal{F}_1 \backslash \mathcal{F}_2$.*

Proposition 2 is a complement to the results of [4, 14] concerning the robustness of the asymptotic stability of the hyperbolic equilibrium state of Eq. (22) in the case of the C^0 topology of its right-hand side.

ACKNOWLEDGMENTS

I am grateful to Prof. A.A. Shestakov and Academician V.V. Rumyantsev for their attention to this study.

REFERENCES

1. A. M. Lyapunov, *The General Problem of the Stability of Motion* (Kharkovsk. Mat. Obshchestvo, Kharkov, 1892; Taylor & Francis, London, 1992).
2. N. G. Chetaev, *Stability of Motion* (GITTL, Moscow, 1955).
3. V. V. Vorotnikov and V. V. Rumyantsev, *Stability and Control of Coordinates Concerning Part of the Phase Vector in Dynamic Systems: Theory, Methods, and Applications* (Nauchn. Mir, Moscow, 2001).
4. N. N. Krasovskiĭ, *Stability of Motions* (Gos. Izd. Fiz.-Mat. Lit., Moscow, 1959; Stanford University Press, 1963).
5. V. M. Millionshchikov, in *Dynamical Systems and Boundary-Value Problems* (Shtiintsa, Kishinev, 1987), pp. 84–99.
6. V. M. Millionshchikov, Mat. Zametki **36**, 517 (1983).
7. E. Cotton, Annales de l'Ecole Normale Superieure, Ser. 3 **28**, 473 (1911).
8. O. Perron, Math. Z. **29**, 129 (1928).
9. I. Petrowsky, Mat. Sb. **41**, 108 (1934).
10. E. A. Coddington and N. Levinson, *Theory of Ordinary Differential Equations* (McGraw-Hill, New York, 1955; IL, Moscow, 1958).
11. L. Cesari, *Asymptotic Behavior and Stability Problems in Ordinary Differential Equations* (Springer, Berlin, 1959; Mir, Moscow, 1964).
12. O. V. Druzhinina, Dokl. Akad. Nauk **343**, 332 (1995) [Dokl. Phys. **40**, 362 (1995)].
13. O. V. Druzhinina, Dokl. Akad. Nauk **343**, 473 (1995).
14. E. A. Barbashin, *Section Method in Theory of Dynamic Systems* (Nauka i Tekhnika, Minsk, 1979).

Translated by V. Chechin